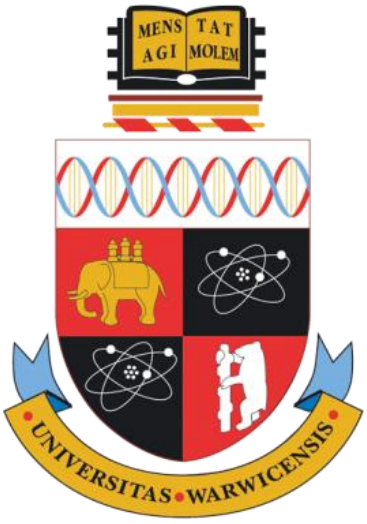

Assessment of Solidification Behaviour of Peritectic Steels

Kateryna Hechu

A thesis submitted in fulfilment of the requirements for the degree of Doctor of Philosophy in Engineering

University of Warwick
Warwick Manufacturing Group

February 2018

Abstract

Casting of peritectic steels is often associated with defects such as cracking that may lead to breakouts. Such defects have technical and financial disadvantages. There are many arguments about the reason for the defect formation in peritectic steels. The principal purpose of the present research is to gain a further understanding for the cause of the defect formation during solidification of peritectic steels, which may help to improve the castability of peritectic steels. The main finding of this thesis is that the solidification behaviour of peritectic steels differs significantly in comparison to non-peritectic steels and pure iron.

Peritectic steels have been historically hard to characterise via Differential Scanning Calorimetry (DSC) due to the multiple phase transformations (DSC only gives information on if a transformation is occurring, not which phase). One of the findings of this research is that it explains what was previously reported to be an undercooled peritectic reaction of the DSC cooling plot is, in fact, the bulk transformation of the solute poor dendrite cores from delta-ferrite (δ) to austenite (γ). This observation allowed to quantify the latent heat associated with the solidification and showed that peritectic steel release 38% more heat compared to the non-peritectic. The DSC results also showed that the amount of undercooling of δ to γ transformation in peritectic steels is measured to be greater (75°C) compared to non-peritectic steels (32-35°C).

A significant difference was seen on shrinkage behaviour of steels with different cooling rates. However, little difference in shrinkage was found between peritectic and non-peritectic steels.

Confocal Scanning Laser Microscopy (CSLM) has shown the presence of remelting of peritectic steels at all cooling rates tested, although no remelting was observed in non-peritectic steels.

The technique of combining CSLM and infrared thermography that was used for the first time in this research allowed observing the non-uniform and poor heat extraction during solidification of peritectic steels.

Table of Contents

List of Figures

List of Tables

Nomenclature

Notation	Description	Unit
$V\gamma$	velocity of the γ growth	µm/s
D_L	diffusion coefficient of carbon in the liquid	m^2/s
R	radius of the growing γ	µm
C_L^{γ}	carbon concentrations in the liquid in equilibrium with the γ	wt.%
C_L^{δ}	carbon concentrations in the liquid in equilibrium with the δ	wt.%
C_{γ}^{L}	carbon concentrations in the γ in equilibrium with the liquid	wt.%
J_C	diffusion flux of C atoms	µm/s
J_{Ni}	diffusion flux of Ni atoms	µm/s
T_o	temperature at which the free energy of the δ and γ phases (in the case of Fe-C alloys) is equal	°C
Q	radiated heat	W
A	surface area	mm^2
ε	emissivity	-
σ	Stefan-Boltzmann constant	$Wm^{-2}K^{-4}$

List of Acronyms

Acronym	Description
CC	Continuous Casting
DSC	Differential Scanning Calorimetry
CSLM	Confocal Scanning Laser Microscope
AHSS	Advanced High Strength Steel
HSLA	High Strength Low Alloy
BCC	Body-centred Cubic
FCC	Face-centred Cubic
IR	Infrared

Acknowledgements

I would like to express my deepest gratitude to the special people who motivated me for the success of this work.

I am grateful to Professor Sridhar Seetharaman for giving me the opportunity to do this interesting research, and for his patience, valuable guidance, knowledge and encouragement extended to me.

I am also grateful to Dr Carl Slater for his endless research ideas, patience and encouragement, which greatly assisted this research.

My sincere thanks to Dr Begona Santillana for her guidance, continuous support and motivation which helped me a lot.

Thanks also to Dr Prakash Srirangam for his comments and suggestions on the early stages of my research.

I would like to acknowledge Tata Steel and University of Warwick for proposing and funding the project.

A huge thanks to all my colleagues, friends and everyone who, directly or indirectly, helped me in this venture.

Special thanks to my Parents for their love and words of encouragement in whatever I pursue.

Finally and most importantly, Sina, I could not have done this without your support.

Declaration

The research presented within this thesis has been undertaken by me, except where otherwise stated. No part of this thesis has been submitted in support of another degree. The thesis is presented in accordance with the regulations of Warwick University.

Kateryna Hechu

February 2018

Peer-reviewed Publications

1. K. Hechu, C. Slater, B. Santillana, P. Srirangam, S. Sridhar, Real-time Measurement of Contraction Behaviour of Peritectic Steels during Solidification, in: AISTech - Iron Steel Technol. Conf. Proc., 2016.
2. K. Hechu, C. Slater, B. Santillana, S. Clark, S. Sridhar, A novel approach for interpreting the solidification behaviour of peritectic steels by combining CSLM and DSC, Mater. Charact. J. 133 (2017) 25–32.
3. C. Slater, K. Hechu, S. Sridhar, Characterisation of solidification using combined Confocal Scanning Laser Microscopy with Infrared Thermography, Mater. Charact. 126 (2017) 144–148.

Chapter 1 Motivation: Significance of Casting Peritectic Steel Grades

Casting is one of the most important steps in the steel making process. The events, which occur at the liquid-solid interface during the Continuous Casting (CC) process, such as solidification, phase transformations, shrinkage and exothermic reactions, have a significant influence on the product quality [1]. More than 1.6 billion tonnes of steel were produced in 2016 [2]; therefore, it is essential to gain a better understanding of these events.

The 'near final' shape of the steel product is partially determined by the geometry of the mould, and many physical properties of castings can be established through optimal control during the solidification of steel [3]. Steel is predominantly cast into semi-finished products such as blooms, billets, slabs using the CC process [4]. In addition, direct strip and wire casting are carried out for certain grades of steel which allows significant energy and cost savings [5–7].

The World Steel Association estimates that there are over 3,500 different grades of steel, encompassing unique physical, chemical, and environmental properties [8]. The steels with a carbon equivalent of between 0.07% - 0.18% are referred to as peritectic steels [9]. Steels produced close to or within the peritectic composition range, such as AHSS (Advanced High Strength Steel) and HSLA (High Strength Low Alloy), have the mechanical properties required for the automotive applications combined with low production costs [10]. Therefore, there is a need to produce these grades in high volume.

However, the solidification paths associated with peritectic transformation during continuous casting often become a reason for defects such as deeper oscillation marks, longitudinal cracks and even breakouts [11–15]. The especially severe longitudinal cracks which lead to a breakout of peritectic steel grades are illustrated in Figure 1.1. Previous analyses have shown that such defects originate in the mould [16], but uncertainties still remain about the main reason behind the defect formation in peritectic steels. In order to minimise the defects, casting of peritectic grades is typically performed at lower speeds, leading to up to 20% lower plant productivity [13]. Therefore, it is crucial to obtain an

enhanced understanding of the reason behind the defect formation in peritectic steels to minimise or prevent the defects in the future.

Figure 1.1 Severe longitudinal facial crack and breakout shell of solidified peritectic steel grade (Fe-0.1wt% C) [16]

During the peritectic reaction, the liquid (L) reacts with a primary solid phase (delta-ferrite or δ) to form a secondary solid phase (austenite or γ) [7]. The two solid phases, δ and γ, have different crystal structures - body-centred cubic (BCC) and face-centered cubic (FCC), respectively [17]. Therefore, the peritectic reaction is associated with the volume contraction (shrinkage) because the density of γ is larger than δ [18]. This shrinkage leads to the formation of an air gap between the steel shell and the mould during the CC process, which reduces the contact with the water-cooled mould during the CC process and decreases the heat flux in the CC machine. It subsequently leads to a thinner solidified shell and increased strains and stresses within the liquid-solid region [19], which results in defect formation such as internal and external cracks, breakouts, uneven shell growth and surface reliefs [20].

It is well established that the surface defects of continuously cast product originate in the meniscus region (liquid-solid interface) during the early solidification stages when the solidified shell is thin [20]. To fully understand the reason behind the defect formation in peritectic steels, it is essential to understand the influence of processing parameters, such as temperature, composition, phase transformation, latent heat, and shrinkage on solidification behaviour of peritectic steels. The study of peritectic transformations through conventional

techniques is challenging due to the decomposition of the high-temperature phases. Therefore, there is a need to develop new methods that allow for the in-situ study of such transformations for them to be fully understood.

1.1 Research Aims and Objectives

A fundamental aim of the current research is to obtain a detailed explanation of the reason for the defect formation during solidification of peritectic steels, which may help to improve the operational stability of casting peritectic steels. The present research was designed based on the previous review of the literature with the following objectives:

1. To identify the solidification paths of a series of selected industrial peritectic and non-peritectic steel grades based on the thermodynamic Thermo-Calc calculations.
2. To determine the reason for different thermal responses between heating and cooling in peritectic steels during the Differential Scanning Calorimetry (DSC) experiments and to analyse the difference in solidification behaviour between industrial steel samples based on the DSC measurements and Confocal Scanning Laser Microscope (CSLM) results.
3. To determine and compare the solidification shrinkage of peritectic and non-peritectic steels in real-time conditions under different cooling rates, comparable with the CC process.
4. To analyse the solidification behaviour of steels during shrinkage experiments based on the thermal profile of the sample surface obtained using infrared (IR) thermography.
5. To develop a new experimental technique which gives the understanding of the defect formation of peritectic steels during solidification.

1.2 Research Hypotheses

The comprehensive literature review on the topic of peritectic solidification in Fe-C alloys revealed that it leads to defect formation during solidification. However, the exact reason for the origin of those defects is still missing. In the attempt to understand the initial solidification behaviour of peritectic steels, it is hypothesised that:

1) Thermodynamic calculations predict higher shrinkage and an exothermic reaction during solidification of peritectic steel, compared to non-peritectic steels.

2) A peritectic reaction occurs during the first peak on the DSC cooling curve rather than during the second peak.

3) The peritectic steels exhibit a greater measured solidification shrinkage than non-peritectic ones.

4) Due to massive $\delta \rightarrow \gamma$ transformation during fast cooling rates, the peritectic steel will show a higher shrinkage rate during solidification compared to the non-peritectic steels.

5) Large shrinkage and high exothermic heat during the peritectic reaction is a cause of the defect formation during solidification.

1.3 Outline of the thesis

The remainder of this thesis is organised as follows:

Chapter 2 reviews the literature relevant to the scope of the research and identifies the gap in the knowledge;

Chapter 3 outlines the methodology of the research including the experimental techniques employed to investigate the research questions;

Chapter 4 explains the analysis of the solidification behaviour of peritectic steels using the combination of CSLM and DSC techniques;

Chapter 5 presents the solidification shrinkage measurement results using in techniques;

Chapter 6 shows the results of the solidification behaviour of peritectic steels using the combination of CSLM and IR thermography and explains the reason for the defect formation during solidification of the Steels;

Chapter 7 highlights the key conclusions of the research and includes the recommendations for further research.

Chapter 2 Literature Review of Phase Transformations in Peritectic Steels

2.1 Introduction

The peritectic phase transformation, where liquid reacts with primary solid phase (δ) to form secondary solid phase (γ), is a phase transformation that is very interesting and challenging at the same time to study. It can only be observed at around 1500°C as steel solidifies because the microstructure of the δ cannot be seen at room temperature, as it transforms twice during cooling: $\delta \rightarrow \gamma$ and then $\gamma \rightarrow \alpha$. Modelling gives an excellent insight into the peritectic reaction and transformation, but mainly based on the equilibrium conditions. There are still many controversial reports found in the literature, where contradicting assumptions are made on the solidification of the peritectic steel, depending on the experimental technique or mathematical results[21–23]. The only common agreement reported in all literature regarding peritectic steels is that during the continuous casting process, it leads to the defect formation and that it is essential to understand the reason behind it[21–23]. So, even though the reaction seems simple at first sight (Liquid + $\delta \rightarrow \gamma$), it is in fact very complicated because it involves the interaction between 1 liquid and 2 solid phases, which have different properties. However, this reaction is intriguing once the behaviour of the steel during the peritectic reaction becomes apparent.

2.2 The continuous casting process

Casting and solidification are the most important processing steps for metals and alloys, which allow the casting product to be produced with an appropriate geometry. Continuous casting can be used to form not only steel slabs, blooms, billets but also sheets directly by including rolling mills as part of the steel making process at plant [24].

The principle of the continuous casting process is illustrated in Figure 2.1. During this process, the molten steel must be transported at a required flow rate from the ladle into the bottomless water-cooled copper mould [25]. The solidification process commences at a temporary bottom, attached to a dummy bar. It is pulled through the strand guidance at the beginning of the casting process and then cut off from the solidified steel at the end of the caster. [20] As soon as the molten metal reaches the area in the mould, it starts to solidify due to the heat transfer from the

metal towards to mould. The thickness of the solidified steel shell increases down the length of the mould and it must have such a thickness that it can withstand the ferrostatic pressure from the molten metal in the interior of the steel shell when it loses contact with the mould wall and approaches the water nozzles and support rolles (secondary cooling) [26]. While the steel solidifies, the mould oscillates to avoid sticking of the steel shell with the mould. Mould powder is added on the surface of the steel to provide thermal isolation of the molten metal and to improve the lubrication and heat extraction towards the mould [20].

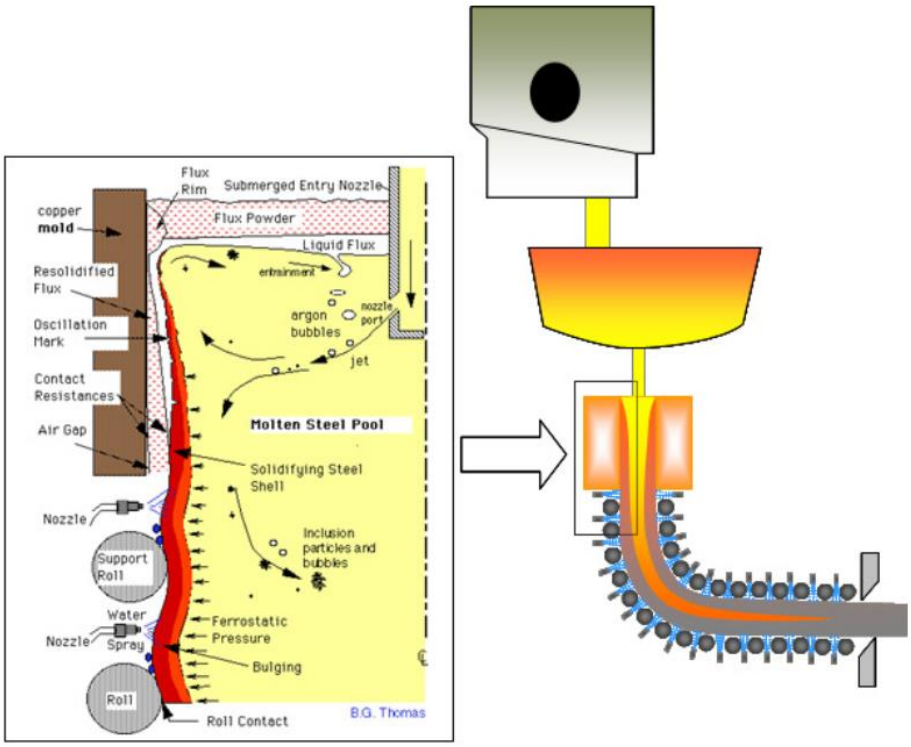

Figure 2.1 Schematic illustration of the continuous casting process [20,25]

The variation of the heat transport in different parts of the water-cooled copper mould, solid and molten metal during continuous casting process is illustrated in Figure 2.2 in four steps:

A – thermal conduction through the solidified shell;

B – heat transfer across the air gap between the shell and the chill (water-cooled) mould;

C – thermal conduction the chill-mould;

D – heat transfer between the chill-mould and the cooling water.

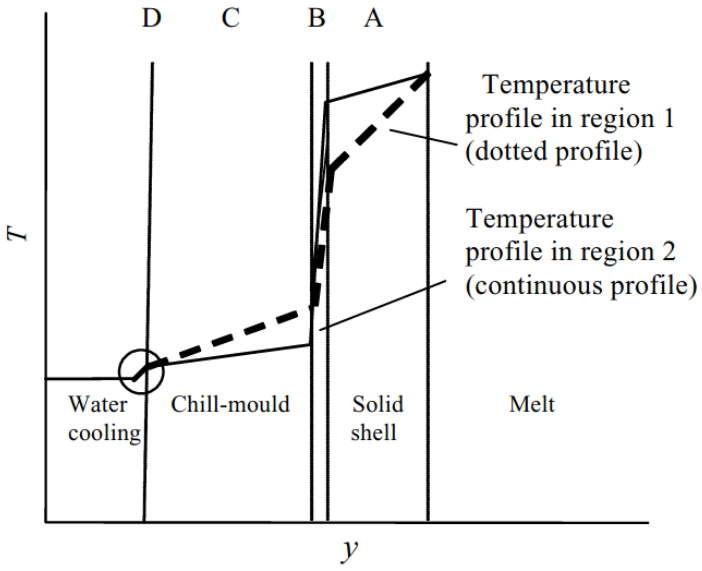

Figure 2.2 Temperature distribution in the chill-mould, solid metal and melt during continuous casting [26]

Due to the difference in the temperature distribution, the cooling rate of the steel during continuous casting process varies from 10^2 °C/s (at the steel shell closer to the copper mould) to 10^{-2} °C/s (closer to the middle of the solidified slab, bloom or billet). [27,28]. The interface morphology (the shape of the growing dendrite) changes, depending on the thermal gradient in the liquid phase at the S/L interface. The distance between the dendrites (dendrite arm spacing) varies between 20 to 200µm [28]. When the thermal gradient in the liquid is larger than the liquidus temperature gradient, the interface will be planar. For small constitutional undercooling, the dendrites will start to grow in the solidification direction, resulting in the cellular interface, as illustrated in Figure 2.3 as $G_{p/c}$ during the planar-to-cellular transition. When the constitutional undercooling increases due to the lower thermal gradient, the distance between the cells increases, resulting in the formation of dendrites. This is a cellular-to-dendrite transition and takes place at a temperature gradient $G_{c/d}$. Both cellular and dendritic growth occurs it the opposite directions to the heat extraction and is called columnar growth. When the undercooling is even higher, equiaxed grains can grow in the liquid away from the interface, and the dendritic to equiaxed transition is shown at $G_{d/e}$ in Figure 2.3. When the thermal gradient is flat (G_t=0), it will lead to the formation of complete equiaxed structure because the driving force for the columnar structure will be minimal [28].

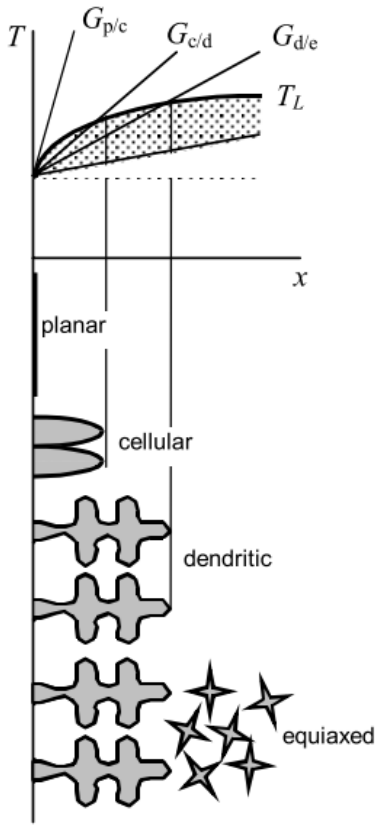

Figure 2.3 Correlation between the thermal gradient at the interface and the interface morphology [28]

As illustrated in Figure 2.4, when the heat flux is imposed, the tip of the dendrite grows into a liquid phase while the B-atoms rejected at the interface and diffused into the liquid (J_B). It leads to the creation of the solutal diffusion boundary layer, ΔC, which does not have the same composition as the original liquid and it is used as heat extraction. The ratio of the concentration change at the tip of the dendrite, ΔC, to the equilibrium concentration difference, ΔC^* is called supersaturation. The temperature at the tip of the growing dendrite, T^* will define the solute undercooling, $\Delta T_{C,}$ or the degree of supersaturation (via the phase diagram), $\Omega=\Delta C/\Delta C^*$. The supersaturation (or the associated undercooling, ΔT_c) characterises the driving force for the solute diffusion at the dendrite tip in the metals.

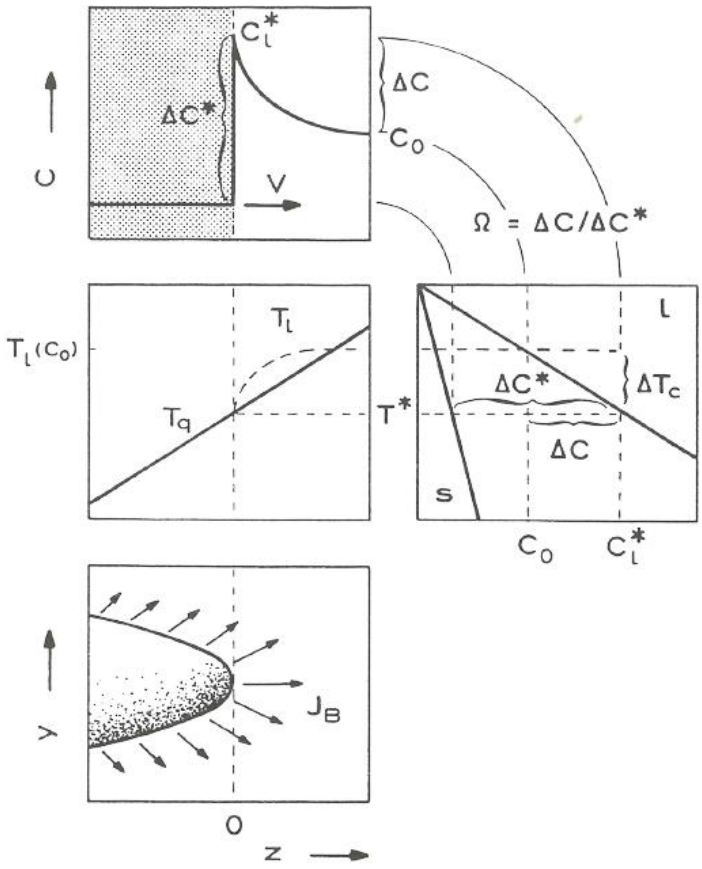

Figure 2.4 Solute rejection at the tip of an isolated dendrite

The distribution of the rejected heat and solute elements in the metal affects the form of the dendrite tip, and the shape of the dendrite tip influence the growth rate of the dendrite [29]. It suggests that the more non-uniform distribution of the alloying elements can lead to the slower growth of the dendrite. Although the increase of the supersaturation (undercooling), leads to the increase in the growth rate of the new phase [29].

2.3 Solidification process

The solidification process is accompanied by a change from a short-range atomic order to a long-range, and this process results in the latent heat of fusion as a result of the energy release [30]. Unlike pure metals, which solidify at one temperature, the alloys transform from liquid to solid state gradually, over a wide temperature interval [31]. During the Continuous Casting (CC) process the steels or alloys consist of both solid and liquid phases, and while they are solidifying, they form the microstructure, which has a direct influence on the mechanical properties of the casting and can be controlled during the solidification process [7].

The primary requirements for the solidification process are nucleation and growth, which are affected by the solidification undercooling, heat evolution and therefore cooling rate. Eventually, it affects the final grains number and size. Higher cooling rate leads to the formation of the higher number of substrates, so the grain density increases. The example of the typical grains numbers is illustrated in Figure 2.5 for cast iron with different carbon equivalents (CE) [28,32–34].

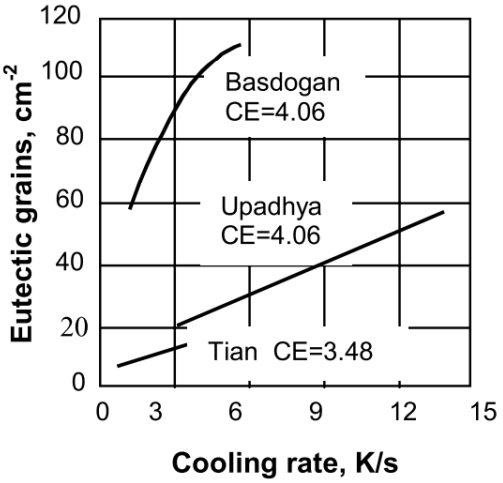

Figure 2.5 Variation of the volumetric eutectic grain density as a function of cooling rate for cast iron [28,32–34]

Nuclei are the solid particles of a micron-scale size that are used as substances for growing grains [7]. After the nucleation is completed, the growth and therefore solidification occurs only if, by doing so, the system can lose energy [35]. Therefore, it is essential for the heat to be removed during the crystallising process and transferred to the environment to complete the solidification reaction [36].

The solidification morphology changes, depending on a combination of factors, like the diffusivity of the solute and thermal conductivity, thermal gradient across the interface and the velocity of the moving interface. Experimentally it was found that a planar interface is formed if the solidification rate is low. By increasing the solidification rate, the interface changes to cellular, and then to dendritic [37].

During the continuous casting process, the nucleation starts close to the mould wall or in the liquid metal and the newly formed crystals grow towards the opposite direction from the heat flow, leading to the formation of the dendrite (tree-like) morphologies. As illustrated in Figure 2.6, three regions can be distinguished during solidification: the solid, solid plus liquid (so-called mushy zone), and the liquid region. During initial shell growth, before the liquid fully

solidifies in the interdendritic region and while the secondary dendrites are located close to the primary dendrites, without overlapping with the other secondary dendrites, there are no mechanical bonds between the primary dendrites. At this stage, the solidified steel shell has little or no strength and is sensitive to the defect formation. Upon further solidification, the dendrite tips grow and adjoin the other dendrites and form a coherent dendritic network, so the strength of the solidified shell increases [20].

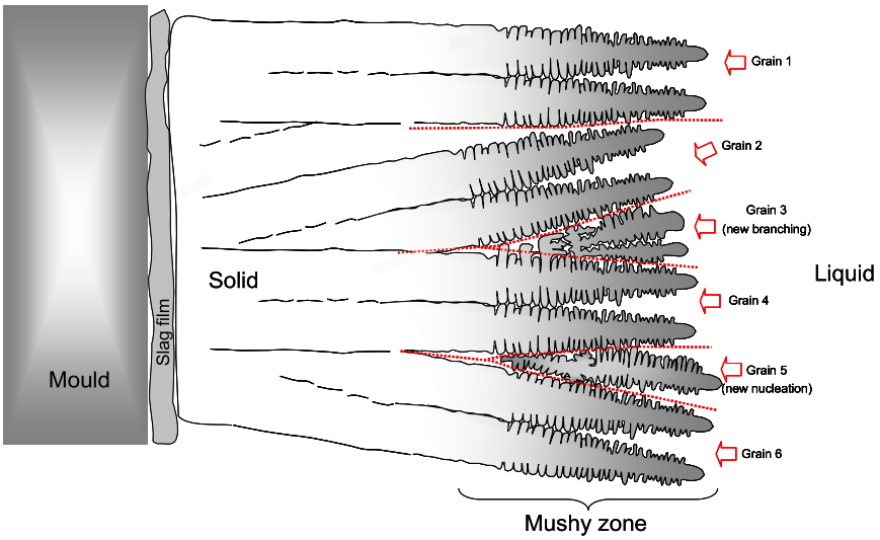

Figure 2.6 Schematic illustration of the dendrite's growth and branching. The hypothetical grain boundaries are marked in the dashed red lines [20]

The approach described above is taken as a basis for the assessment of the solidification of the peritectic steels. Therefore, if there are any parameters, which prevent the development of the dendrites during solidification, it may subsequently cause defect formation during the continuous casting process.

2.4 Peritectic Reaction and Transformation in Low Carbon Peritectic Steels

The name *"peritectic reaction"* was given to this system because a secondary phase (γ) normally grows around the *periphery* of the primary phase (δ) [38]. However, the concept of a "peritectic" did not have a complete terminology until 1974, when Kerr et al. [39] gave a precise definition to a peritectic system by distinguishing the peritectic reaction ($L + \delta \rightarrow \gamma$) and peritectic transformation ($L \rightarrow \gamma$ and $\delta \rightarrow \gamma$), shown in Figure 2.7. During the peritectic reaction, liquid and δ become separated by γ, which has a concentration gradient across the width of the γ layer because local equilibrium is maintained at the respective interfaces. As illustrated in Figure 2.7, the concentration at the δ/γ interface is γ_1, and the concentration at the L/γ interface

is γ_2 at the undercooling temperature below the peritectic reaction [10]. After liquid and δ are separated by γ, the peritectic transformation occurs, when the liquid solidifies as γ and δ transforms to γ.

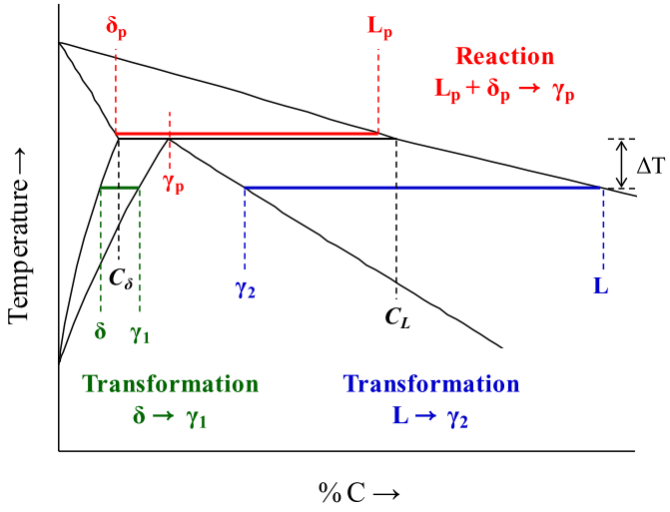

Figure 2.7 Peritectic reaction and subsequent phase transformation [10]

The idea of distinguishing the peritectic reaction and transformation was supported by Fredriksson [38] who explained that the peritectic reaction is controlled by diffusion through the liquid phase. However, when δ is covered by γ, the situation changes entirely because the reaction can only be continued by the diffusion of γ, which is much slower than the diffusion in the liquid phase [40]. In this case, the reaction rate will drop, and the peritectic reaction may not even have time to be finished, which is why the next event, followed after that, was called a peritectic transformation. Distinguishing these two events – the peritectic reaction and transformation – is an essential step towards understanding the solidification behaviour of peritectic steels.

The events, which occur during peritectic solidification were summarised and schematically illustrated by Stefanescu [41] as shown in Figure 2.8. The peritectic solidification starts with a peritectic reaction, when all three phases, liquid, δ and γ are in contact with each other and γ grows along the L/δ interface, compelled by liquid super-saturation. The solute rejected by the γ phase will diffuse through the liquid to the δ contributing to its dissolution. After the liquid and δ are isolated by γ, the peritectic transformation starts, so δ transforms to γ by solid-state diffusion through the "peritectic γ phase", and γ also grows by direct solidification in the liquid [41].

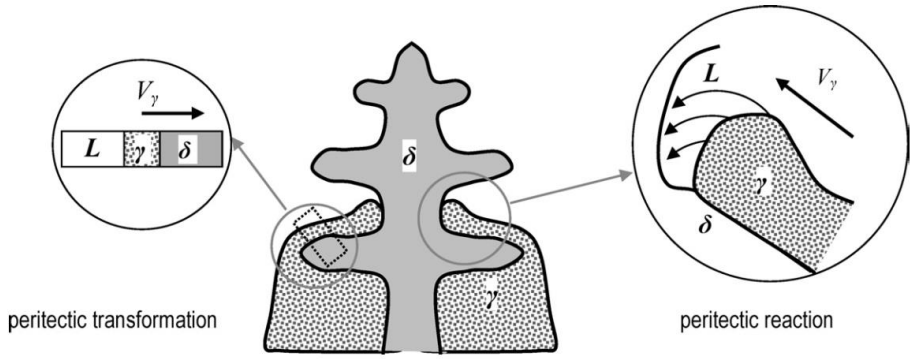

Figure 2.8 Mechanism of peritectic solidification [41]

Different transformation sequences can be distinguished in steels during solidification, which are illustrated in Figure 2.9 and summarised in Table 2-1. Different ranges in the Fe-C phase diagram are shown with the points C_A, C_B and C_C. The steels which undergo transformation sequences shown in range II (from C_A to C_B) are of special interest because in this case the $\delta \rightarrow \gamma$ transformation starts in the solid-liquid region and ends in solid ($L \rightarrow L + \delta \rightarrow \delta + \gamma \rightarrow \gamma$). These steels are called hypo-peritectic, and they are sensitive to the defect formation during (such as hot tearing, depressions and in the worst case breakout) continuous casting process. The steels which undergo transformation sequences within range III ($L \rightarrow L + \delta \rightarrow L + \gamma \rightarrow \gamma$) are called hyper-peritectic (from C_B to C_C). The $\delta \rightarrow \gamma$ transformation, in this case, starts and ends in the solid-liquid regions and they have fewer surface defects compared to the hypo-peritectic steels [42].

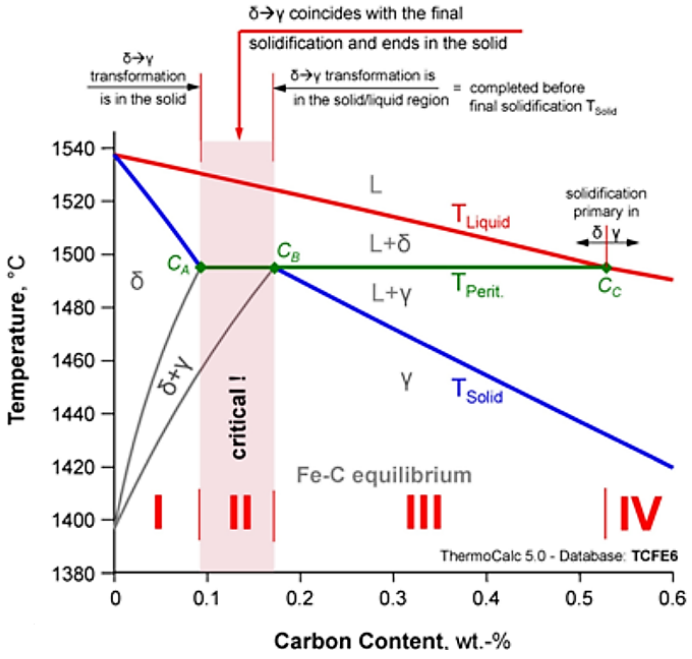

Figure 2.9 Fe-C equilibrium diagram with the critical peritectic range [42]

Table 2-1 Different transformation sequences in the Fe-C systems [42]

Range	Position	Phase sequence	Characteristics
I	Left of C_A	$L \rightarrow L+\delta \rightarrow \delta \rightarrow \delta+\gamma \rightarrow \gamma$	Primary δ-Fe solidification
II	Between C_A and C_B = *hypo-peritectic*	$L \rightarrow L+\delta \rightarrow \delta+\gamma \rightarrow \gamma$	Peritectic transformation coincides with the final solidification
III	Between C_B and C_C = *hyper-peritectic*	$L \rightarrow L+\delta \rightarrow L+\gamma \rightarrow \gamma$	Peritectic transformation occurs in the solid/liquid two phase region
IV	Right of C_C	$L \rightarrow L+\gamma \rightarrow \gamma$	Primary γ-Fe solidification

The focus of the current research is on hypo-peritectic steel, although various tests were also done for the hyper-peritectic steel.

2.5 Thermodynamic Calculations

The thermodynamic calculations are based on the thermodynamic database obtained by assessment of experimental data using the Calphad (calculation of phase diagrams) method [43]. The equilibrium calculations can be made by a minimisation procedure of the Gibbs energy as a function of composition, temperature and pressure for every given phase in the system [44].

The methodology of multicomponent phase diagram calculations using Calphad or a similar thermodynamic approach is illustrated in Figure 2.10. It must be noted that significant progress in understanding the phase transformations could not have been made without the availability of the first generation of phase diagram calculation software developed in the 1980s and 1990s, such as Newton Raphson's method of calculation of phase diagrams by Lukas et at. [45], the

Thermo-Calc database system [46] or a chemical equilibrium calculation program called ChemSage [47,48].

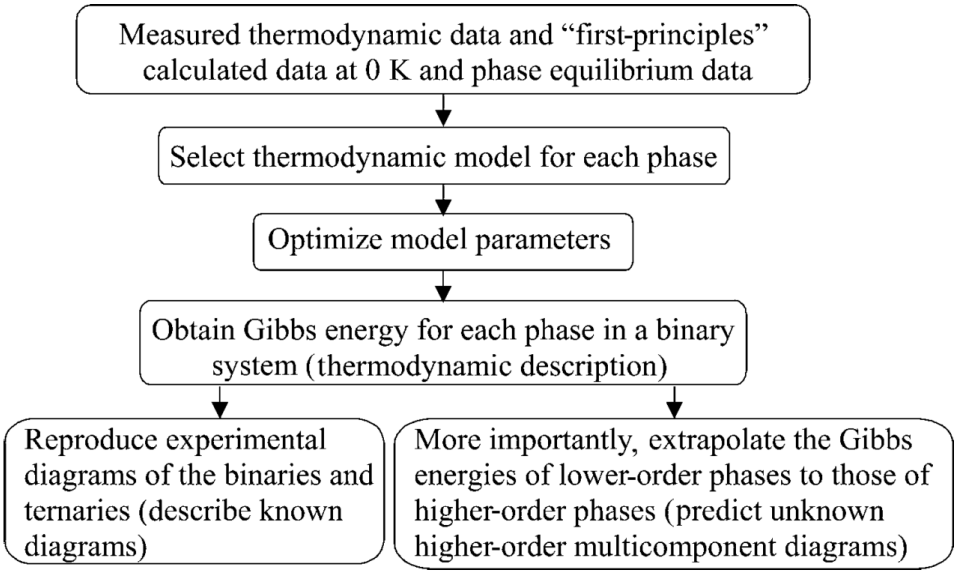

Figure 2.10 The Calphad or phenomenological thermodynamic approach to obtain a thermodynamic description or database of a multicomponent system [47]

Thermo-Calc [49], is a commercial software package, which is used worldwide for thermodynamic and phase diagram calculations of multi-component systems for many types of materials. It can predict the phase transformations of steels and alloys in mainly equilibrium conditions by processing multi-component systems defined with up to 40 elements [44].

Thermodynamic calculation is a good method to understand the phase transformation of the material under equilibrium conditions. However, the accuracy of such calculations is limited by the database of chemical compositions available, as in the absence of such a database the calculations cannot be extended to new materials [19,42]. Moreover, real-world casting processes are under conditions significantly deviating from equilibrium. Therefore, it is also essential to experimentally explore the solidification behaviour of steels considered in this research to understand solidification not only in equilibrium but also in non-equilibrium conditions.

2.6 Thermal analysis of Peritectic Steels

Thermal analysis is a commonly used experimental measurement technique, which allows us to obtain data and generate analysis of measurements relatively quickly and within a degree of local thermodynamic equilibrium [50]. The specific sample characteristics can affect the

interpretation and analysis of the thermal measurements. Therefore, thermal cycles and holding treatments must be taken into account when interpreting the thermal analysis signals. In real-time conditions, the phase evolution of multicomponent systems, like peritectics, can have different behaviour compared to that in equilibrium, so this fact must also be considered when interpreting the solidification behaviour of peritectic steels.

Experimentally, the peritectic phase transformations in steels can be evaluated using Differential Scanning Calorimetry (DSC) tests, which capture the variation of enthalpy during phase transformations in Steel samples, as they are slowly heated (until melted) or cooled (until solidified) [50]. During slow heating (around 0.5 °C/s), DSC curves are consistent with equilibrium transformation temperatures and melting normally occurs at or just above the thermodynamic melting temperature [51]. Upon cooling, undercooling is required to provide the driving force for nucleation, so usually, the solidification process commences at a temperature lower than the thermodynamic liquidus temperature unless cooling is infinitely slow [17]. Thus, DSC cooling curves tend to show discrepancies compared to equilibrium phase diagrams during solidification of steels, and as such DSC curves of melting and solidification typically exhibit asymmetry [51,52].

2.6.1 Overview of the Differential Scanning Calorimetry (DSC)

Differential Scanning Calorimetry (DSC) is currently the widest spread technique for recording and characterising the transformations associated with enthalpy change (exo- or endothermic reactions). The DSC equipment consists of a furnace, two crucibles and thermocouples under the crucibles (Figure 2.11). The sample is positioned inside one of the crucibles and the second crucible, called the reference, is empty. The differential signal of the DSC equipment is the power difference needed to retain an equal temperature between the sample and the reference during controlled heating and cooling. Usually, this signal is given in units of Watts per unit sample mass [50]. To obtain the enthalpy data in Joules per gram, the calibration file should be used during the test. This file can be created based on the DSC signal of pure metals like Zn, Al, Ag, Au, etc., for which enthalpy data is well known.

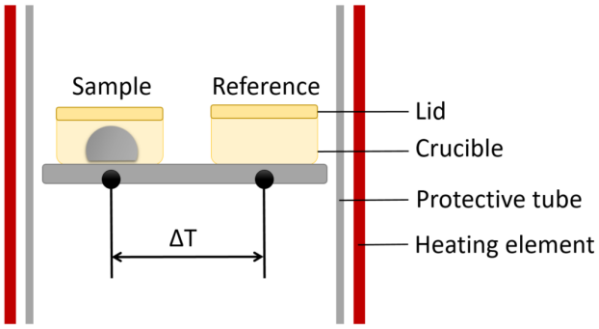

Figure 2.11 Schematic illustration of the DSC sensor (not to scale)

It is critical to define and control the inert gas flow during the test to obtain accurate DSC measurements. A metal-housed mass flow control system (MFC) offers ideal control of the atmosphere around the sample during the test [53]. Two purge gas channels supply the inert gas into the furnace, and the protective gas channel supplies the gas to the balance system. During the test, the inert gas moves through the radiation shield and sample carrier and exits through the exhaust pipe on the top of the equipment. The sample carrier is separated from the heating elements by the protective tube. The evacuation system can be used to pump down the furnace before filling back with an inert gas to reduce the oxygen atmosphere before starting the test.

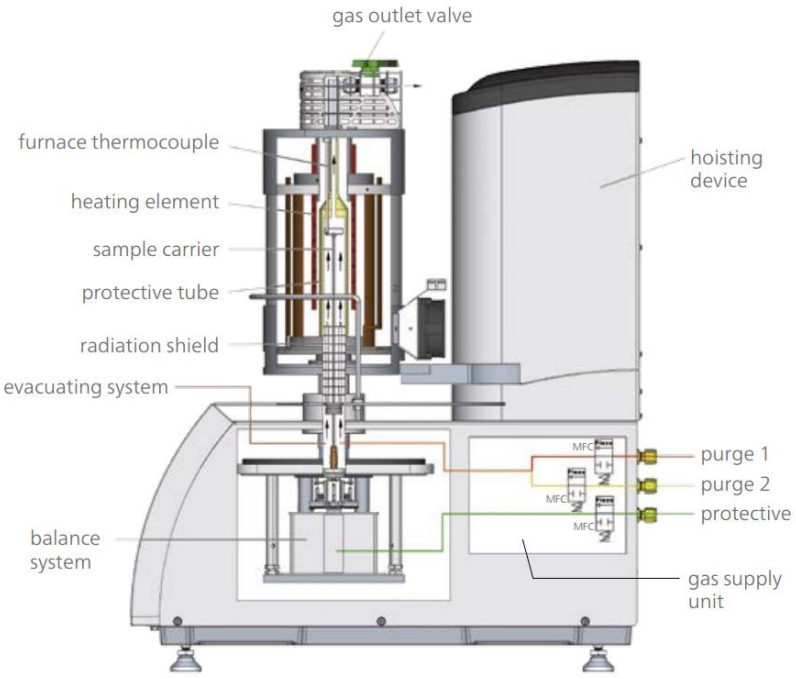

Figure 2.12 Design of the Differential Scanning Calorimeter used in the current research [54]

The oxidation of metal alloys is inhibited, therefore only a pure oxygen-free atmosphere can give well-defined signals of the phase transformations at higher temperatures. To be able to carry out the DSC measurements in a very pure atmosphere, high purity inert gas (6N Argon)

must be used during the test, combined with an oxygen getter material (Zirconia) “ring”, which is illustrated in Figure 2.13 [55]. In addition, titanium slugs can also be placed on the radiation shield to reduce oxygen traces in the atmosphere [56] further.

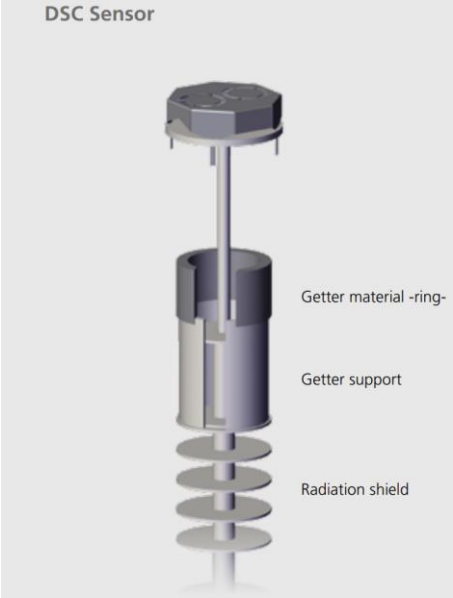

Figure 2.13 Oxygen trap system for reduction of residual oxygen during the DSC test [55]

Figure 2.14 shows how the signal is generated during heating under ideal conditions. On heating, due to the heat capacity of the sample, the reference side (crucible without the sample) normally heats faster than the sample side, so the reference temperature (T_R, green) increases faster than the sample temperature (T_P, red). During the constant heating rate, the red and green curves look parallel until an exo- or endothermic reaction occurs in the sample. For example, if the sample starts to melt at t_1, the temperature of the sample does not change at that moment (the moment when the red line becomes horizontal and do not rise). However, the temperature of the reference is not affected by the sample’s melting, and it continues to increase steadily. After the sample is completely molten, the sample temperature increases again (the red line starts to rise), as shown in Figure 2.14 after the point in time t_2, until it reaches the same temperature as the reference one (green curve) [54]. In this case, t_1 is the onset temperature of the phase transformation, i.e. the temperature when the phase transformation starts. Usually, the software for the DSC equipment determines this temperature automatically, which was done for the experiments conducted for the current research. However, the results were also checked and corrected manually by plotting the tangent to the DSC curve to understand the temperature when the phase transformation starts. It was done if the software showed the artefacts in the experimental results.

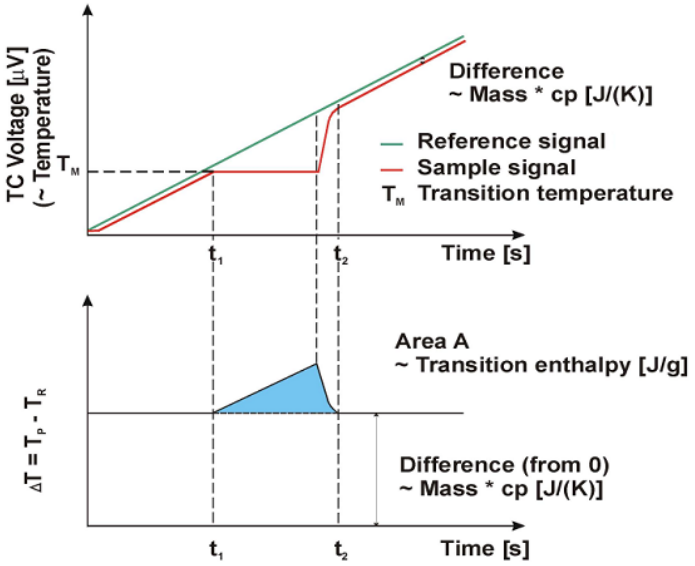

Figure 2.14 Signal generation in a heat-flux DSC [56]

The lower part of Figure 2.14 shows the differential signal (ΔT) of the sample and reference temperature curves. The generated (blue) peak area provides the information of the endothermic melting process and can be shown as a Voltage change (µV/mg) or correlated using the enthalpy data and converted to Joules per gram (J/g).

Establishing the liquidus and solidus temperatures for metals and alloys is the most widespread measurement of determining phase diagrams. Other thermodynamic temperatures, associated with complex phase transformations, like eutectic or peritectic, can also be found and characterised to obtain more accurate phase diagrams. In addition, supercooling and its effect on phase transformations can also be studied using the DSC technique.

2.6.2 Previous DSC studies of solidification behaviour of peritectic steels

A thorough review of the literature has yielded a single study using DSC to identify the peritectic reaction during solidification of steels, which was reported by Wielgosz and Kargul [57]. The authors conducted the DSC tests at slow heating and cooling rates of 0.08 and 0.33 °C/s on the peritectic steel samples, which have the comparable composition to those used in the current research. As illustrated in Figure 2.15 (a), they primarily observed three adjacent DSC peaks upon melting, associated with γ to δ, γ to liquid and δ to liquid transformation, so the peritectic reaction was reported to start at the beginning of the second peak.

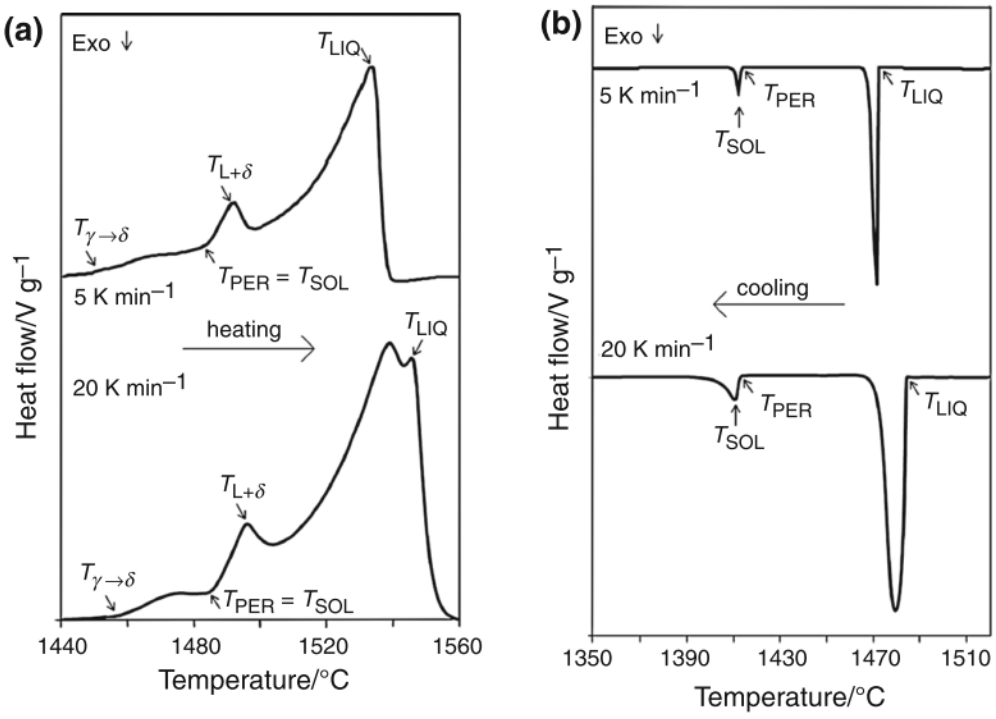

Figure 2.15 DSC curves of peritectic steel obtained during heating (a) and cooling (b) rates of 0.08 and 0.33 °C/s [57]

However, they observed only two distinct DSC peaks upon solidification and suggested that the peritectic reaction in this case also occurs at the beginning of the second peak upon cooling, as shown in Figure 2.15 (b). The first solidification peak was attributed to δ nucleation and growth, which was not deemed to have completed and was followed by a stagnant period of the two-phase structure of L+δ. The second peak was thus attributed to the peritectic reaction, which occurred at a much lower temperature (1413°C) compared to the one upon heating (1486°C). This interpretation suggests that between the first and second DSC peak, which spans a large temperature range of about 70°C, δ dendrites stay in equilibrium with the liquid phase, thus resulting in a large undercooling of the liquid and inconsistent results with thermodynamic calculations.

DSC only provides thermal data of the sample, and therefore distinguishing between different phases can be problematic typically when trying to identify simultaneous multi-phase transformations, therefore additional information is required to interpret DSC curves as such phase transformations are expected in peritectic steels.

Even though currently there is one available study of the DSC cooling curves of low carbon peritectic steels [57], the interpretation of the DSC curves is questionable. Thus, a thorough explanation of the solidification phenomena of peritectic steels is still lacking. The analysis of

the solidification behaviour of peritectic steels based on the DSC cooling curves are conducted in the current research, and the results are discussed in detail in Chapter 4.

2.7 High-Temperature Microscopy to Study the Solidification Behaviour of Peritectic Systems

Initially, it was impossible to observe a peritectic reaction and transformation under a microscope, because it occurs at around 1500°C, and high-temperature metallography analysis was not available. Then Emi and his colleagues [58] developed suitable equipment in 1996, called a high-temperature Confocal Scanning Laser Microscope or CSLM.

This innovative technique facilitates observation of the material's surface perturbations as a result of phase transformations on the microscopic level. Using CSLM, it became possible to develop an extensive database for the phase transformation behaviour during controlled heating up to 1700°C and cooling of steels, alloys, slags and fluxes [59].

2.7.1 Overview of Confocal Scanning Laser Microscope (CSLM)

The schematic diagram of the high-temperature Confocal Scanning Laser Microscope (CSLM) is illustrated in Figure 2.16 [22]. The sample is set in a rectangular high purity Al_2O_3 crucible, held in a platinum holder (Figure 2.16 (a)) and positioned in the upper half of the gold-plated ellipsoidal cavity of the chamber. The location of the sample can be horizontally adjusted, and it is placed in the focal point in the upper part of the furnace (Figure 2.16 (b)). The top of the ellipsoidal cavity has a viewing window covered airtight with a quartz disk. The halogen bulb, which is a source of heat, is located at the other focal point in the lower part of the cavity. It is capable of heating up the sample at a maximum rate of about 5°C/s [22] and cooling down at a rate of up to 50°C/s.

The CSLM has a He-Ne laser beam (1.5 mW, 632.8 nm) that is delivered via a half mirror (polarising 45 deg.) and an objective lens (with long focal length) to the surface of the sample. The deflected beam is then delivered through the half mirror (polarising further 45 deg.) and a beam splitter to a CCD (charge-coupled device) sensor to convert it to a digital value. The intensity of the laser beam of 0.5μm diameter is so high that the small difference in emissivity of the solid and liquid steel and a shallow wave of the sample surface is clearly identified.

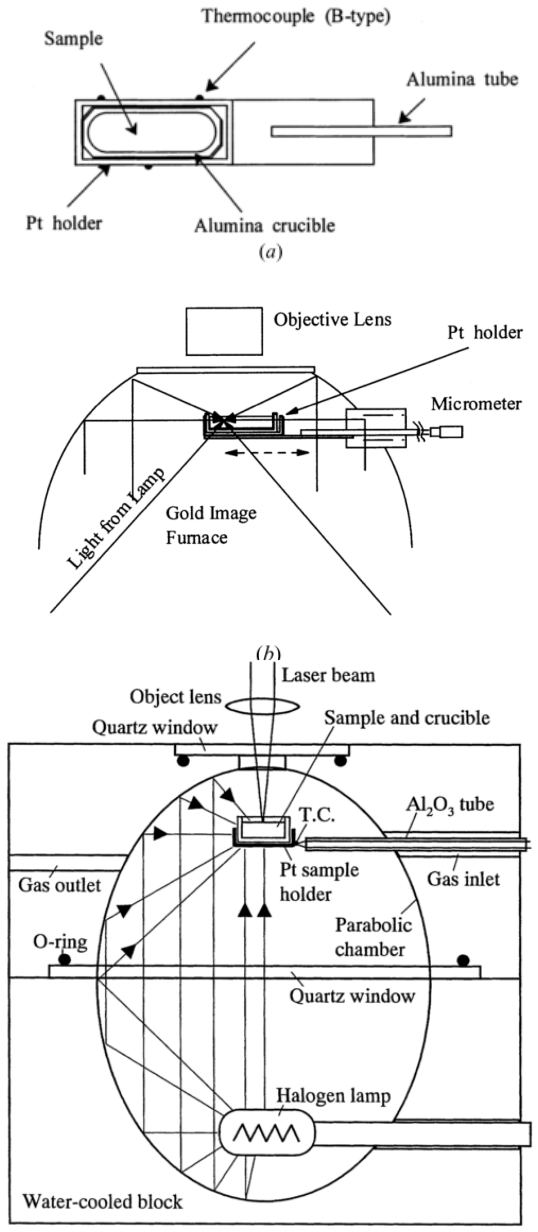

Figure 2.16 (a) and (b) Schematic illustration of the high-temperature Confocal Scanning Laser Microscope and sample holder [22]

The shape of the sample used during the CSLM test can vary depending on the aim of the experimental results. Figure 2.17 illustrates how different crucible shapes affected the observation of the peritectic reaction in a Fe-0.43 wt.%C alloy. In the conventional CSLM technique, the rectangular (Figure 2.17 (a)) and cylindrical (Figure 2.17 (b)) crucibles are used to melt the material inside it. However, it was reported ([60]) that after the sample is fully molten, the solidification begins from the crucible wall up the meniscus' area. So it becomes difficult to observe the growth of γ between liquid and δ because the liquid phase moves out of focus and the γ layer is too thin to be able to distinguish it, as shown in Figure 2.17 (a). This

technique is called horizontal directional solidification because the sample starts to solidify from the cold end of the crucible and planar crystals grow directionally towards the opposite side of the crucible where the highest peak of the thermal gradient is located [22].

A comparable situation was observed during solidification of a large steel sample, when it completely covered the bottom of the cylindrical crucible (Figure 2.17 (b)), so a presence of meniscus exacerbated the observation of the thin γ layer at the L/δ interface.

In the case of the concentric solidification technique (Figure 2.17), usually a sample of 9.8 mm diameter and 100-250 μm thickness is used, so the thermal gradient in the through-thickness direction approaches zero ([21,61]). Using a radial thermal gradient across the sample, the steel is melted in the middle, but the rim of solid material stays around it, causing the formation of a vertical solid/liquid interface. Due to minimal thermal gradient through-thickness of the sample (which is only 100-250 μm thick), the observations made on the surface are representative of the events occurring in the bulk [60]. Therefore, observations of the peritectic reaction become more vivid, as illustrated in Figure 2.17 (c). More detailed information on the experimental techniques described above is given later in this Chapter.

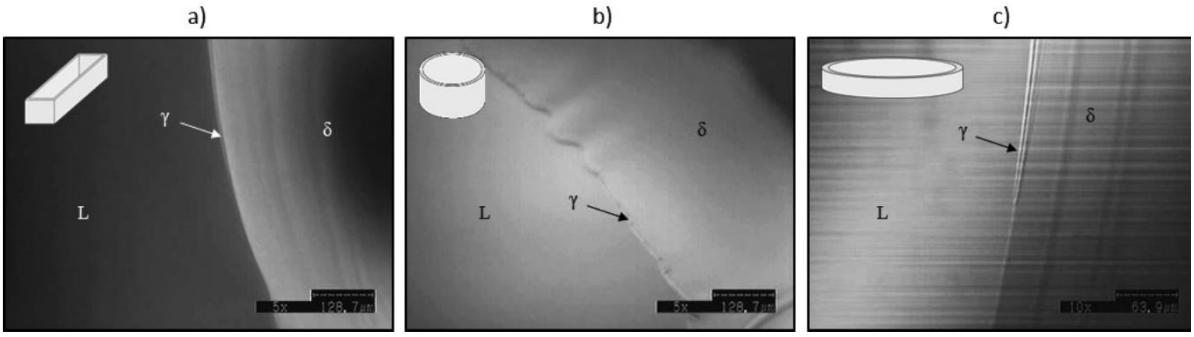

Figure 2.17 Application of different shapes of the sample holders to observe the peritectic reaction in Fe-0.43 wt.%C alloy, using rectangular (a), cylindrical (b) and concentric crucibles (c) [60]

2.7.2 Horizontal directional solidification technique using CSLM

Shibata et al. [22] used the horizontal directional solidification technique in the CSLM using a rectangular crucible (3 mm width, 11 mm length, 3 mm height) to show the first evidence of the peritectic reaction in a Fe-0.42wt%C alloy. As illustrated in Figure 2.18, the authors observed the growth of the γ layer between the liquid and the δ interface, which is a peritectic reaction. This reaction was reported to be very rapid, so the γ layer separated into L and δ within 2/30 s (Figure 2.18 (b – c)).

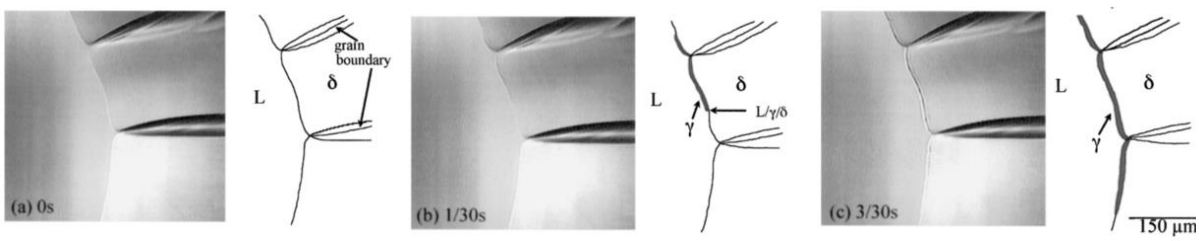

Figure 2.18 Progress of the peritectic reaction along the L/δ boundary observed in a Fe-0.42wt%C alloy [22]

However, it was difficult to observe the peritectic reaction in the low carbon steel (Fe-0.14wt%C) during horizontal directional solidification because the reaction starts when the fraction of δ of the system reaches 0.95 [22]. As soon as this reaction takes place, the remaining liquid phase shrinks and becomes out of focus, which hampers the observation of the peritectic reaction. Therefore, the observation of the solidification process was done in the middle part of the sample where the solidification occurs from the bottom towards the meniscus of the liquid. The cooling rate was controlled manually to slow down the reaction rate, and the observation was made while the last liquid phase was solidifying.

The observed phase transformation sequences are illustrated in Figure 2.19. The growth of γ is seen at 1/30 seconds, which propagates along the L/δ boundary and grows into the δ much faster than towards L as was suggested by Shibata et al. [22].

However, it contradicts the mechanism proposed by Takahashi et al., who suggested that peritectic γ grows towards the L but not toward the δ because the C in the γ does not diffuse into the δ [22,62]. They suggested that instead, the transformation of δ to γ occurs by the nucleation and growth of new γ in the remaining δ. This discrepancy of the results can be explained by the segregation of the C, Mn and other elements towards the observation area (Figure 2.19) during the directional solidification technique, which decreases the solidification temperature of the remaining liquid.

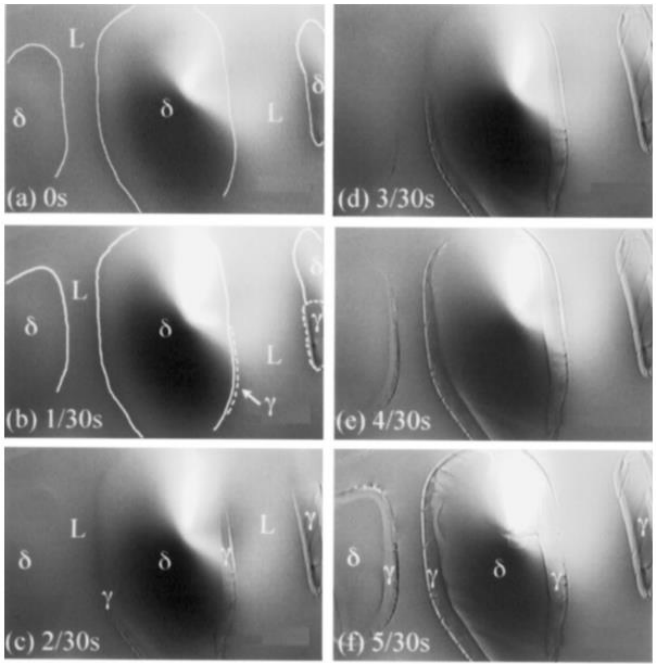

Figure 2.19 (a) through (f) Peritectic reaction and transformation of Fe-0.14wt%C steel during solidification at 1492° (Cooling rate is manually controlled to be less than 0.17 °C/s)

To summarise, the first observation of the peritectic reaction in the CSLM was made using a relatively large sample (for the CSLM technique) in a rectangular crucible using directional solidification technique. However, it was difficult to see the peritectic transformation followed by a reaction. Therefore, the technique was adjusted and allowed us to observe the peritectic transformation while the last liquid phase is solidifying, but it may affect the transformation behaviour as it occurs in the most segregated region of the sample.

2.7.3 Concentric solidification technique

The concentric solidification technique is currently the most popular technique during high-temperature CSLM tests for studying the peritectic solidification because it allows observation of the mechanism and measurement of the kinetics during the peritectic reaction and transformation. This technique was developed by Reid et al. [61] in 2004. It inherently has a radial temperature gradient across the sample with a higher temperature in the centre. Therefore, a pool of liquid metal can be created in the centre, which is contained by a rim of the solid phase of the same metal. The events that occur at the solid-liquid interface, like solidification, segregation and phase transformations can be studied using this technique [60,61,63,64].

As mentioned in at the beginning of this section, the thickness of the sample must be between 100 and 250 μm thickness to achieve zero thermal gradients in the through-thickness direction. At the same time, it is essential to create a thermal gradient along the sample with a maximum temperature in the middle to create a liquid melt pool in the middle of the sample with a thin solid rim of δ around it, as illustrated in Figure 2.20 [1].

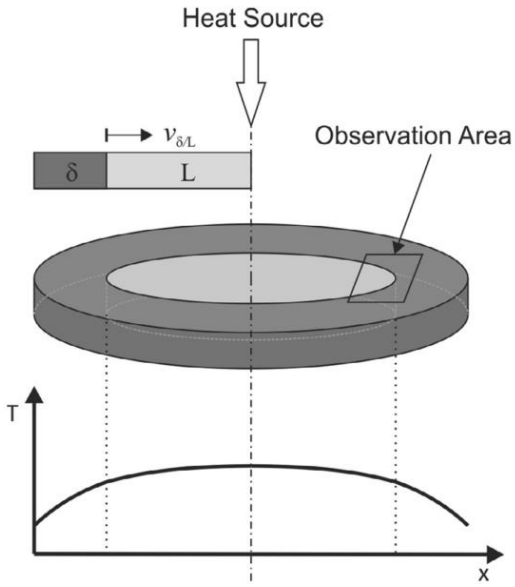

Figure 2.20 Schematic illustration of the thermal gradient along the sample during concentric solidification technique [1]

The solubility of elements in δ is much lower than in the liquid phase, so they diffuse through the δ towards the liquid phase. Therefore, the experimental conditions required for the concentric solidification test, promote high enrichment of the alloying elements towards the centre of the sample as clearly shown in Figure 2.21 [64].

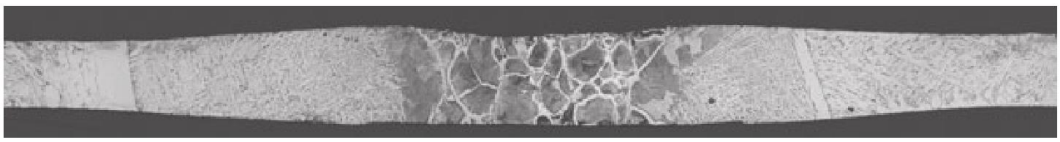

Figure 2.21 Cross section of the concentrically solidified Low Carbon Steel (Fe-0.095wt%C), which shows the segregation in the centre [64]

The inevitable segregation in the centre of the sample changes the composition of the liquid phase [64], which in turns affects the phase transformation behaviour, so the microstructure of the sample which was used during the concentric solidification can visually be divided into several regions with different phases. As illustrated in Figure 2.22. [59,61] the concentrically solidified Fe-0.42wt%C steel sample is divided into 3 phases: pearlite in the centre of the liquid

pool (the highest temperature during the test), α-ferrite beyond the edge of the pool (the lowest temperature) and Widmanstatten ferrite between pearlite and α-ferrite. The carbon content of this sample (0.42%) is higher than that used in the current research (0.07-0.15%), but it is still important to illustrate that segregation of the elements must be taken into account during the concentric solidification technique because the segregation changes the microstructure of the steel samples.

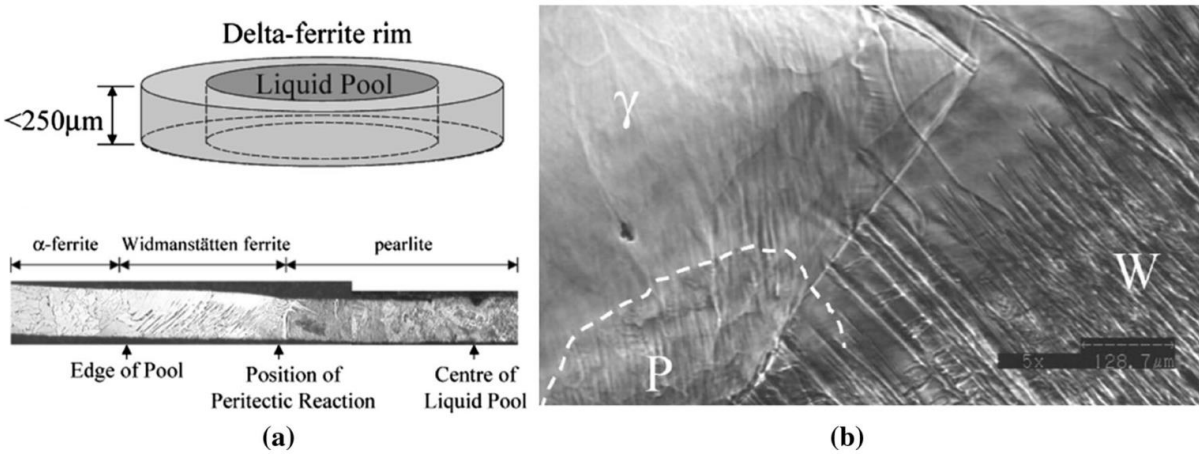

Figure 2.22 (a) Concentric solidification technique and its effect on the microstructure of the solidified specimen and (b) the pearlite/Widmanstatten growth in Fe-0.42wt%C adapted from Reid at al. [59,61]

The segregation and therefore the local composition must be taken into account because it affects the mechanism of the peritectic reaction. Phelan et al. [21] have proven that local composition can affect the peritectic reaction by applying the classic diffusion model to calculate the rate of progression of the peritectic reaction in an Fe-C alloy and comparing it with the measured results. To calculate the maximum velocity of the γ growth, Vγ, as a result of the peritectic reaction, Phelan et al. [21] applied the Bosze and Trivedi diffusion model [65]:

$$V_\gamma = \left(\frac{9}{8\pi}\right)\left(\frac{D_L}{R}\right)\Omega'^2 \tag{2.1}$$

where D_L is the diffusion coefficient of carbon in the liquid ($2 \cdot 10^{-8}\ m^2/s$) [21,22] and R is the radius of the growing γ and is equal to half of the determined thickness of the growing γ plate (1.5μm), and Ω' can be defined as:

$$\Omega' = \frac{\Omega}{\left(1 - \frac{2\Omega}{\pi} - \frac{\Omega^2}{2\pi}\right)} \tag{2.2}$$

$$\Omega = \frac{\left(C_L^{\gamma} - C_L^{\delta}\right)}{\left(C_L^{\gamma} - C_{\gamma}^{L}\right)} \tag{2.3}$$

where C_L^{γ} and C_L^{δ} are the carbon concentrations in the liquid in equilibrium with the γ and δ phases, respectively, and C_{γ}^{L} is the carbon concentration in the γ in equilibrium with the liquid.

It was found that the calculated growth rate of the γ tip of 200 μm/s at 30K undercooling is not in agreement with the measured growth rates of 400 – 12500 μm/s. Even when the γ tip radius was artificially reduced from 1.5 μm to 0.15 μm, it did not lead to an agreement between observed and predicted ranges of γ growth during the peritectic reaction (Figure 2.23).

Shibata et al. [22] have also confirmed that the peritectic reaction in Fe-C alloys cannot be controlled by the diffusion of carbon. However, they found that the velocity of γ growth is 1500 – 5500 μm/s at an undercooling of 5 to 15 K below the equilibrium peritectic reaction, which is less than the velocity measured by Phelan et al. [21] of about 2100 – 6250 μm/s at the same undercooling temperatures for a comparable Fe-C steel. So even though the measured kinetic values for comparable steels were different, both authors concluded that the experimentally determined peritectic reaction rate in Fe-C steels could not be explained by a mechanism where carbon diffusion controls the rate of the peritectic reaction. Instead, a massive transformation of solidification of γ directly from liquid was suggested to be a reason of rapid propagation of γ [22].

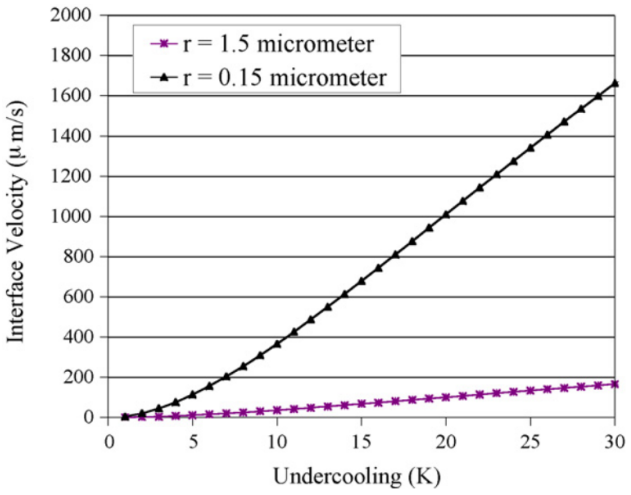

Figure 2.23 Growth velocities calculated using Bosze and Trivedi's method [21,65]

In contrast to these conclusions, McDonald and Sridhar [66] applied the Bosze and Trivedi method [65] to Fe-Ni peritectic alloys and found that the rate of the γ growth during the

peritectic reaction can be accurately predicted using Equations 2.1 – 2.3. This difference in the findings can be explained by the fact that the diffusion flux of interstitial C atoms $J_C \approx 0.15$ μm/s is higher in Fe compared to the flux of substitutional Ni atoms $J_{Ni} \approx 0.007$ μm/s in Fe [63], which subsequently changes the rate of the peritectic reaction.

Griesser et al. [1] have observed the peritectic transformations, followed by the peritectic reaction and found that there is also an effect of a concentration gradient of C in δ, which leads to a change in the mode of the peritectic transformation of δ to γ, as shown in Figure 2.24. The authors observed a massive δ to γ transformation when the temperature of the L/δ interface is below the T_o temperature[1] of the corresponding composition. A more significant difference between the interface temperature and the corresponding T_o temperature leads to a higher driving force for a massive transformation. However, when the local carbon concentration and temperature of δ are above the corresponding T_o temperature (e.g. C_δ^I in Figure 2.24), the massive transformation changes back to a diffusion-controlled transformation of δ to γ. Therefore, depending on the local conditions in terms of concentration and temperature, a changeover in the mechanism of the peritectic transformation can occur.

[1] T_o temperature is defined from thermodynamic considerations as the temperature at which the free energy of the δ and γ phases (in the case of Fe-C alloys) is equal

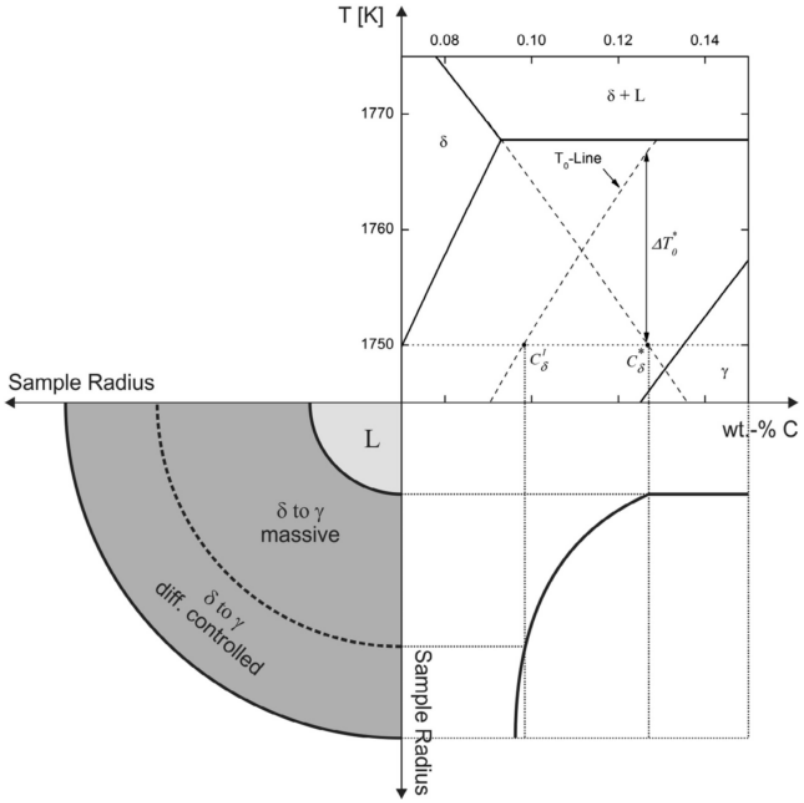

Figure 2.24 Change of transformation mode (massive to diffusion controlled) as a function of the sample radius and the concentration gradient of carbon in δ [1]

An example of when a peritectic reaction and transformation was observed in an Fe-0.18wt%C steel during concentric solidification is illustrated in Figure 2.25 [21]. At the beginning of solidification, the L/δ interface has a planar morphology (t = 0 seconds). At 0.1 seconds, γ has grown along the L/δ interface in the intervening time and into the δ phase. At 2 seconds, the growth of γ into the liquid is measured and reported to be much less compared to the growth into the δ.

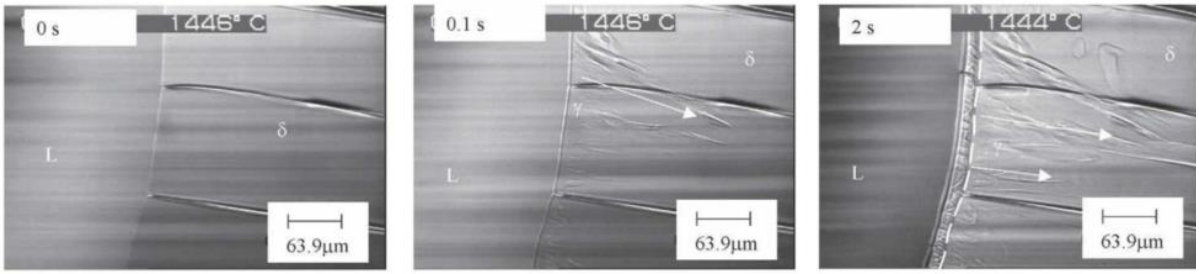

Figure 2.25 Peritectic reaction and transformation observed in Fe-0.18wt%C steel at a cooling rate of 0.83 °C/s. The superimposed broken line in frame t = 2s corresponds to the position of the L/δ interface at t = 0 s [21]

The fact that the growth rate of the γ into the liquid is faster than into the δ was also observed in an Fe-0.14wt%C steel (Figure 2.19 by [22]). As described in Section 2.7.2, it contradicts the

observations made by Takahashi et al. [62], where the authors reported that the peritectic γ grows towards the L but not toward the δ and then the δ → γ transformation occurs after nucleation of new γ. The transformation of δ to γ after the L fully solidifies is also supported by thermodynamic calculations for low carbon steel as described in Section 3.2. In this case, the discrepancy of the conclusions made during concentric solidification and suggested by other sources can also be explained by the segregation of the elements towards the centre of the liquid pool, which decreases the rate at which liquid transforms to solid.

The observations described above show that even though the concentric solidification technique can be an excellent method to measure the kinetics of the peritectic reaction and transformation, the effect of segregation and local temperature must be considered as it strongly affects the transformation behaviour of Fe-C steels and can change the measured values. The amount of the segregated elements depends on the experimental conditions: heating rate, holding time at high temperature, the thickness and size of the sample and chemical composition of the individual sample. The composition of CSLM samples can vary even if they were taken from the same steel grade because depending on the cooling conditions the initial microstructure of the solidified sample has depleted and segregated zones. It occurs not only on the macroscale (10^{0} to 10^{-3} m) but also on the microscale (10^{-6} to 10^{-5} m) [28]. So if the slab with a chemical composition of low alloyed steel grade slab has an interdendritic arm spacing of about 180 µm [20], then the CSLM sample for concentric tests with a thickness of 100 µm (10^{-4} m) [21] can either be depleted or enriched in alloying elements. It depends on the location where the sample was taken from, which can either be along the dendrite's core or at the interdendritic region. A combination of all the influencing parameters described above can be a reason why many authors who study the solidification behaviour of peritectic steel using a concentric solidification technique often find a difference in the measured values or even come to different conclusions.

The concentric solidification technique is currently the most common way of observing peritectic solidification in steels using CSLM because it allows us to observe and measure valuable information – kinetics of the peritectic reaction and transformation. However, it is strongly dependent on the local conditions regarding temperature and concentration of the elements in the observation area during the CSLM test. Moreover, the cooling rate is always restricted during the concentric solidification technique. Therefore, in the current study, another type of solidification technique is used to understand the solidification behaviour of peritectic steels, which is described in the following section.

2.7.4 Droplet solidification technique

The droplet solidification technique using CSLM is less common compared to the other solidification techniques described in Sections 2.7.2 and 2.7.3 for study of peritectic reaction and transformations. A comparable technique was previously used to observe the solidification of AISI 304 Austenitic Stainless Steel [67], crystal growth in Fe-C alloys [68], solidification in Fe and low C steel [69], chemically induced solidification [70] and solidification of peritectic steel [71].

Despite the benefits of both horizontal directional and concentric solidification techniques, mentioned in the previous sections, they can hardly be compared to the solidification conditions during continuous casting, because of the development of thermal gradients and zone refining across the sample. Also, the slow cooling rate, which is used during concentric solidification mainly leads to planar solidification. This may conceal some features of phase transformations during dendritic solidification at faster cooling rates.

Therefore, to observe the events which occur on the sample surface at various cooling rates, a small sample of about 130 mg is completely melted in a round crucible (Figure 2.17 (b)) to form a droplet before solidification [71]. In this case, the bottom of the crucible in not entirely covered with molten steel, as was observed in the previous technique summarised in Section 2.7.2. Instead, a small steel sample forms a droplet, and the wetting behaviour of the molten iron droplet in an alumina crucible is sufficiently high for the curvature of the resultant spherical cap to be imaged with CSLM. Then it is cooled down at higher cooling rates, applicable to CC to observe the solidification behaviour of the sample.

The main benefits of this technique are the observation of dendritic solidification, cooling rate variations, the possibility to study solidification of steel depending on the superheating and undercooling temperatures and the direct correlation of this technique to the DSC results during solidification of steel [71]. Therefore, the droplet solidification technique with CSLM gives a better representation of the solidification conditions in the CC process, compared to concentric or horizontal directional solidification.

2.8 Massive Transformation in Peritectic steels

A massive transformation is described as diffusionless or composition-invariant nucleation and growth of one solid phase from another solid phase [24,72]. Before massive transformation, the precipitation of the second phase with a composition much different from the composition

of the parent phase usually occurs inside the parent grains, even though the grain boundaries are preferred nucleation sites. If the parent phase is brought into the one-phase field of a new phase during cooling, the long-range diffusion will not be required, and the diffusionless transformation will take place. The composition-invariant transformation can also occur if the parent phase is undercooled below the T_0 temperature, which is the temperature when the Gibbs energy is equal in two phases. In this case, the growth rate will increase dramatically. The resulting allotriomorphs will have comparable shape but the size will be larger, and they will have more blocky shapes because their growth would not be restricted by the development of the composition gradient in front of the migration interface [72].

The progress of a massive transformation of δ to γ is frequently observed during the concentric solidification technique in steels which have comparable composition to the peritectic steels investigated in the current research. As illustrated in Figure 2.26, Fe-0.10wt%C steels undergo a massive transformation during cooling, which was completed within 2/30 seconds [63]. The thermodynamic requirement for a massive transformation is that the Gibbs energy of the secondary phase must be smaller than that of the primary phase for the same composition. Similar to the observation described in the previous paragraph, Griesser et al. [63] have also noted, that if two phases have the same composition and Gibbs free energy values, then the critical limit for the massive transformation is the allotropic phase boundary (T_0 temperature). Therefore, when the γ nucleation in steels is sufficiently constrained via diffusive suppression, when the temperature of the L/δ interface drops below the T_0 temperature of the corresponding composition, the massive transformation from δ to γ can occur in this case. Massive $\delta \rightarrow \gamma$ transformation was suggested to be the route for the defect formation during peritectic solidification mainly due to the high kinetics rates [63].

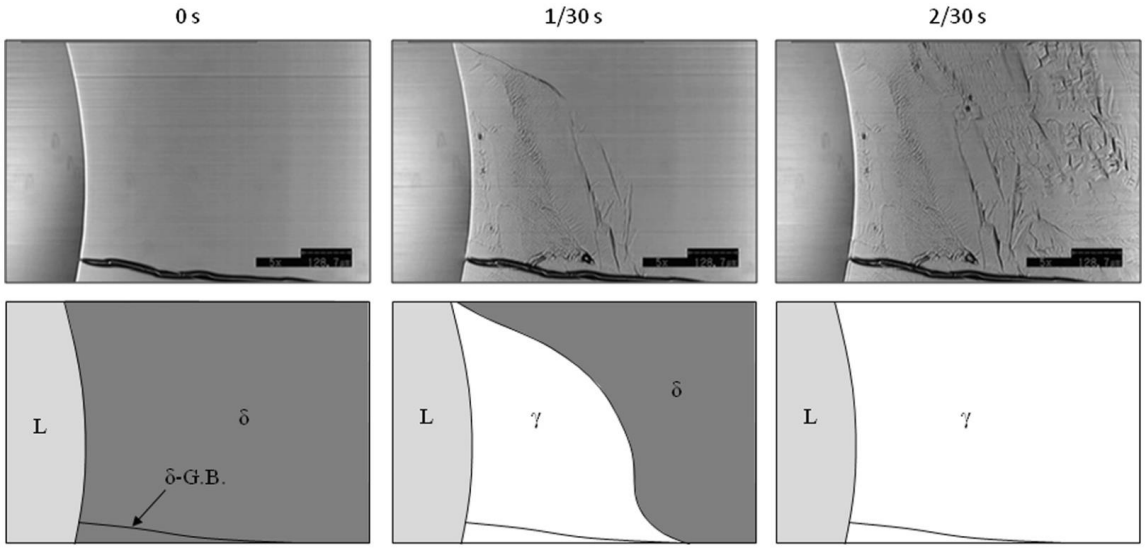

Figure 2.26 Massive transformation of δ to γ in a concentrically solidified Fe-0.10wt%C steel at T_P = 1473 °C [63]

Another observation of the massive transformation in peritectic systems was made by Yasuda et al. using synchrotron radiation X-rays [17]. The schematic illustration of the observed massive transformation in Fe-0.18wt%C steel is illustrated in Figure 2.27. The authors suggest that peritectic γ nucleates at the bottom of the mould, where δ is undercooled below the peritectic temperature at $t=t_3$. Then γ rapidly follows δ dendrite growth towards the tip of the dendrite as a result of massive transformation until it reaches the isothermal plane of the peritectic temperature ($t=t_4$). It was suggested that since the massive transformation occurs in the solid δ, the shrinkage, caused by the δ → γ transformation is not compensated by the liquid flow from the mushy zone. It leads to strain formation on the surface of the solidifying shell [17].

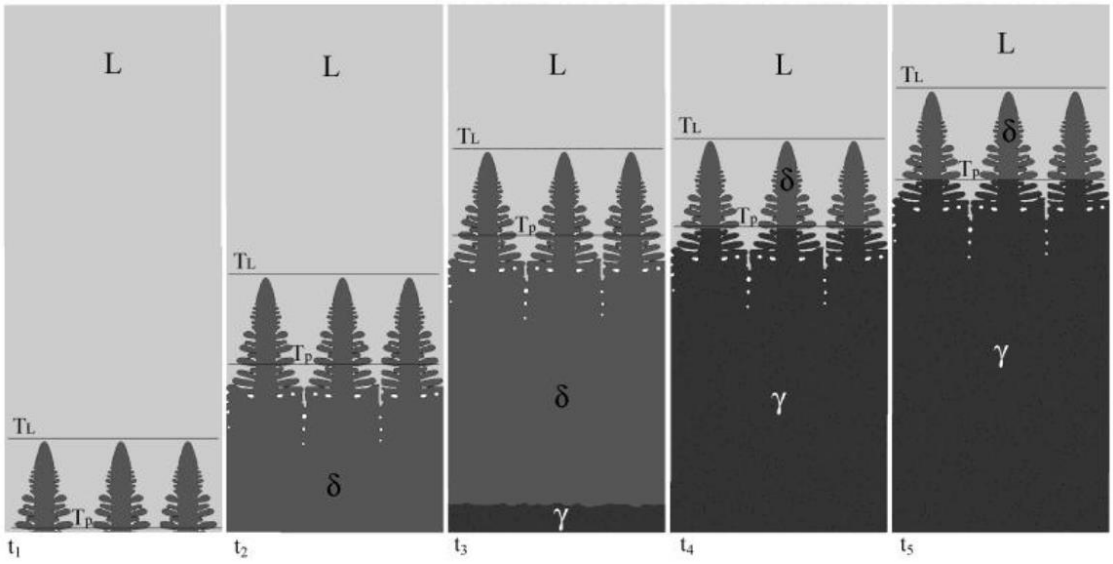

Figure 2.27 Development of solidifying shell and the massive transformation of Fe - 0.18wt% C steel. T_L and T_P are the liquidus temperature of δ and the peritectic transformation temperature respectively.

As summarised above, Griesser et al. [63] and Yasuda et al. [17] have attempted to explain the nucleation and growth of γ during massive transformation in peritectic steels. However, the explanation for this transformation is different. Griesser et al. [63] suggested that γ nucleates at the L/δ interface and grows towards the δ grain, whereas Yasuda et al. [17] proposed that γ nucleates in δ and grows in the opposite detection, towards the liquid phase. Therefore, although the underlying mechanism of massive transformation is not completely known, both authors believed that this transformation is the likely cause of the defect formation during solidification of peritectic steels.

2.9 Remelting Phenomena during Solidification of Peritectic Steels

The remelting of peritectic steels during solidification was originally proposed by Hillert [73] in 1978. Based on the isothermal model, Hillert [73] suggested that during solidification δ remelts partially in front of γ formation due to the segregation of solute. However, at that time, the high-temperature microscopy observations were not available, so this model was not experimentally observed for low carbon peritectic steel.

About three decades after, Phelan et al. [21] and Griesser [30] confirmed that the remelting of δ ahead of the advancing γ tip indeed occurs. However, even though both authors were conducting comparable concentric experiments, they came to different conclusions about the reason for the remelting of peritectic steels. The observations made by Phelan et al. [21] are

illustrated in Figure 2.28. The authors proposed that δ remelts due to the heat release during formation of γ. This is explained by the difference in the latent heat of fusion between δ and γ. The latent heat of fusion of δ is 260kJ/kg [74], and of γ is 272kJ/kg [74], so the latent heat released by the phase transformation of δ to γ is 12kJ/kg ($L_\gamma - L_\delta$). Therefore, when γ nucleates between L and δ as a result of the peritectic reaction, δ remelts because it absorbs the component of the latent heat of fusion liberated by the formation of γ. It was assumed that the latent heat has to be removed for the peritectic reaction to proceed, i.e. for the γ growth along the δ phase [21].

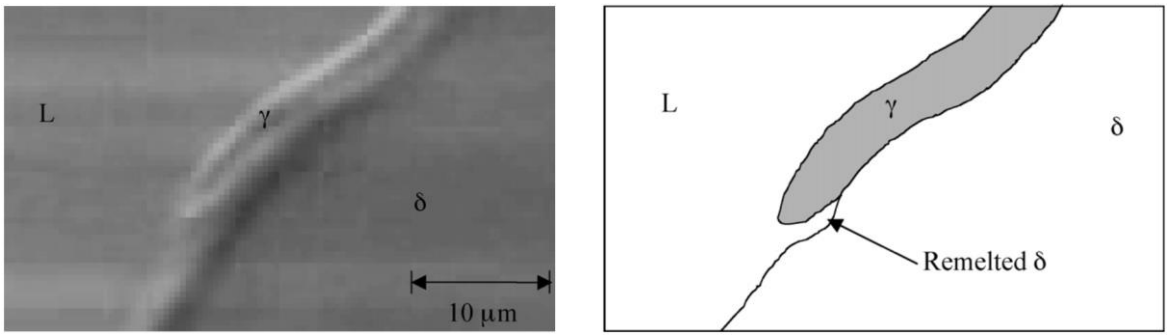

Figure 2.28 Peritectic reaction showing remelting of δ ahead of the growing γ during peritectic reaction observed by Phelan et al. [21]

Griesser et al. [30] have also observed the localised remelting of δ. As illustrated in Figure 2.29, when the γ platelet was held at a stationary position at the L/δ interface (Figure 2.29 a, c, e, g), the phases were in equilibrium at the triple point of L/γ/δ, so no remelting of δ was observed. However, as soon as the temperature was slightly decreased by dT, the remelting of δ was seen while the γ platelet remained without further growth (Figure 2.29 b, d, f). After the δ was remelted for a certain length of dL, the γ continued to grow into the gap where the δ was remelted.

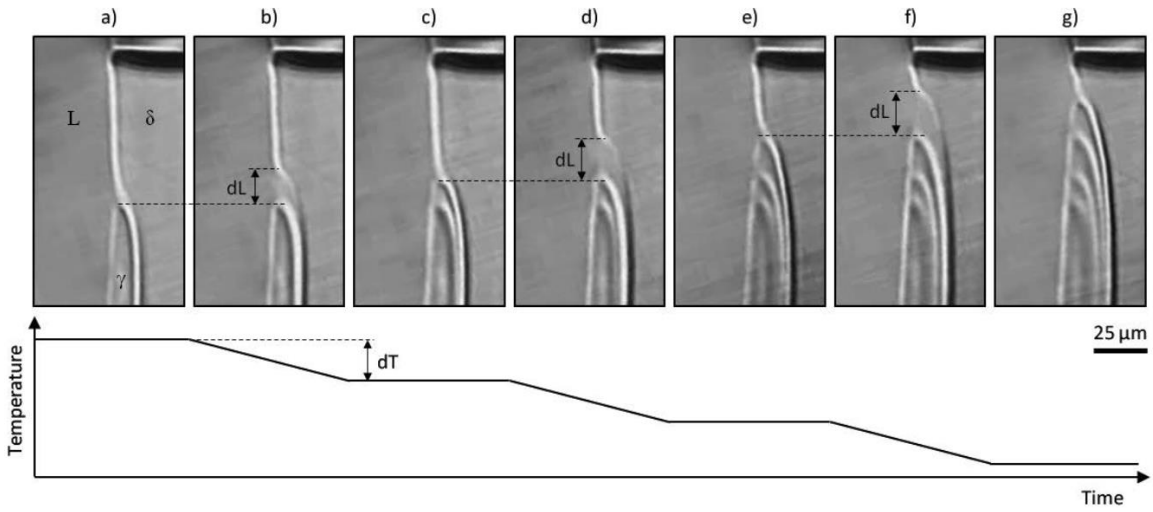

Figure 2.29 Sequence of events during incremental growth of γ in a Fe-0.42wt.%C alloy.

Griesser et al. offered a different explanation for remelting to that offered by Phelan et al. [21], suggesting that remelting of δ is not related to the heat transfer but is caused by the solute diffusion. The authors of [30] concluded that the diffusion of carbon in iron is higher compared to the diffusion of iron atoms, leading to a partitioning process and causing remelting of δ, which occurs at higher driving force (higher rate) than the solidification of the γ phase.

Both observations of peritectic steels described above were made using the concentric solidification technique, where the solidification commences at the outer rim of the steel disk and moves towards the centre. It was previously shown in Figure 2.21 that the middle of the cross-section of the concentrically solidified sample was highly segregated with the alloying elements (C, Mn and other) [64]. Due to the existence of a radial thermal gradient, when the temperature is the highest in the middle of the sample, the elements are forced to diffuse towards the liquid pool in the middle of the sample's disk.

Therefore it is essential to understand if remelting of peritectic steel indeed occurs when the peritectic reaction is not affected by high segregation of the elements, that is, remelting does not only occur in the concentric test but also in the droplet solidification test.

2.10 Volumetric changes in peritectic steels and shrinkage experiments

Volumetric change is an important factor, which must be taken into account to achieve good quality castings because large shrinkage can be a reason for defect formation during solidification of peritectic steels [19,57,75–78]. Therefore there is a need for a comprehensive

understanding of the phase transformations and the resultant shrinkage to avoid such defects [75].

It has been well documented from casting of peritectic steels that these steels are more prone to defects than other commercial grades. Emi and Fredriksson [13] have investigated the non-uniformity of the solidifying peritectic steel shell and found that non-uniform steel shell can occur as a result of shrinkage due to the $\delta \rightarrow \gamma$ transformation which leads to the hot spot in the peritectic steel shell during solidification. This may lead to irregular heat transfer to the continuous casting mould, causing the stresses and crack generation.

Suzuki et al. [79] have measured the heat flux and shrinkage during solidification of 9 kg of peritectic and non-peritectic steels. It was found that peritectic steels (which have carbon composition close to the steels used in the current research) exhibit an anomalous decrease of the heat flux on the mould surface, which is correlated with a high surface roughness of the solidifying shell. Moreover, the shrinkage of the solidifying shell of the peritectic steel increases just after the beginning of solidification and the shrinkage rate remains larger compared to all other steel samples investigated in the research [79].

Another example of the shrinkage measurements during solidification of steels was presented by Mehrara et al. [76]. The sample size for the experiments conducted by Mehrara et al. [76] was much smaller (about 250 grams) compared to that used by Suzuki et al. (9000 grams) [79]. This leads to faster solidification rates, so the shrinkage values measured by Mehrara et al. [76] are closer to those, obtained at the solidifying shell during the continuous casting process.

The experimental setup used by Mehrara et al. [76] for the shrinkage measurements of metals during and after solidification is based on the idea initially proposed by Novikov [48] and further developed by Eskin et al. [49]. The detailed description of the experimental setup for these experiments can be found in [76] and is illustrated in Figure 2.30. The setup consists of a cavity with T-shaped geometries inside the graphite mould with one moving and three fixed walls. During the test, the molten metal, poured into the cavity, start to solidify and shrink, pooling the moving wall towards the fixed wall located on the opposite side of the mould. The shrinkage, i.e. the displacement of the moving wall, is measured by a laser measurement device.

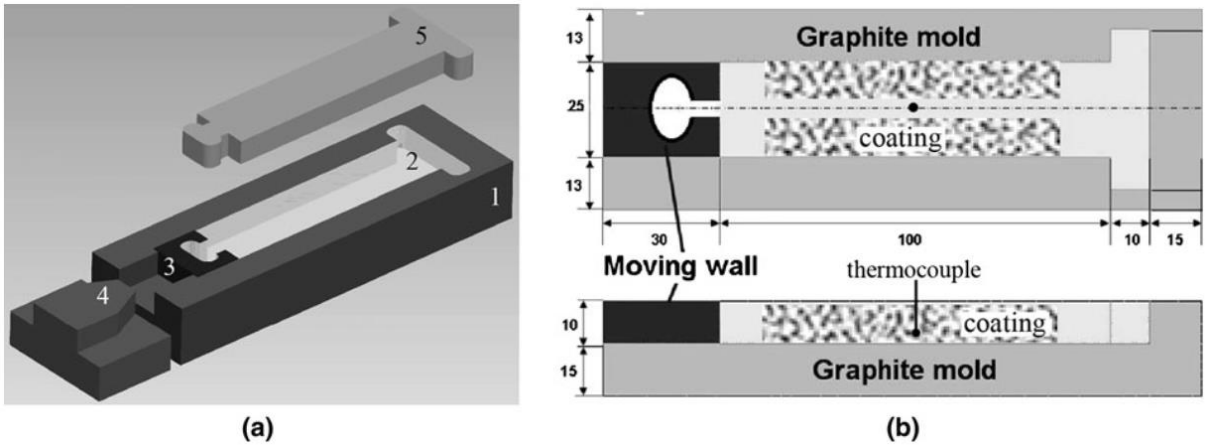

Figure 2.30 (a) Experimental setup of shrinkage experiments: mould (1), cavity (2), moving block (3), laser (4), and steel sample (5), and (b) schematic of the mould and coating. Dimensions are in mm [76]

The experimental results presented by Mehrara et al. [76] have shown that it is a good method for measuring the shrinkage during solidification of steels because it is comparable with the cooling conditions during the CC process. It was suggested to use this technique as a method for detection of the hot cracking susceptibility [76] because larger shrinkage during solidification increases the stresses at the solidified shell and therefore increases the chances of the hot crack formation.

Therefore, comparable experimental techniques will be used in the current research to measure the shrinkage formation in peritectic and non-peritectic steels during solidification. It may help to understand if there is an influence of the large shrinkage on the solidification behaviour of peritectic steels.

2.11 The application of Infrared Thermography for analysis of material behaviour

2.11.1 Overview of infrared thermography

The application of the infrared (IR) technique in Materials Science has been considerably extended over the last 25 years in academic laboratories and research centres. This is due to the progress which was achieved in the digitisation of the signal, the increase of the data transfer rate and image processing technique, which simplified the use of thermal imaging cameras [80].

The main advantage of infrared thermography is that it provides a contactless full-field measurement of the surface temperature. In addition, current IR cameras allow us to record the data at frame rates reaching up to several hundred Hertz [80]. Such a high framing rate is

especially important for studying the kinetic behaviour of materials. IR thermography can also help to better understand and model the behaviour of materials at high temperatures. The thermographic analysis can be done during physical treatment of the sample (hardening, annealing), welding processes (melting, solidification), thermomechanical processing (phase transformation, precipitation kinetics) [80] and solidification processing of the cast material [81].

2.11.2 Application of infrared thermography in the high-temperature environment

Previously, thermal imaging studies have been conducted to diagnose the welding processes [82], assess the solidification of Al-Si alloys [81] and monitor the thermal history during depositions of 304 Stainless Steel [83]. However, there was no information found in the literature about the application of IR thermography to assess the solidification behaviour of steels until this technique was developed in the current research to image a rapid solidification of the steel samples during shrinkage experiments [11]. More detailed explanation of this technique is summarised in Section 3.4, and the results are presented in Chapter 5.

Another application of IR thermography to assess the solidification behaviour of steels was also developed for the current study by Slater et al. [69] by combining the CSLM with a thermal imaging camera. It was found that by adding the infrared thermography during the solidification of the steel sample in the CSLM, information can be obtained about the latent heat of fusion during solidification and solid state transformation from δ to γ of both non-peritectic steel and pure iron. More detailed information about this technique is summarised in Section 3.5. The information about the radiated heat was collected from the sample and crucible during cooling, which gives useful information about the exothermic heat during solidification. It mimics the DSC technique, however, the maximum cooling rates of the currently available DSC is around 0.5°C/s, whereas the cooling rate with the newly developed technique can be achieved up to 10°C/s [69]. Therefore, the assessment of the released heat from the steel samples can be done at rapid cooling rates, which is important in order to interpret the solidification behaviour of industrial steels at cooling rates, applicable to the CC process.

Chapter 3 Research Methodology

3.1 The Samples under investigation

As case studies, a low carbon hypo-peritectic (Hypo-P) steel sample was chosen to compare with non-peritectic steels (Non-P 1 and Non-P 2), hyper-peritectic (Hyper-P) steels and pure iron (Fe). The samples were selected based on industrial importance and research interest. The samples called Hypo-P, Hyper-P, Non-P 1 and Non-P 2 were produced and supplied by Tata Steel, IJmuiden, The Netherlands. The pure iron sample was also supplied by Tata Steel, IJmuiden, The Netherlands. The chemical composition of the samples was determined using optical emission spectrometry (OES) (Table 3.1).

Table 3.1 Chemical composition of the samples investigated in the current research

Samples	Chemical composition (wt%)					
	C	Mn	Cr	Si	S	Fe
Iron	0.0005	0.0001	0.0003	0.0005	0.0005	99.9000
Hypo-P	0.1130	0.4940	0.0160	0.0045	0.0086	bal.
Hyper-P	0.1540	1.9400	0.0179	0.8410	0.0010	bal.
Non-P 1	0.0670	0.3230	0.0180	0.0001	0.0120	bal.
Non-P 2	0.042	0.234	0.0170	0.0022	0.0011	bal

3.2 Thermodynamic calculations of the solidification paths of the samples

In order to predict the equilibrium solidification paths of the steels under investigation, the Thermo-Calc – 2017a software package was used. Thermo-Calc [49] has a graphical and console mode. In the current study, the graphical mode was used, so there is no need to use the codes like in the console mode [44]. A project with different chemical compositions was generated for each steel under investigation. Then, several specific phases (Liquid, BCC, FCC) and precipitates (MnS) were selected to define a system based on the TCFe9 database within the temperature range between 500 and 1600°C and under a pressure of 1.01325 bar.

The calculated pseudo-binary Fe – C diagram is illustrated in Figure 3.1. for all samples investigated in the current research. The vertical dashed arrows in Figure 3.1. show the equilibrium solidification behaviour of pure iron, Non-P 2, Non-P 1, Hypo-P and Hyper-P samples, based on their chemical composition. The difference in the solidification behaviour of Hypo-P and Hyper-P samples is that the Hypo-P sample undergoes hypo-peritectic reaction during solidification, i.e. after the sample undergoes a peritectic reaction (L + δ + γ region), there are two solid phases of δ + γ before it transforms to a single solid γ phase. Whereas after the Hyper-P goes through the hyper-peritectic reaction during solidification, i.e. after the sample undergoes a peritectic reaction (L + δ + γ region), it transforms to a region of L + γ before it fully solidifies as γ. Neither Non-P 1 nor Non-P 2 samples undergo peritectic reaction, however, the solidification path of the Non-P 1 sample is close to the peritectic region, therefore, the solidification behaviour of that sample is different compared to the Non-P 2 sample. For comparison, the solidification behaviour of pure iron has also been considered in the current research.

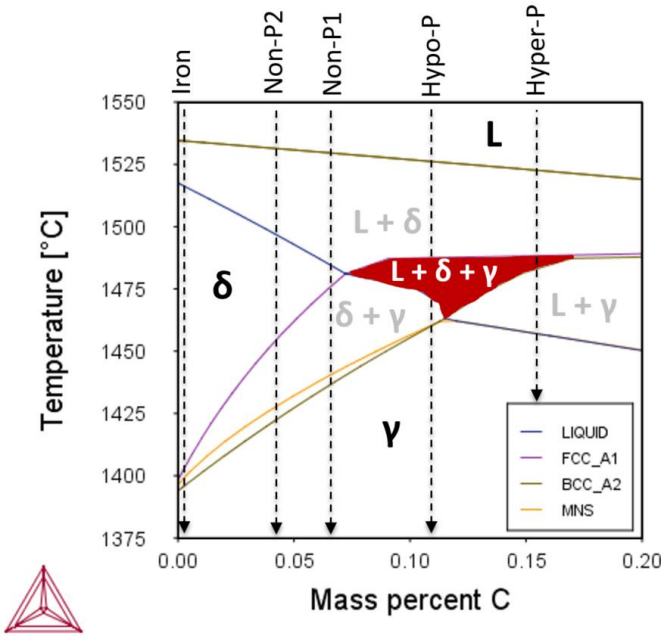

Figure 3.1 Thermo-Calc calculations of equilibrium Fe-C diagram for Hypo-P sample, compared to the solidification paths of all other samples investigated in the current research. Vertical dashed arrows indicate the carbon content of each sample.

3.3 The techniques used in DSC and CSLM experiments

3.3.1 Equilibrium solidification paths of the samples

The solidification sequences for the Hypo-P and Non-P 1 samples are illustrated in Figure 3.2. In comparing the two samples, the mushy zone[2] range of Hypo-P and Non-P 1 samples are shown to be almost the same – 45°C and 42°C respectively. However, the temperature range between the liquid and single γ phase is narrower in the Hypo-P sample – 62°C, increasing to 98°C in the Non-P 1 sample. Thus, based on the equilibrium calculations of the Hypo-P sample, the transformation from δ to γ occurs during a comparably earlier stage of solidification, and it starts when there is about 8% of liquid remaining during solidification. However, in the Non-P 1 sample, the δ to γ transformation happens once solidification of δ is completed.

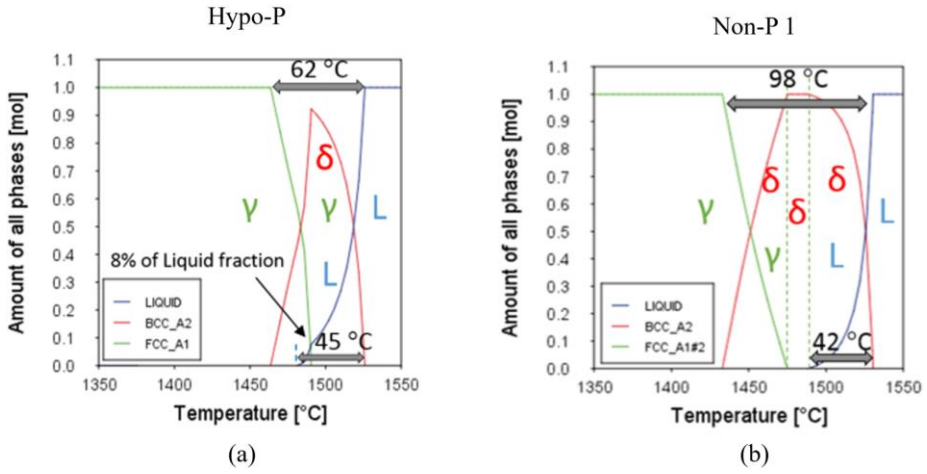

Figure 3.2 Thermo-Calc calculations of phase fractions during solidification of the Hypo-P (a) and Non-P 1 (b) samples

The enthalpy change for each phase as a function of temperature for the Hypo-P and Non-P 1 samples are calculated using Thermo-Calc [49], assuming zero-undercooling for all transformations (Figure 3.3). When the nucleation and growth of δ occurs, there is a significant exothermic heat associated with it (Figure 3.3). In the Non-P 1 samples, this was followed by a gradual enthalpy decrease as the temperature decreases while the steel was in the δ phase, then a slight reduction in enthalpy occurs when δ transforms to γ. However, in the Hypo-P sample, the nucleation of δ is followed by a peritectic reaction (nucleation of γ from a mixture of L+δ). This is associated with a sharp drop in enthalpy, resulting in 6% and 11% greater heat release

[2] Mushy zone is a temperature range between liquidus and solidus temperatures

computed for the Hypo-P sample, compared with that of the Non-P 1 and Fe samples respectively, until the system reaches the solidus temperature.

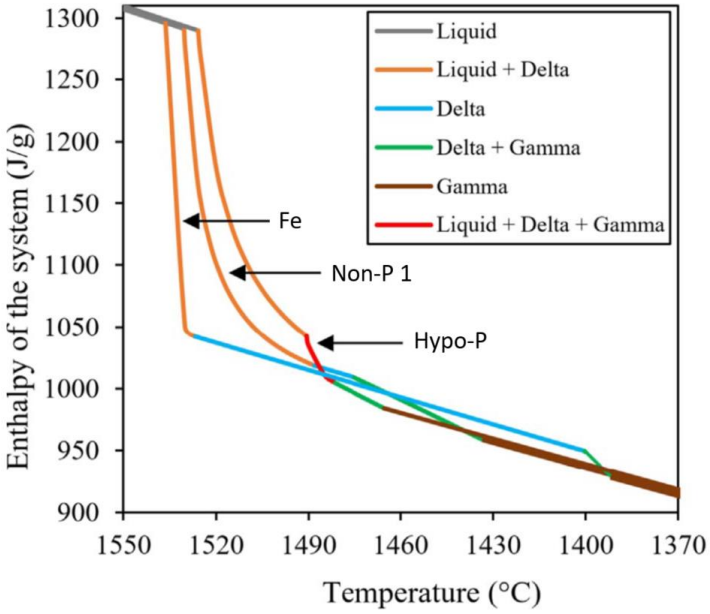

Figure 3.3 Enthalpy changes for each phase of the Hypo-P, Non-P 1 and iron samples as a function of temperature

3.3.2 The DSC: experimental setup

A NETZSCH STA 449 F3 *Jupiter* DSC was used for the calorimetry experiments in this research. The illustration of the DSC equipment is shown in Figure 2.12. The DSC was calibrated using the melting points of high-purity In, Sn, Al, Ag and Ni. High purity protective gas (argon, N6.0) was further purified using an oxygen getter, so during the DSC tests, the oxygen content at the inlet to the DSC was reduced to approximately 1ppb. The experiments were carried out using steel samples with an average weight of 130 mg (± 3 mg) in sapphire crucibles (6.8 mm diameter, 4 mm height, 85 µl volume) with a sapphire lid (6.8 mm diameter) at heating and cooling rates of 0.5 °C/s in the critical temperature ranges of 1300°C - 1585°C.

Before the start of each experiment, the furnace was evacuated and backfilled with argon three times; it was also dried at around 250°C for one hour to remove moisture, then once more evacuated and purged with argon at around 100°C - 150°C. Furthermore, sacrificial Ti slugs and Zr rings were used during the experiments to ensure a low oxygen partial pressure throughout the experiments.

The general shape of the DSC curve during phase transformations and melting of low carbon steel is shown in Figure 3.4 (a). During heating, the phase transformation and melting require

heat input, so the upward peak is endothermic, as illustrated in Figure 3.4 (a). During cooling, solidification of the sample leads to the release of heat, so the downward peak is exothermic, as shown in Figure 3.4 (b).

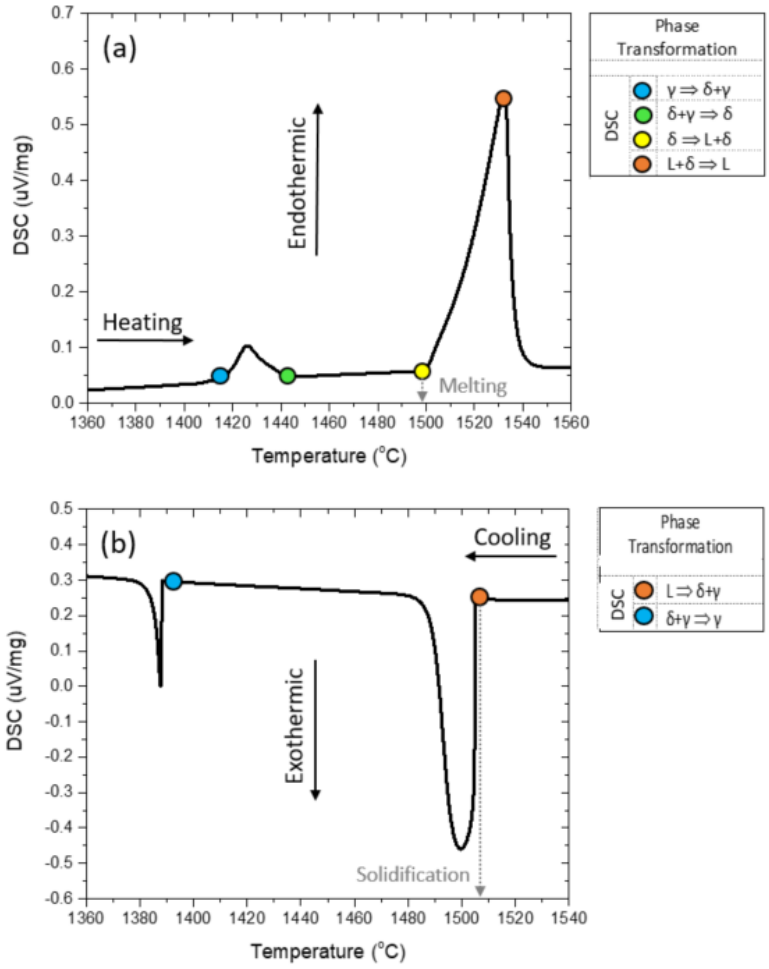

Figure 3.4 General DSC curve of phase transformation and melting of the low carbon steel (about 0.06%C) upon heating (a), followed by a DSC curve of solidification and phase transformation of low carbon steel upon cooling (b)

The maximum heating and cooling rate of the DSC equipment (which is available in the current research) is 0.83 °C/s. Initially, the DSC tests were conducted at 0.08, 0.33, 0.5 and 0.83 °C/s to find the optimal heating and cooling rate for the DSC experiments. It was found that the rate of 0.83°C/s is too high because there is not enough time to collect the data points as soon as the sample starts to cool down and solidify. Therefore, the first peak during cooling (solidification peak) is not fully recorded by the software.

At 0.08°C/s it was difficult to detect the onset temperature of the solid-state phase transformation (caused by the endothermic $\gamma \rightarrow \delta$ transformation during heating). This is because the heat was consumed slowly by the sample during $\gamma \rightarrow \delta$ transformations at a heating

rate of 0.08 °C/s and the DSC equipment is not sensitive enough to pick up this small thermal difference as soon as the transformation commences. The DSC results at 0.33 °C/s for the peritectic steels, which have comparable composition used in the current research, were already published in the literature [19,57]. Therefore, due to the limitations of the equipment and other reasons described above, the optimal heating and cooling rate of 0.5 °C/s was chosen for the current research.

The difference in the cooling rate across the solidified metal during continuous casting process varies from 10^2 °C/s (at the steel shell closer to the copper mould) to 10^{-2} ºC/s (closer to the middle of the solidified metal) [27,28] as described in section 2.2. Therefore, the chosen cooling rate of 0.5 °C/s corresponds to the cooling rate closed to the middle part of the metal during the continuous casting process and not at the steel shell.

3.3.3 The CSLM: experimental setup

In the current study, a Yonekura VL2000DX – SVF17SP CSLM was employed to record the high-quality microscopy images during the experiment under an inert gas atmosphere (argon, 6N). The temperature of the investigated samples was controlled by an R type thermocouple, which was positioned at the outer bottom of the crucible in the Pt-sample holder. The CSLM was calibrated using the melting points of pure Cu and Ag. The experiments were carried out through surface visualisation of the sample upon melting and solidification and recorded at 15 frames per second during controlled heating and cooling rates of 0.5 °C/s.

During the CSLM experiments, a 1.5 mW He-Ne (wavelength 632.8 nm) laser was used, which helped to distinguish clearly the different phases at the sample surface, which have various reflectivity and heights that are caused by the volume change during transformations. Various applications and observations using high-temperature CSLM have been described elsewhere [19,63,64,67,84–88] and summarised in Section 2.7.

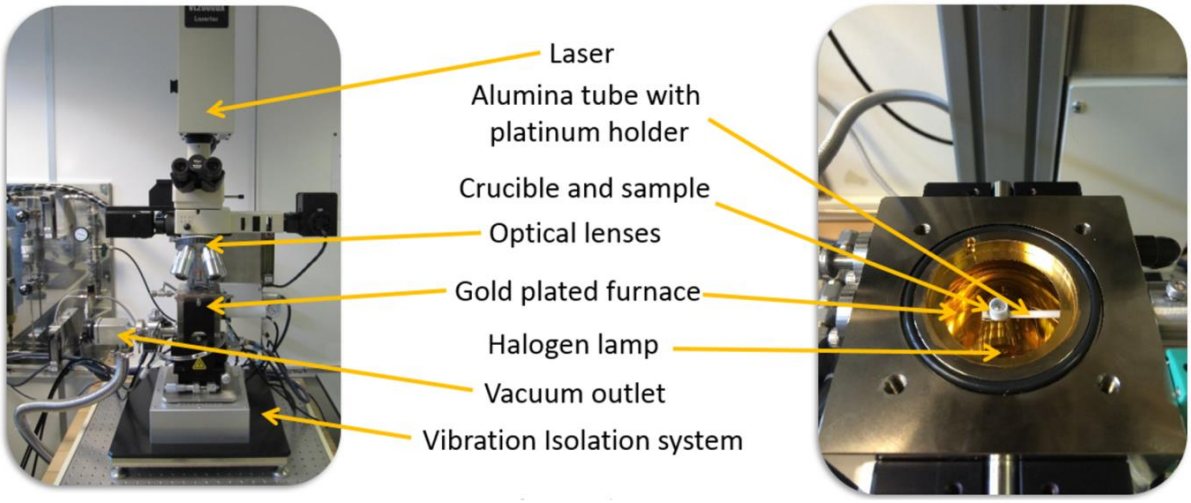

Figure 3.5 Illustration of the experimental setup for CSLM experiments

The CSLM experiments were carried out using steel samples with an average weight of 130 mg (±3 mg) in alumina crucibles (6.8 mm diameter, 4 mm height).

As previously mentioned in Section 2.7, the droplet solidification technique will be used in the current research instead of the widely used concentric solidification technique in order to avoid the macrosegregation (difference in chemical composition at the macroscopic level, i.e. 10^{0} to 10^{-3} m [28]) observed during concentric tests as shown in Figure 2.21 and Figure 2.22. To confirm that there is no macrosegregation during the droplet solidification technique, SEM analysis was carried out on the solidified Hyper-P sample, where segregation of Mn is easier to detect compared to all the other samples considered in this research. For these analyses, the steel sample, which solidified during the CSLM test, was held using an Al-alloy wire and embedded into Bakelite. The sample was then ground to reach the middle part of the sample in the cross section and then it was mirror-polished for the SEM analysis, as illustrated in Figure 3.6.

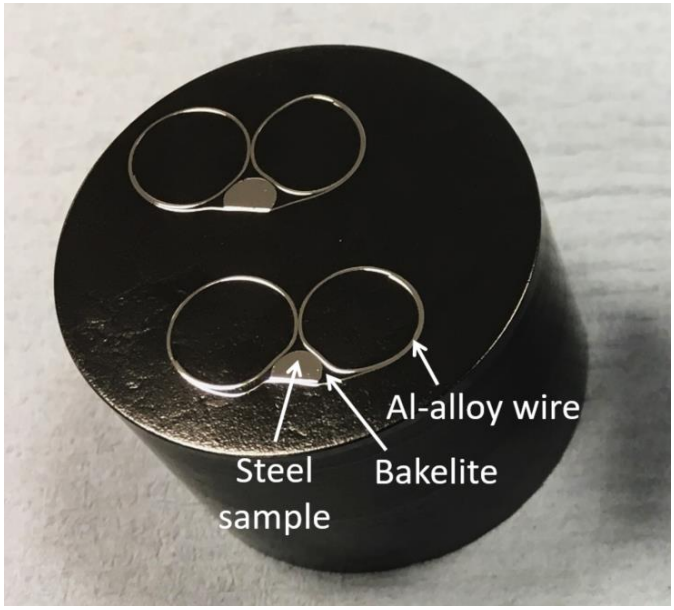

Figure 3.6 CSLM sample, held using Al-alloy wire and embedded into Bakelite for the SEM analysis

Figure 3.7 illustrates microsegregation (difference in chemical composition at the interdendritic region or microscopic level, i.e. 10^{-6} to 10^{-5} m [28]) of Mn in the cross-section of the Hyper-P sample, which is expected, but it does not show macrosegregation. It suggests that due to the absence of macrosegregation, the events, which occur on the surface of the sample during the CSLM test, also represent the solidification behaviour of the bulk of the sample.

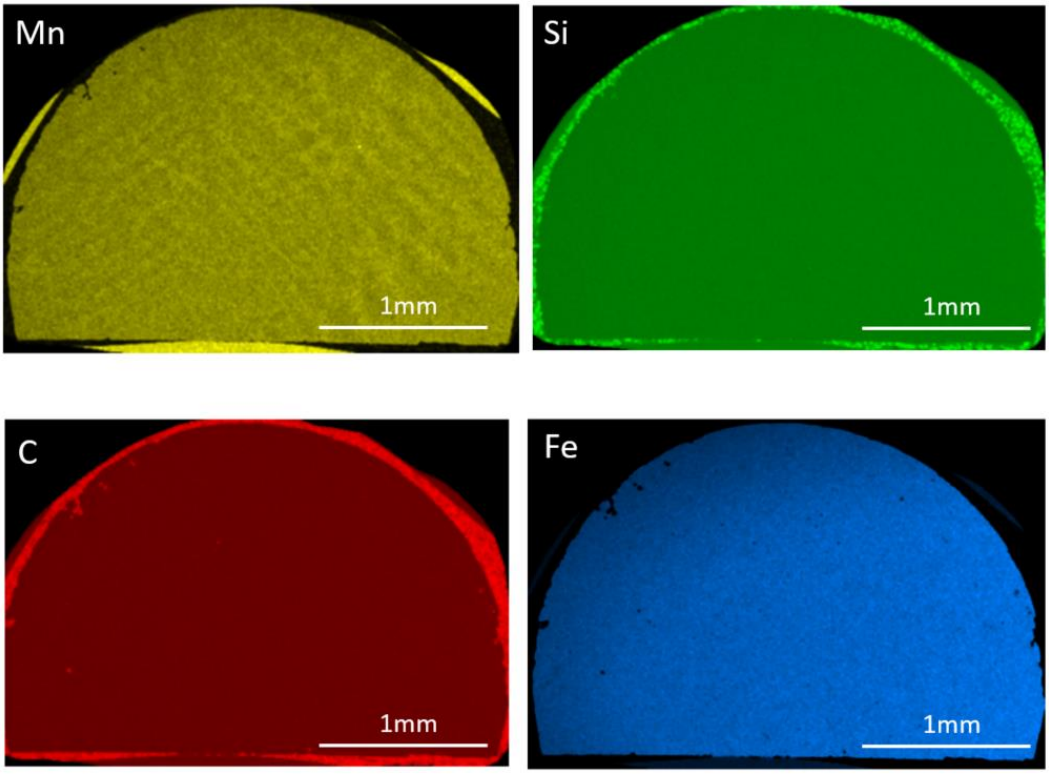

Figure 3.7 SEM analysis of the cross-section of the Hyper-P sample, solidified during the droplet solidification technique during CSLM tests

During the SEM analysis, the area for the mapping was selected manually around the cross-section of the sample. The area which was not selected for the analysis around the steel sample is shown in black colour in Figure 3.7. C and Si mapping results show the area with high C and Si content around the sample but it is the results for the Bakelite, and not the steel sample. SEM results for the Mn and Fe also show a high concentration of the elements around the sample, but these are the results for the Al-alloy wire (as shown in Figure 3.6), and not for the CLSM steel sample.

3.4 Solidification Shrinkage Experiments Combined with Infrared Thermography

3.4.1 Equilibrium solidification paths of the samples

The solidification sequences for the Hypo-P and Non-P 2 samples are illustrated in Figure 3.8. In comparing the two samples, the mushy zone length of the Hypo-P is larger (45°C) compared to the Non-P 2 sample (30°C). The temperature range between the liquid and single γ phase is much narrower in the Hypo-P sample – 62°C, compared to 117°C in the Non-P 2 sample. Therefore, in the Non-P 2 sample, the δ to γ transformation happens as a solid state

transformation, whereas in the Hypo-P sample it occurs when there is about 8% of liquid fraction (or 92% of solidified δ).

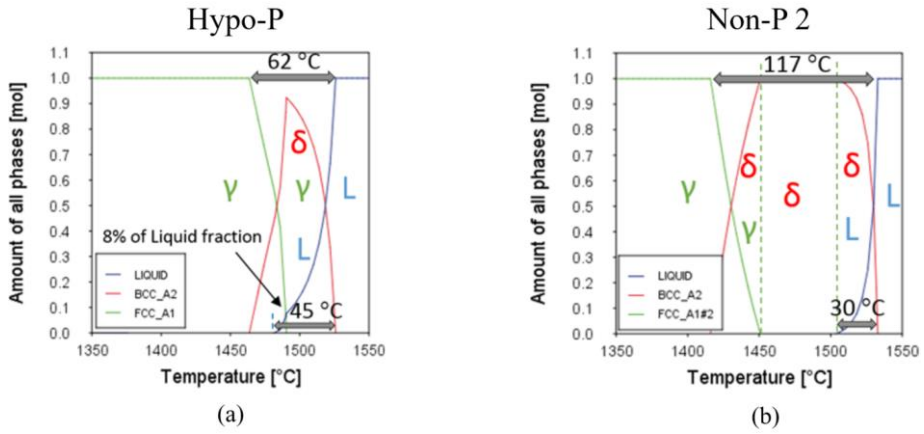

Figure 3.8 Thermo-Calc calculations of phase fractions during solidification of the Hypo-P (a) and Non-P 2 (b) samples

Figure 3.9 illustrates the volume change of the system predicted with the Thermo-Calc software [49] for the investigated steels and pure iron (as a reference). As shown in the graph, the nucleation and growth of δ are associated with a large shrinkage in both samples. Then, in the Non-P 2 sample, this was followed by a gradual decrease in volume after the steel solidifies. Whereas in the Hypo-P sample, the growth of δ is followed by a rapid shrinkage as soon as the sample reaches the peritectic reaction (red line in Figure 3.9). As soon as the Non-P 2 and Hypo-P samples reach single γ phase, the shrinkage value equalises in both samples and reaches 3% right before γ transforms to α (Figure 3.9 (b)).

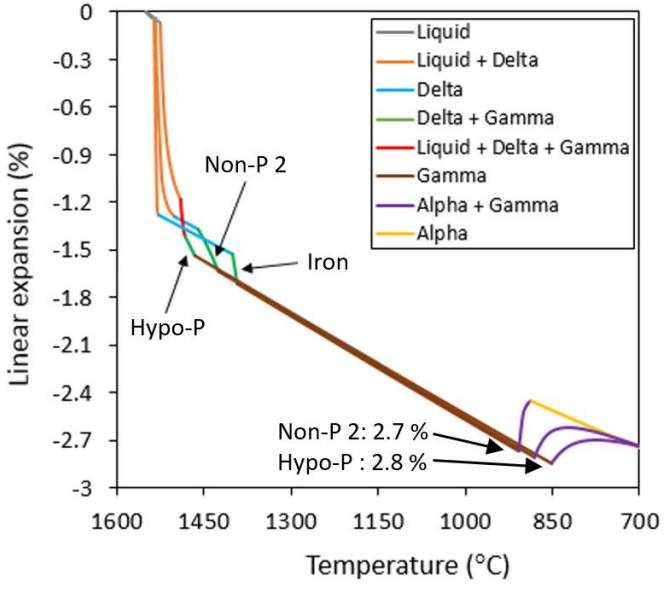

Figure 3.9 Volume changes for each phase of the Hypo-P and Non-P 2 samples as a function of temperature

As δ (BCC) and γ (FCC) have different densities, δ to γ transformation is associated with steel shrinkage (in the direction of the cast thickness). If during CC processing this transformation occurs as a massive type in the Hypo-P steels, the rapid volume change associated with it may lead to sudden bending of the thin steel shell and an increased strain rate, which worsens due to the ferrostatic pressure [14,89].

3.4.2 The experimental setup for measuring solidification shrinkage of the samples

Solidification shrinkage is the volume shrinkage of metals, which occurs while 100 pct of liquid transforms to 100 pct of solid phase [49]. As outlined in the literature review (Section 2.10), peritectic steels are prone to higher shrinkage during solidification, compared to non-peritectic steels. During the continuous casting process, it is almost impossible to obtain shrinkage measurements at the initial solidification stage when the CC is operated at a temperature above the steel melting point [90]. Thus, alternative experiments should be conducted to obtain these details.

The detailed description of the experimental setup for the shrinkage experiments can be found in Mehrara et al.'s work [76] and is illustrated in Figure 2.30 (Section 2.10). The displacement of the moving wall is measured by a Micro-Epsilon optoNCDT 1700-20BL Laser, which has a resolution of 1.5 μm.

The surface of the moulds was spray coated with a thin layer of Yttria Stabilized Zirconia and boron nitride to avoid carbon diffusion from the graphite mould and decrease the friction forces upon shrinkage of the solidified material (Figure 3.10).

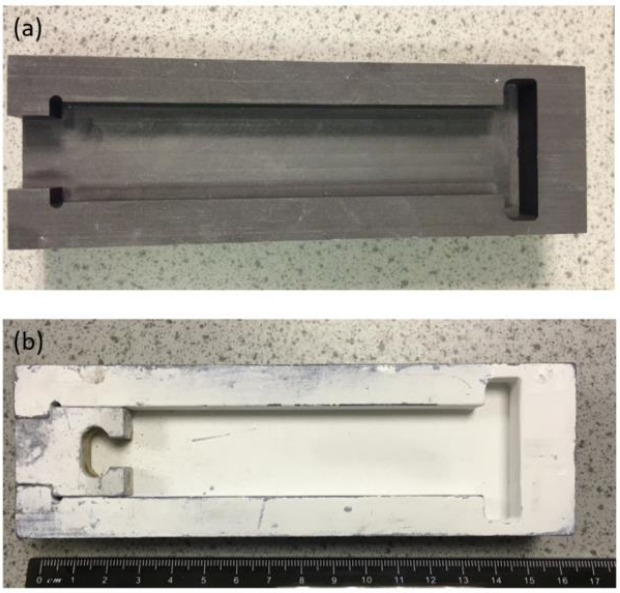

Figure 3.10 Graphite mould for shrinkage experiments (a) without the coating and moving wall; (b) with coating and moving wall

To reach a high cooling rate, comparable to the continuous casting conditions (average of about 10°C/s [28]), a water-cooled copper mould was developed for the current research, as shown in Figure 3.11. The advantage of this method is the possibility of measuring the shrinkage of the metals from liquid to solid state at high cooling rates up to about 50°C/s at the beginning of solidification, which cannot be done using other methods, such as dilatometry or DSC.

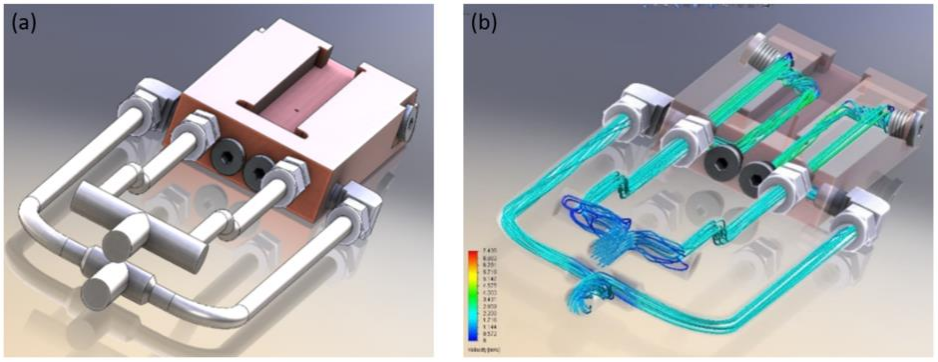

Figure 3.11 Illustration of (a) water-cooled copper mould and (b) water-flow inside the mould, designed for the solidification shrinkage experiments

In the current study, the steel samples were remelted in the TopCast Induction Furnace [91] under a protective argon atmosphere (using Ar supply during the test) and then cast into the mould. Figure 3.12 illustrates the typical shrinkage results, recorded during the test. It can be seen that the pre-shrinkage expansion is formed after the casting of the molten metal into the mould and before the solidification shrinkage (Figure 3.12). This expansion is associated with the formation of CO and CO_2 when the carbon in the molten metal reacts with the oxygen in

the atmosphere and the values of the expansion should be considered for measuring the shrinkage of the steels [76,92]. The solidification shrinkage values will then be compared between Non-P 2 and Hypo-P samples to assess the difference between the solidification shrinkage of the industrial steels.

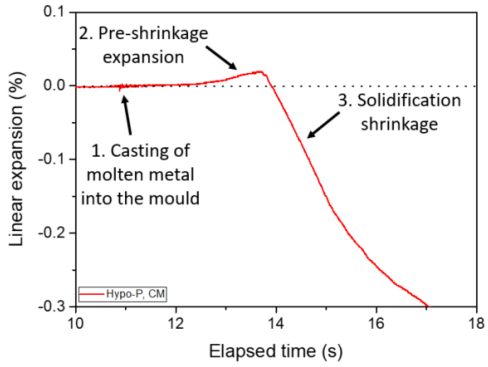

Figure 3.12 An example of the experimentally measured pre-shrinkage expansion and solidification shrinkage of the Hypo-P steel, solidified in the water-cooled copper mould

One of the main limitations of this technique is that the experiment is conducted in the open atmosphere, so the formation of the CO and CO_2 gases can affect the solidification shrinkage. This will further be described in Chapter 5.

3.4.3 The application of infrared thermography during shrinkage experiments

The apparent temperature of the solidifying metal is obtained using infrared thermography. The infrared imaging system is a powerful experimental device which allows us to obtain a mapping of the surface temperature of the whole area of interest without interfering with the investigated object [93].

In the current research, a Micro-Epsilon TIM160 thermal imaging camera was used, which operates at a frequency of 7.6–13 μm (long wavelength) and has a fast thermal imager with a frame rate up to 120 Hz with a resolution of 160 × 120 pixels using a 6° lens. This TIC is referred to as a long-wavelength camera with high resolution and sensitivity because atmospheric absorption is minimal. This IR camera is capable of measuring a temperature range of -20 °C – 1500 °C. During the measurements, the TIC was connected to a computer via USB 2.0, and the TIMConnect software allows control of the camera, so the thermal images and the temperature data can be observed and recorded during the test [94].

During the shrinkage experiments, the TIC was clamped about 500 mm above the mould where the molten steel is poured during the test. The camera is then manually focused on the area where the molten steel will be casted. During the test, the TIC receives the IR signal from the

steel samples, which corresponds to specific energy values. The signal is then converted to temperature data based on the given emissivity values, which allows us to analyse the solidification behaviour of the sample based on the thermal gradient across the sample.

3.5 CSLM Technique Combined with Infrared Thermography

3.5.1 Equilibrium solidification paths of the samples

Three steel samples were used for the assessment of the solidification behaviour during the combined CSLM and infrared thermography technique. The equilibrium solidification behaviour of two samples (Hypo-P and Non-P 2) are illustrated in Figure 3.8. The solidification behaviour of the third sample is shown in Figure 3.13. Comparing the solidification paths of the three samples, it can be seen that the equilibrium mushy zone is largest in the Hyper-P sample (53°C), compared to the Hypo-P (45°C) and Non-P 2 (30°C) samples. The peritectic transformation in the Hyper-P sample occurs when about 50% of liquid phase transformed to δ (Figure 3.13), whereas in the Hypo-P sample it occurs when about 92% of δ is solidified (Figure 3.8).

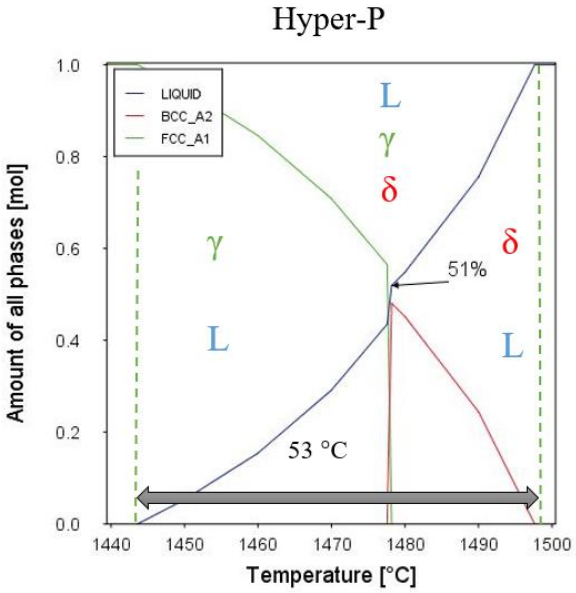

Figure 3.13 Thermo-Calc calculations of phase fractions during solidification of the Hyper-P sample

The differences found in the equilibrium calculations of the Non-P 2, Hypo-P and Hyper-P samples affects the solidification behaviour of these steel samples and the results are discussed in Chapter 6.

3.5.2 Combining the CSLM and IR thermography: experimental setup

As mentioned in the Literature review (Chapter 2) and Section 3.4.3, the Thermal Imaging Camera (TIC) allows non-contact measurement of the temperature distribution of the material, based on the infrared radiation emitted by the material. This helps to monitor and evaluate the high-temperature processes in different applications.

In the current research, a new method was developed [69] to evaluate the solidification behaviour of the steel samples during solidification by combining the CSLM and infrared thermography. The detailed information of the CSLM technique is given in Section 3.3.3, and the description of the thermal imaging camera is given in Section 3.4.3. The experimental setup of combined CSLM and IR thermography is illustrated in Figure 3.15. Before the test, the TIC was clamped 45 mm above the viewing window and manually focused on the surface of the sample, positioned inside the CSLM furnace. Alumina crucibles, which have round shape inside at the bottom (6.8mm diameter; 4 mm height) were chosen for these experiments to ensure that the sample always stays in the middle of the crucible and does not solidify on the crucible wall, as shown in Figure 3.14.

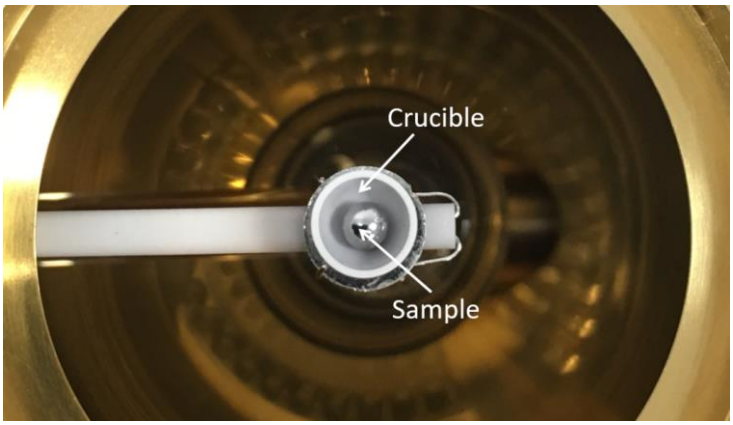

Figure 3.14 CSLM sample, solidified in the middle of the crucible, which has round shape inside at the bottom

The viewing window of the CSLM (shown in Figure 3.15 (2)) is conventionally made from quartz due to its high transmissivity and thermal stability around the frequency of laser operation. However, the transmissivity of quartz drops considerably after 4 µm. Therefore, in this experimental setup a CaF_2 window was used which maintains >70% transmissivity up to 14 µm, allowing us to use the TIC at a frequency of 7.6-13 µm, with a thermal sensitivity of 0.04K [69].

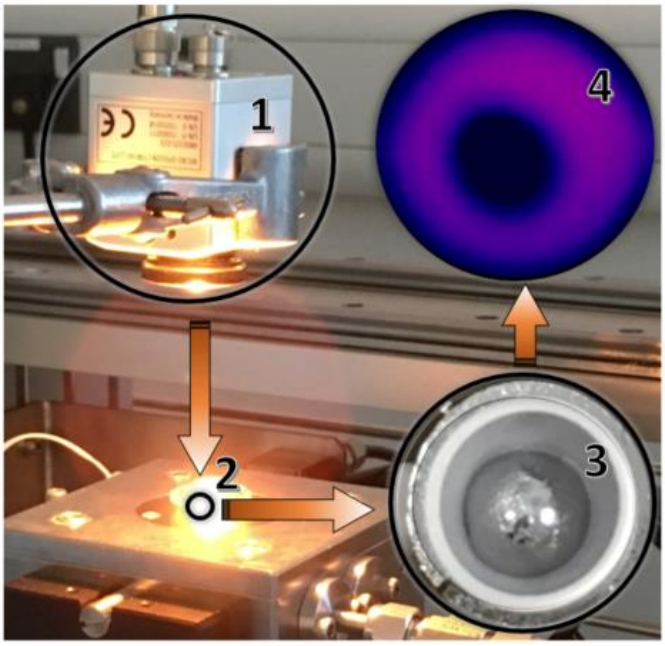

Figure 3.15 Experimental setup using a combination of CSLM with IR thermography. 1 - IR Camera; 2 - Observation area; 3 – Image, observed without IR camera at room temperature; 4 – Image, observed using an IR camera at high temperature.

To measure the emitted heat from the crucible (Figure 3.16 (b)), the thermal imaging source must operate at frequencies higher than the frequency of the halogen bulb at the bottom of the CSLM furnace (higher than 2 μm). Therefore, the long wavelength TIC, described in detail in Section 3.4.3, is also applicable to this technique.

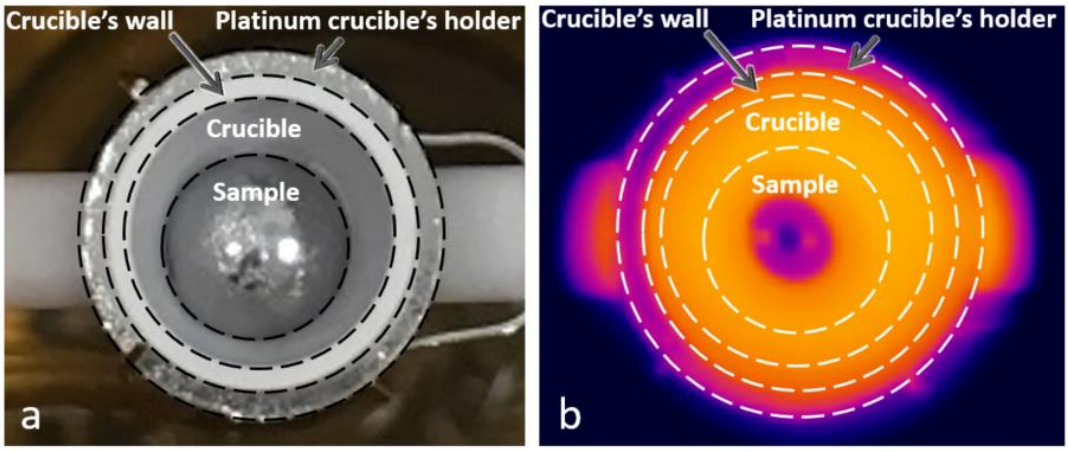

Figure 3.16 Illustration of the steel sample, solidified inside an alumina crucible, positioned on the platinum crucible holder, observed (a) visually at room temperature; (b) using IR thermography at high temperature

A series of experiments were conducted for the Non-P 2, Hypo-P and Hyper-P samples, which qualitatively indicates the heat conducted from the sample to the crucible during solidification. The data is taken from 8 pixels located on the crucible (C1-8), which are about 0.5mm away from the sample, as illustrated in Figure 3.17.

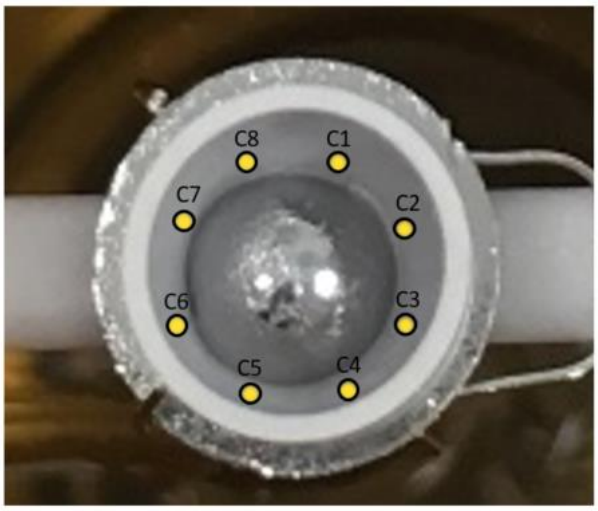

Figure 3.17 Eight point positions around the solidified sample, taken for the IR thermography analysis

The radiated heat was measured from the crucible and not from the sample because the emissivity of the solidifying sample changes when the liquid phase transforms into solid. In addition, it changes if there are any inclusions or oxides on the sample surface, which are also affected by the atmosphere [69]. However, the crucible always remains solid during the CSLM test, so it does not undergo the emissivity change due to phase transformation, but it shows the difference in emitted heat as the temperature changes. Therefore in order to obtain a much more reliable and consistent thermal reading, only the heat conducted from the sample to the crucible (much like a DSC) is considered, and not the heat, emitted by the sample.

The following equation was used to calculate the radiated heat during this technique [69]:

$$Q = A\varepsilon\sigma T^4 \tag{3.1}$$

where Q is the radiated heat, A is the surface area, ε is the emissivity of the sample, σ is the Stefan-Boltzmann constant and T is the absolute temperature. A value for ε of 0.7 is used in this study, which is consistent with the emissivity of alumina. A value for A (spot size) used in this study is 0.059 mm^2.

Chapter 4 Interpreting the Solidification Behaviour of Peritectic Steels by Combining CSLM and DSC

4.1 Introduction

In section 2.6 it has been shown that the only currently available study of the DSC cooling curves of low carbon peritectic steels [57] is questionable. The authors primarily observed three adjacent DSC peaks upon melting and only two distinct DSC peaks upon solidification. Having considered that the peritectic transformation involves several phases and it is generally problematic when trying to distinguish simultaneous multi-phase transformations, then additional information is required to interpret the DSC curves. Presoly et al. [19] have previously recommended combining both DSC and CSLM techniques for validating and determining peritectic transformations during heating. However, in the case of cooling, the usefulness of this technique was questioned, as they reported significant supercooling and "poor reproducibility" of results. Thus, a thorough explanation of the solidification phenomena of peritectic steels is still required.

This Chapter presents the DSC heating and cooling curves for the Hypo-P and Non-P 1 steels together with their surface visualisation using CSLM under experimentally comparable conditions. The explanation of the DSC and CSLM results of the steel samples is supported by the thermodynamic calculations and compared with the DSC cooling curves of pure iron.

Previous experimental studies of the DSC and CSLM techniques and the overview of the unresolved issues are summarised in sections 3.1 – 3.3. The chemical compositions and phase transformations of the samples are shown in sections 4.2 and 4.3 respectively. The detailed description of the DSC and CSLM techniques used in the current research can be found in Chapter 3.

4.2 Phase transformations of steels based on the DSC and Thermo-Calc results during heating

4.2.1 Non-P 1 sample

During DSC heating test at 0.5 °C/s, the Non-P 1 sample shows a small peak, which indicates the γ to δ transformation, and then a large peak, which indicates melting (Figure 4.1). The onset temperature of the solid-state phase transformation during the DSC test correlates well with the corresponding temperatures obtained with the Thermo-Calc software shown as triangles (Figure 4.1). However, a consistently higher transformation temperature can be seen on the DSC (around 10 ºC) which is a typical characteristic of DSC heating tests [57,87].

The main reason for the higher temperature found for the DSC results is because the thermocouple underneath the crucible with the sample is heating up faster than the sample itself. The larger the sample size, the more time it takes to heat it up, therefore, by the time when the sample reaches the transformation temperature, the thermocouple already has a slightly higher temperature.

A similar principle of the temperature detection is applied to the CSLM technique because during CSLM test the thermocouple is also located underneath the crucible and it is also heated up faster than the sample. This is a reason why in the following sections it is shown that the DSC results are closer to the CSLM temperature results, and not to the Thermo-Calc data.

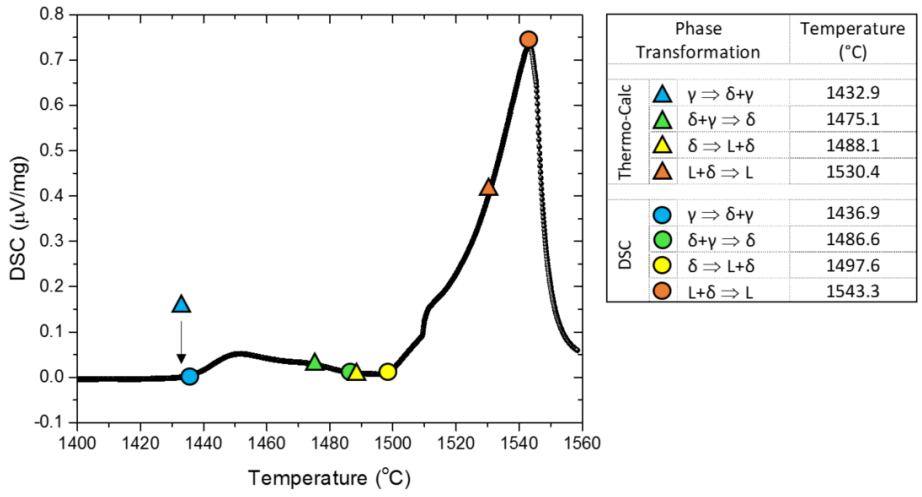

Figure 4.1 Thermo-Calc and DSC results of the Non-P 1 sample during heating

The peak temperature for the DSC curve during melting, which is indicated as "L + δ → L" in Figure 4.1 shows when the sample is completely molten, but it does not mean that this is a

liquidus temperature of the sample. The larger the size of the sample, the more time it takes to melt the sample completely, therefore this value should not be used as a liquidus temperature.

4.2.2 Hypo-P sample

During the DSC test, at a heating rate of 0.5 °C/s (Figure 4.2), the Hypo-P sample shows a small diffuse peak, when the γ to δ transformation commences. Then, there is a distinct second peak, which indicates the peritectic transformation, and a final large peak at higher temperatures, which is indicative of melting. The phase transformations and the corresponding temperatures are in good correlation with the Thermo-Calc results (Figure 4.2). This heating trend of the DSC curves is in general agreement with Presoly et al. [87] and Wielgosz et al. [57].

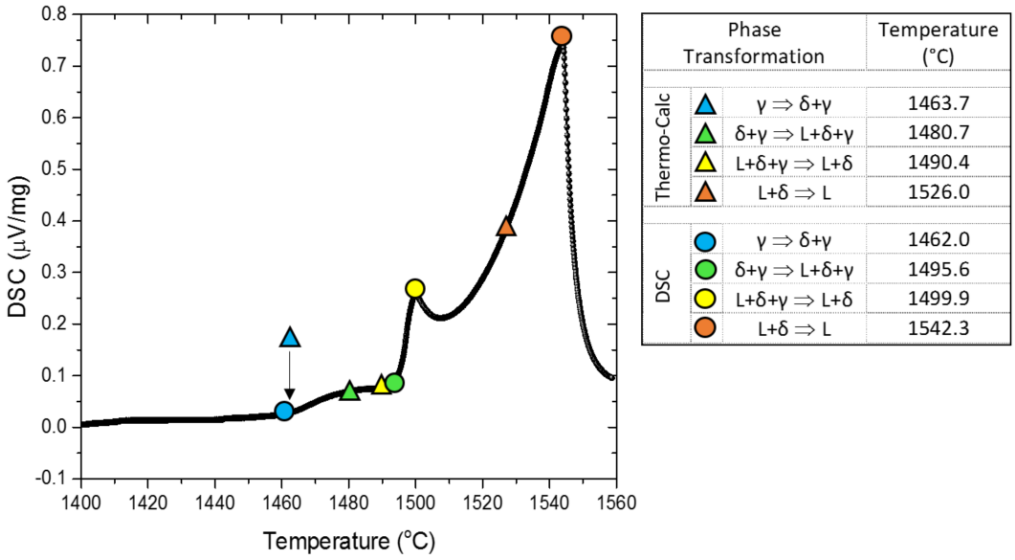

Figure 4.2 Thermo-Calc and DSC results of the Hypo-P sample during heating

4.3 Comparison between DSC, Thermodynamic Calculations and CSLM Experiments

4.3.1 Non-P 1 sample

A reasonably good agreement was observed between calculated transformation temperatures, using Thermo-Calc, and measured temperatures, using DSC and CSLM for the Non-P 1 sample during a heating rate of 0.5 °C/s (Figure 4.3).

The CSLM images (Figure 4.3a-d) show the events, which occur on the surface of the Non-P 1 sample (and are labelled on the DSC curve). Figure 4.3a shows γ at 1431 ºC immediately before the γ → δ transformation, where weak γ grain boundaries can be seen. The transformation from

γ to δ starts at 1431 ºC, which is close to the equilibrium transformation temperature and finishes at 1459 ºC.

It should be noted that DSC results indicate the enthalpy changes of the bulk, whereas CSLM images show the small area on the steel surface. This variance, therefore, means that the CSLM is likely to indicate a transformation which happens over a shorter period, as seen with the γ → δ transformation in Figure 4.3. Phelan [37] has previously reported that care needs to be taken during CSLM analysis of the grain growth rates and anomalous massive phase transformations, as they may not always represent the same velocity within the bulk. Nevertheless, the author [37] shows a good correlation between the fact of the δ → γ transformation on the surface during CSLM tests and the same transformation inside the bulk.

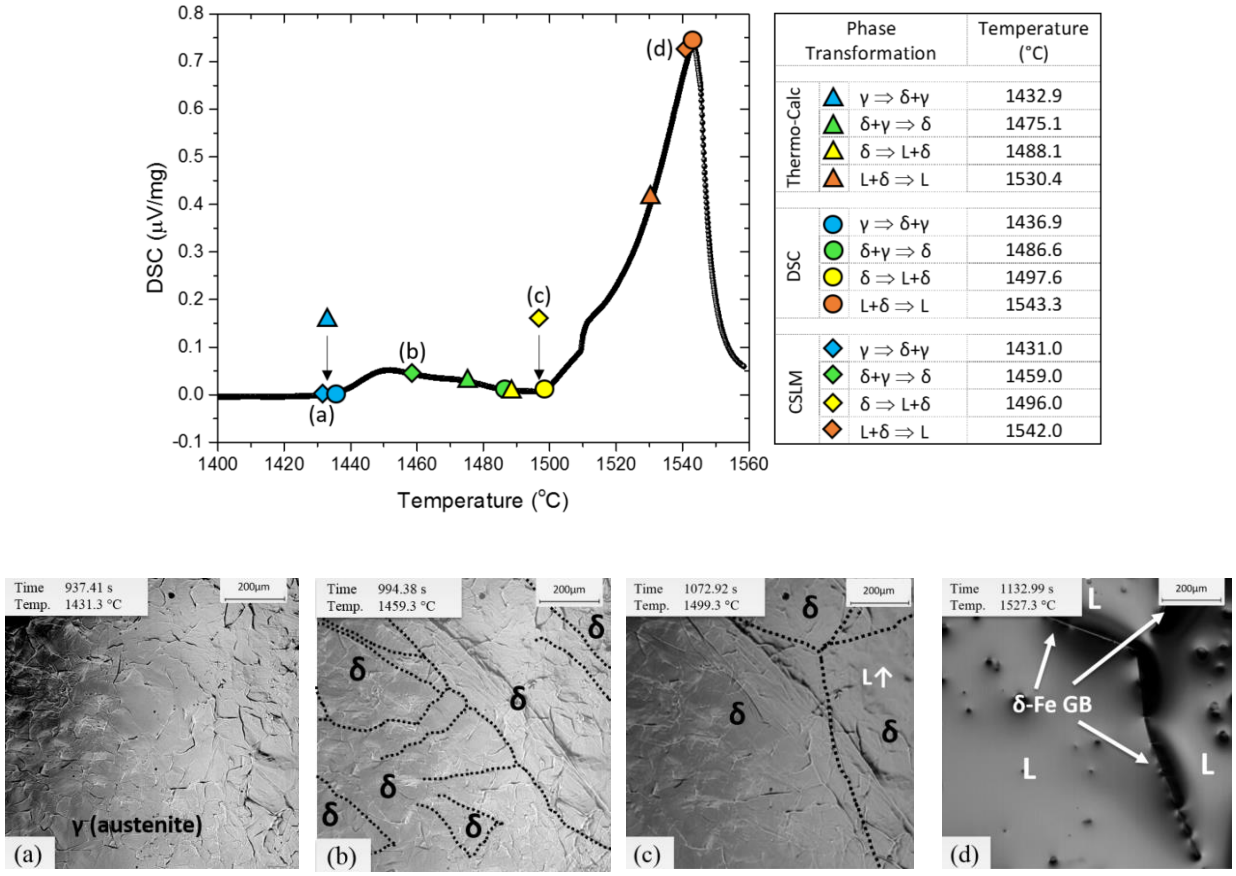

Figure 4.3 Combination of the DSC and CSLM results of the Non-P 1 sample at a heating rate of 0.5 °C/s

After γ transforms to δ, grain growth of δ is observed on the surface of the Non-P 1 sample (Figure 4.3b and c). As expected, during δ grain growth, the DSC curve does not exhibit a thermal response because it does not require as much endothermic energy as it is for the phase transformation. As illustrated in Figure 4.3c-d, during further heating, the liquid phase covers

the steel surface, but the δ grain boundary can still be seen (Figure 4.3d) until the sample is entirely molten.

4.3.2 Hypo-P sample

Figure 5.4 shows the CSLM results of the Hypo-P sample heated at 0.5 °C/s, where γ grain boundaries were seen at 1466 ºC (Figure 4.4a). Momentarily after that, γ to δ transformation commences at 1467ºC, followed by a continued increase in δ while γ decreases. Before this transformation was completed, the observations show the melting of γ at 1493ºC, which is an indication of a peritectic reaction (Figure 4.4b and c). Then, the liquid phase covered the steel surface, although, δ grain boundaries could still be seen in Figure 4.4d until the sample melted completely at 1536ºC.

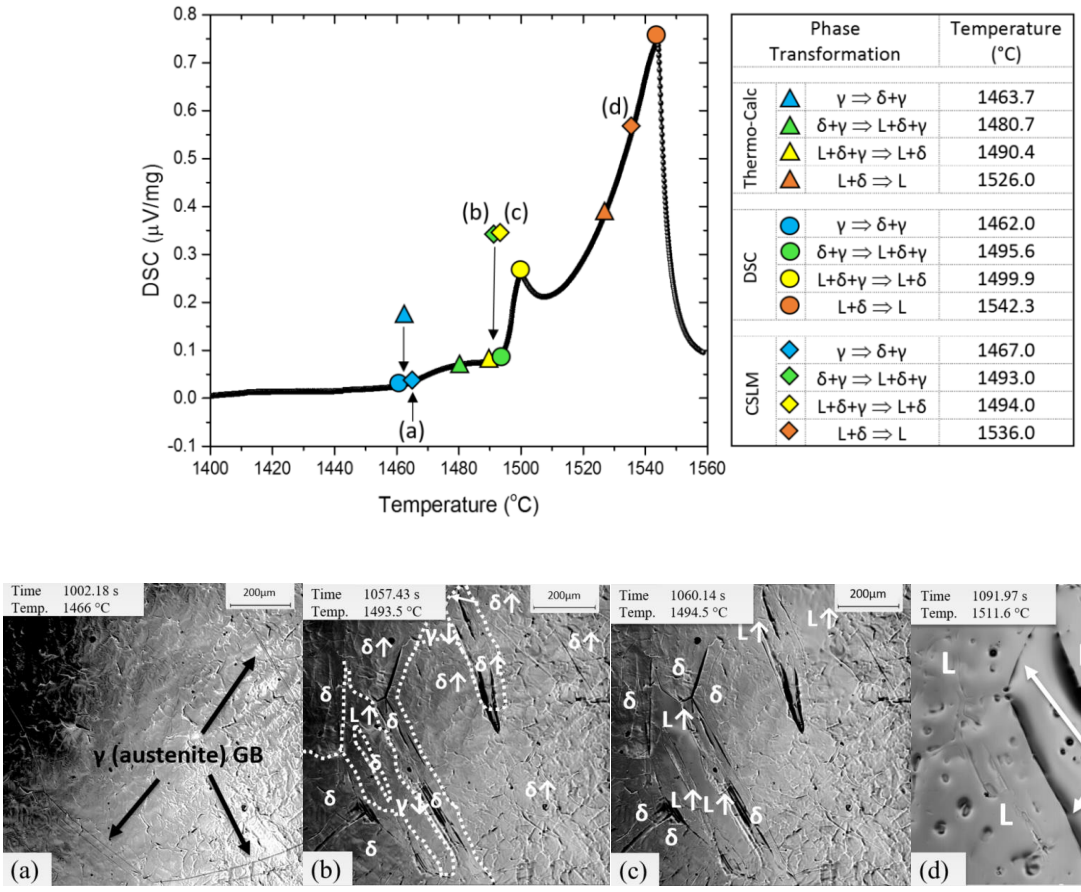

Figure 4.4 Combination of the DSC and CSLM results of the Hypo-P sample at a heating rate of 0.5 °C/s

Both DSC and CSLM phase transformation results and their measured temperatures correspond reasonably well to the calculated Thermo-Calc results, which suggests that the Hypo-P sample falls into the peritectic region and that the Non-P 1 sample is indeed non-peritectic.

4.4 Illustration and interpretation of the DSC curves during cooling

Literature work on the DSC cooling curves of peritectic steel is very sparse, and Wielgosz et al. [57] are the only authors who have previously reported it. However, as described in section 3.2, Wielgosz et al. [57] have shown only two distinct DSC cooling peaks, rather than the characteristic three peaks, which would be expected as seen with heating.

This section presents the DSC cooling curves for two steels, where the results for one of the steels (Hypo-P) is comparable to that illustrated in Figure 2.15b and described in the Wielgosz paper [57]. The main difference is that the heating and cooling rate used in the current research is 0.5 °C/s and the rates used in the Wielgosz paper are 0.08 and 0.33 °C/s.

The surface visualisation of the steel samples upon solidification has been done using CSLM under experimentally comparable conditions to illustrate the events, which occur on the steel surface.

4.4.1 Non-P 1 sample

The DSC curves of the Non-P 1 sample during cooling at 0.5 °C/s (Figure 4.5) show that solidification begins at 1506ºC. The CSLM results illustrate that the first solid phase that forms upon cooling and is seen on the surface of the molten droplet of the Non-P 1 sample at 1531ºC is believed to be δ. The temperature difference at the beginning of the solidification between the DSC and CSLM results can be explained by a theory of nucleation, which is described as a stochastic process [1].

All solidification starts with the formation of so-called nuclei at different locations in the molten metal, and then the crystals (or dendrites) grow from these nuclei. Undercooling is the necessary condition for the formation of crystals in a melt, so the temperature of the melt must be lower than the liquidus temperature of that metal. When the steel or alloy solidifies, the nucleation occurs on foreign particles or crystals, which are precipitated in the melt, called heterogeneities [26]. It can also occur at the bottom of the crucible or on the surface of the sample. Every time the nucleation point can vary together with the nucleation temperature, and it cannot be predicted during DSC and CSLM tests unless the solidification process is interfered on purpose to trigger the nucleation at the specific temperature, which was not the case in this study. Therefore, the nucleation temperature during DSC and CSLM tests has the random probability distribution, it cannot be predicted precisely, and it is difficult to obtain the same solidification temperature value even for the same sample for the same experimental conditions.

Upon further cooling, the dendrite arms grow and coarsen (Figure 4.5a), until the liquid phase fully solidifies at 1513ºC (Figure 4.5b). The occurrence of the solid state transformation, which is signified by a change to the surface relief (due to the density difference in δ and γ), confirms that the initially solidified phase was indeed δ (Figure 4.5c, d). The δ → γ transformation in the Non-P 1 sample was fast, it took about 1 second and was observed at 1405ºC, which is comparable to that, measured with DSC – 1401ºC.

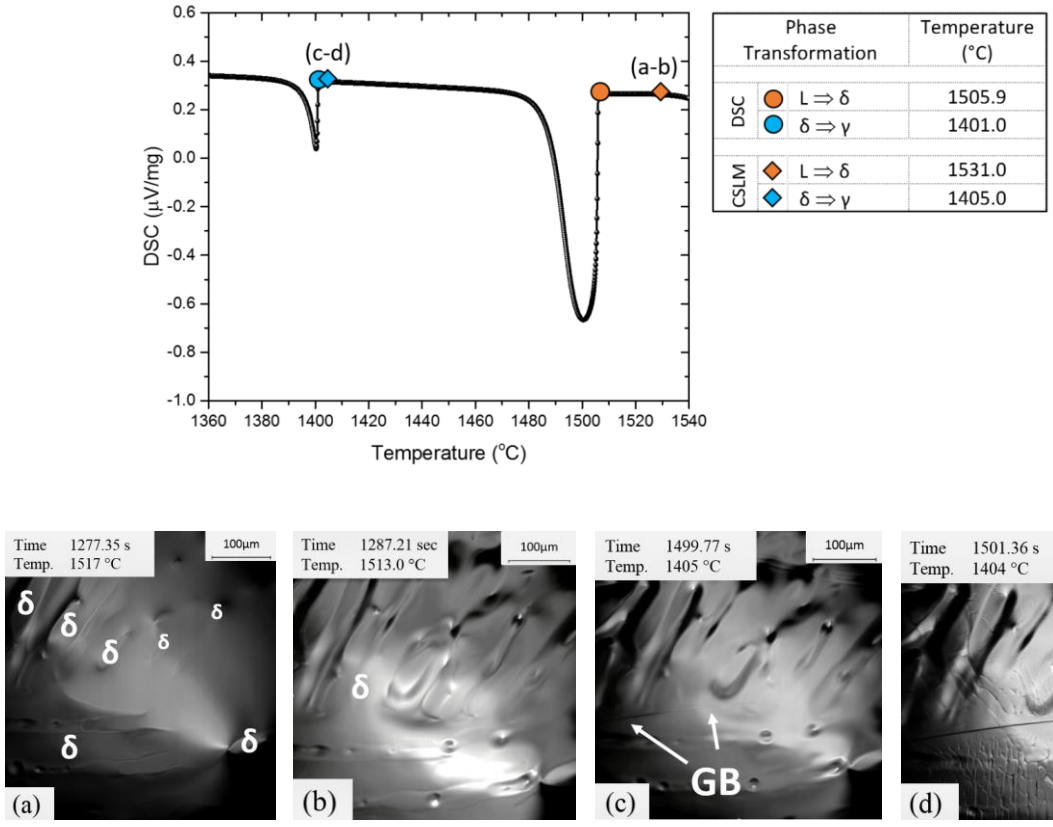

Figure 4.5 Combination of the DSC and CSLM results of the Non-P 1 sample at a cooling rate of 0.5 °C/s

4.4.2 Hypo-P sample

Even though the DSC curve exhibits three adjacent peaks upon heating of the Hypo-P sample, upon cooling, only two DSC peaks are distinguishable (Figure 4.6). The 1st cooling peak commences at 1501ºC, followed by a broad temperature range of about 70 ºC without significant enthalpy change, until the commencement of the 2nd peak at 1389 ºC.

The CSLM results show that upon cooling, the δ dendrites appear on the steel surface at 1511ºC, followed by the δ growth (Figure 4.6a), until the sample solidifies completely at 1495ºC, as illustrated in Figure 4.6b. During further cooling, no changes to the steel surface can be seen

for about 60ºC, until the commencement of the δ → γ transformation at 1434ºC (Figure 4.6c), which was completed within less than a second (Figure 4.6d).

A high undercooling in low carbon peritectic steels has been reported previously for the DSC tests [57,87]. As mentioned before in section 3.2, the authors suggested that the 2nd peak upon solidification refers to the peritectic reaction [57], assuming that liquid phase stays in the sample until the onset of the 2nd peak. However, CSLM observations (Figure 4.6a-d) show that all the liquid phase in the Hypo-P sample solidifies during the first peak and the sample stays in solid state for about 60 ºC until the δ → γ transformation occurs. If there is no liquid phase, the peritectic reaction cannot occur anymore because liquid phase is one of the main phases for the peritectic reaction (L + δ → γ), suggesting that the peritectic reaction must have occurred during the first peak.

The DSC cooling curves (Figure 4.6) also suggest that the solidification of the sample is followed by a stagnant area lasting for about 70ºC until the commencement of the 2nd peak suggesting it is unlikely that there is still highly undercooled liquid present during this stage. These facts strongly suggest that the peritectic reaction is not the cause for the 2nd DSC peak of the Hypo-P sample (as it was assumed before in [57]) because the liquid phase (which is needed for the peritectic reaction) is not preserved until the commencement of this 2nd peak. The reasons why the peritectic reaction does not occur in the second peak and why the DSC heating and cooling curves are different are described in the following section.

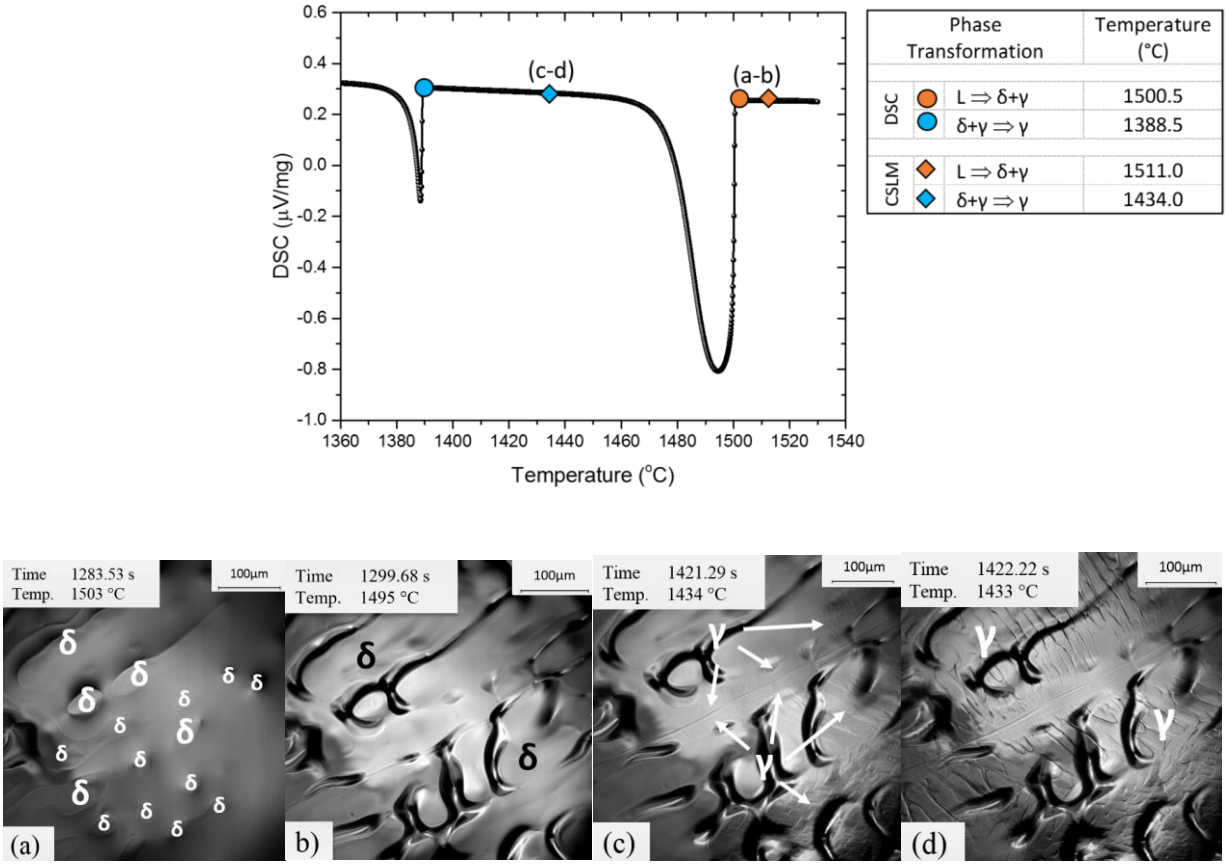

Figure 4.6 Combination of the DSC and CSLM results during the controlled cooling of the Hypo-P sample

4.5 The detailed reasons for the discrepancy in the DSC heating and cooling curves of the Hypo-P sample

It is established that DSC cooling curves (Figure 4.5 and Figure 4.6) consistently exhibit 2 peaks with strong undercooling, regardless of whether the investigated sample is a peritectic grade or not. This is consistent with the limited information previously reported [57,87], but not with the expected number of peaks corresponding to the 3 adjacent transformation events, which are observed upon heating of the Hypo-P sample.

For additional investigation into the reason for only 2 peaks during cooling, further DSC measurements were conducted for a pure iron (Fe) sample (Figure 4.7). At a cooling rate of 0.5 °C/s, the solidification of Fe occurs at 1520°C, followed by a region of single δ. Then, δ transforms to γ at 1358°C, which is 36°C below the equilibrium temperature of the δ → γ transformation of pure iron (Figure 4.7).

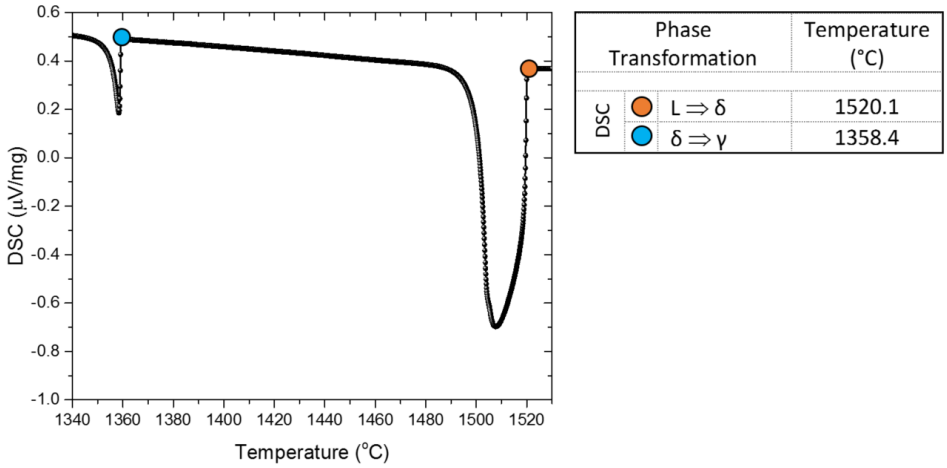

Figure 4.7 DSC results during the controlled cooling of pure iron (Fe)

To understand the phase transformation at the 2nd DSC peak of the Hypo-P sample, the onset temperatures of the 2nd DSC peaks in all samples were compared to the equilibrium temperatures when δ fully transforms to the single-phase γ. The difference between the calculated and measured temperature values is summarised in Table 4.1.

Table 4.1 The extent of undercooling of the 2nd peaks below the equilibrium temperature of the single-phase γ, when γ transforms from δ in the Hypo-P, Non-P 1 and pure Fe samples

Samples	Equilibrium temperature (T_E) of the single-phase γ upon cooling, °C	Onset of the measured temperature (T_M) of the 2nd DSC peak, °C	Undercooling of the measured temperature below the equilibrium temperature, °C ($\Delta T = T_E - T_M$)
Hypo-P	1463.7	1388.5	75.2
Non-P 1	1432.9	1401.0	31.9
Pure Fe	1394.0	1358.4	35.6

The DSC cooling curve of the Non-P 1 steel shows that after complete solidification of δ, it then transforms to γ at 1401°C (Figure 4.5), which is about 32°C lower than the equilibrium temperature (Table 4.1). The 2nd peak during cooling of the Hypo-P sample occurs at 1389°C (Figure 5.6). This is comparable to the δ to γ transformation, observed in Fe and the Non-P 1 steel, even though it is about 75°C below the equilibrium transformation temperature (Table 4.1).

It is found that there is a high undercooling of the 2nd DSC peak of the Hypo-P sample below the equilibrium temperature of the single-phase γ. Moreover, the onset temperature of that peak falls into the temperature region of the measured δ→γ transformation between the Non-P 1 and pure Fe (Table 4.1). These facts suggest that the chemical composition of the δ phases in the Non-P 1 and pure Fe samples, which transform to γ at the 2nd DSC peak, can be comparable.

To understand the proposed idea, it is important to note that the maximum carbon concentration in δ in both samples is limited (about 0.075% according to Thermo-Calc predictions in Figure 3.1a). The solidification of both Non-P 1 and pure Fe samples accompanies the nucleation and growth of δ dendrites until the sample reaches single phase δ. The average carbon concentration in the Hypo-P sample is about 0.11%. Therefore, during solidification, the rest of the carbon in the Hypo-P steel is rejected into the liquid along with other alloying elements, in front of the solidifying δ. The progression of the L/δ interface leads to the formation of solute concentration gradients, causing the remaining L to solidify as γ and isolate δ from L, as suggested in [1,64]. Once a boundary layer of γ forms around the δ dendrite core, the rate-limiting step for the back diffusion of carbon into δ is diffusion through the γ ($D_\gamma = 1 \cdot 10^{-9}$ m^2/s) , as this is slower than diffusion in L ($D_L = 2 \cdot 10^{-8}$ m^2/s) or δ ($D_\delta = 3.95 \cdot 10^{-9}$ m^2/s) [52,85]. This can cause the δ dendrite core with a reduced solute concentration to transform to single phase γ at a lower temperature when δ cannot exist any longer, which is below 1394°C. Such behaviour is illustrated in Figure 4.6 when the onset temperature of the 2nd peak is shown at 1388.5°C. This strengthens the idea that the 2nd peak represents δ→γ transformation and not the peritectic reaction, which was assumed before by Wielgosz et al. [57].

To further confirm that the 2nd peak is not a result of a peritectic reaction, the area of the peaks, which indicate the heat flow, was evaluated for all samples (Figure 4.8). The area of the 1st peak varies between 27 to 43 µVs/mg during solidification of all samples. By comparing this variation among all samples, it can be seen that it is 38% and 23% larger in the Hypo-P, compared to the Non-P 1 and Fe samples respectively, suggesting that the peritectic reaction could be occurring during the 1st peak during solidification. Thermo-Calc calculations also indicate that the solidification of the Hypo-P sample results in a larger exothermic reaction compared to the Non-P 1 and Fe samples due to the peritectic reaction (Figure 4.2).

While the measured enthalpy differences (µVs/mg) are in qualitative agreement with the trends computed by Thermo-Calc, the qualitative equilibrium enthalpy data (J/g) is significantly larger. This measured data in J/g can only be comparable with the calculated enthalpy data in J/g if the instrument sensitivity coefficient is above 0.3 µV/mW. Several parameters, like the sample carrier and thermocouple type, the atmosphere during the test and the crucible material, can increase or decrease the sensitivity coefficient. The estimated coefficient in the current DSC study is 0.117 µV/mW. Thus, the results are shown in µVs/mg in Figure 4.8 and not in J/g. When all tests are conducted under comparable conditions, the obtained qualitative measured

data in μVs/mg is still reliable. The error bars shown in Figure 5.8 represent the sensitivity of the DSC equipment.

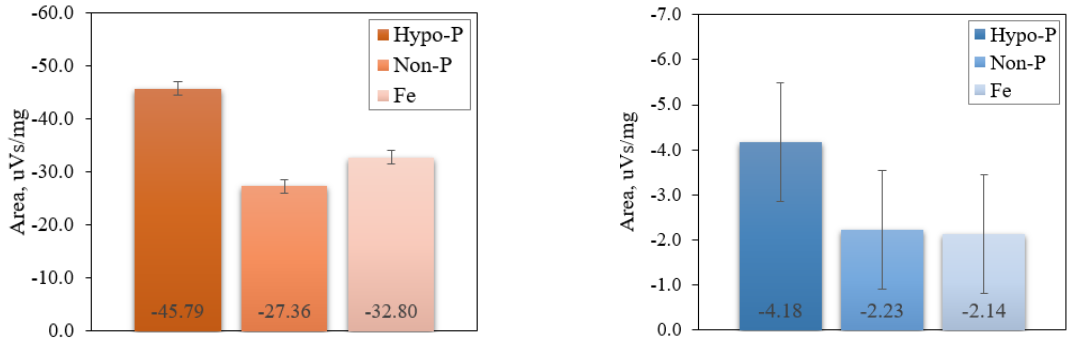

(a) (b)

Figure 4.8 Area under the (a) 1st and (b) 2nd DSC peak during cooling of the Hypo-P, Non-P 1 and Fe samples

As it was suggested above, during solidification of the Hypo-P sample, the 1st peak indicates the growth of δ dendrites (depleted in carbon and the other elements), causing the remaining L to solidify as γ. This is, in fact, the occurrence of the peritectic reaction when the liquid reacts with δ to form γ. Moreover, this causes the larger exothermic heat released by the Hypo-P sample, compared to the Non-P 1 and pure Fe samples, as suggested by the Thermo-Calc calculations (Figure 4.2) and shown in Figure 4.8a.

The area of the 2nd peak in all samples is about 91-93% smaller (2 - 4 μVs/mg), compared to the area of the 1st peak, regardless of whether the sample is peritectic or not (Figure 4.8). Thermo-Calc shows that the peritectic reaction does not occur in the pure iron and Non-P 1 samples. DSC results suggest that the area of the 2nd peak in all three samples may overlap (Figure 4.8b), so they release a comparable amount of heat during the transformation. This is additional evidence that confirms that the 2nd DSC peak of the Hypo-P sample shows the solid-state transformation of the solute poor δ dendrite core to γ and not the peritectic reaction, as was previously assumed [57].

As it is confirmed above, the total heat release in the Hypo-P steels is bigger compared to the Non-P 1 and pure Fe samples. If more heat is rejected during solidification of the Hypo-P steels, the more heat must be extracted during the continuous casting process. Therefore, to cope with the excessive heat, rejected by the steel, the solution is to slow down the casting speed. As mentioned in the Introduction section, the reduction of the casting speed is indeed widely used nowadays to avoid defect formation in peritectic steels.

4.6 Summary

CSLM and DSC experiments were carried out under slow heating and cooling rates for peritectic and non-peritectic steels. Both experimental methods have limitations, which are discussed; however, they complement each other in defining the phase transformation behaviour of investigated steels in the high-temperature range. The following conclusions can be drawn:

- The CSLM results of the investigated steels are in reasonable agreement with the DSC results conducted at a heating rate of 0.5 °C/s and with literature;
- During cooling, the DSC curves always exhibit only 2 distinct enthalpy peaks with strong undercooling, regardless of whether the investigated sample is a peritectic grade. This can be explained by the formation of a boundary layer of γ around the δ dendrite core, which slows the carbon diffusion through the γ, thus postponing the δ to γ transformation;
- During heating, the peritectic behaviour in steels is easily determined based on the DSC curves. However, this is not the case in cooling, making it difficult to define the point of peritectic transformation. Using CSLM results, we were able to establish that there was no liquid in the intermediate period between the 1^{st} and 2^{nd} DSC peaks upon solidification;
- The 1^{st} DSC peak during solidification of the Hypo-P sample is associated with larger energy release than the Non-P 1 and Fe samples. However, the 2^{nd} DSC peak shows a much smaller energy release, compared to the 1^{st} DSC peak, which is comparable to the heat released by the Non-P 1 and pure Fe;
- The peritectic reaction was proved to occur at the 1^{st} peak during solidification of the Hypo-P steel, and not at the 2^{nd} peak, as it was assumed in the previous research [57];
- One of the main solutions worldwide to cast peritectic steels with minimum defects is to reduce the casting speed. The current Chapter has shown that this is necessary to accommodate the excessive heat, rejected by the peritectic steel (Hypo-P) during solidification;
- Although peritectic steel release more heat during solidification, compared to the non-peritectic sample, but these conclusions are based on the qualitative data and not quantity. Therefore currently is indicates that the DSC is not a right method to study the peritectic reaction during cooling unless it becomes possible to measure the amount of the heat released more accurately during the solidification of steels and to make the nucleation temperature more

consistent. This will improve the repeatability of the results and it will give more useful information for the materials characterisation.

Chapter 5 Real-time Measurement of the Solidification Shrinkage of Peritectic Steels

5.1 Introduction

As was summarised in Chapter 2, peritectic steels are more sensitive to defect formation during the continuous casting process compared to non-peritectic steels. It was suggested that one of the reasons for the surface defects is the large and rapid shrinkage, associated with peritectic reaction and transformation. However, currently, there is no sufficient information on the exact measured value of the shrinkage in peritectic steels, which occurs when the liquid phase transforms into solid.

Section 2.10 describes previous experimental attempts to measure the shrinkage of steels during and after solidification by Mehrara et al. [76]. The authors obtained a larger solidification shrinkage in the low carbon aluminium-killed (LCAK) steel sample than in high-strength low-alloy (HSLA) steel. It was also noted that LCAK steel was known to be more sensitive to defect formation during continuous casting and mechanical testing compared to the HSLA steel used in that research. Thus, it was concluded that the volume change during solidification of steel could be measured and it also could be an indication of the hot cracking susceptibility of steel.

As shown in Section 3.4.1, the thermodynamic calculations for the current study predict a larger solidification shrinkage of the Hypo-P sample compared to the Non-P 2 sample. As this information is in agreement with the literature review, then comparable shrinkage experiments, described by Mehrara et al. [76], were conducted for the Hypo-P and Non-P 2 samples to obtain actual results for the volume change. The effect of cooling rate on the solidification shrinkage is also studied using this technique. Additionally, the solidification behaviour of steels during shrinkage tests was analysed using the IR Camera.

Section 2.10 summarises the unresolved issues of the previous studies during the solidification shrinkage technique, and Section 3.4 shows the improved methodology for this technique, which is used in the current research.

The objectives and hypotheses to be investigated were explained in Section 1.1, but the parts relevant to this part of the study are:

1) To determine and compare the solidification shrinkage of peritectic and non-peritectic steels in real-time conditions under different cooling rates, comparable with the CC process. This can be done using the water-cooled copper mould where the molten metal is poured to and where it rapidly solidifies to mimics the solidification behaviour of the steel shell during the CC process.

Based on the theoretical values, which have been produced using thermodynamic software (Thermo-Calc), it was found that the solidification shrinkage is larger in the hypo-peritectic steels compared to the non-peritectic. However, based on the literature survey on this topic, the solidification shrinkage values have not been thoroughly studied in past research. Therefore, such an investigation is of great importance. In the present study, the evaluation of the shrinkage formation during peritectic transformation will be made based on previous research [76,92]. The area of interest is a solidification shrinkage of steel starting from the liquidus temperature at around 1530°C until approximately 1300°C, where a microstructure of single-phase austenite is achieved.

- It is hypothesised that the hypo-peritectic steel (Hypo-P) exhibit a greater measured solidification shrinkage than non-peritectic one (Non-P 2).

2) To evaluate the influence of cooling rate on the solidification shrinkage behaviour of steels. The technique adopted in this study was improved to allow the characterisation of the shrinkage of the steel at high cooling rates.

- It is hypothesised that at a slow cooling rate, during initial stages of solidification, the non-peritectic and hypo-peritectic steels shrink less in comparison with high cooling rates.

5.2 Measurements of the solidification shrinkage

As explained in Section 3.4.1, the Thermo-Calc calculations of the volume changes (which are mainly based on the density difference between the phases) show a large radial slope during shrinkage formation of the Hypo-P and Non-P samples as soon as they are cooled down below the liquidus temperature as illustrated in Figure 5.1. Then Hypo-P sample shows a rapid volume decrease associated with a peritectic reaction before it reaches the gradual linear volume decrease, which is observed below the solidus temperature when the shrinkage reaches 1.6%. In the Non-P 2 sample, which does not undergo the peritectic reaction, the radial shrinkage slope steadily changes to the linear slope after the sample reaches the solidus temperature when the shrinkage is about 1.4%. In an attempt to measure the real-time shrinkage and estimate the accuracy of the thermodynamic calculations, the solidification shrinkage technique was conducted, and the results are described in this section below.

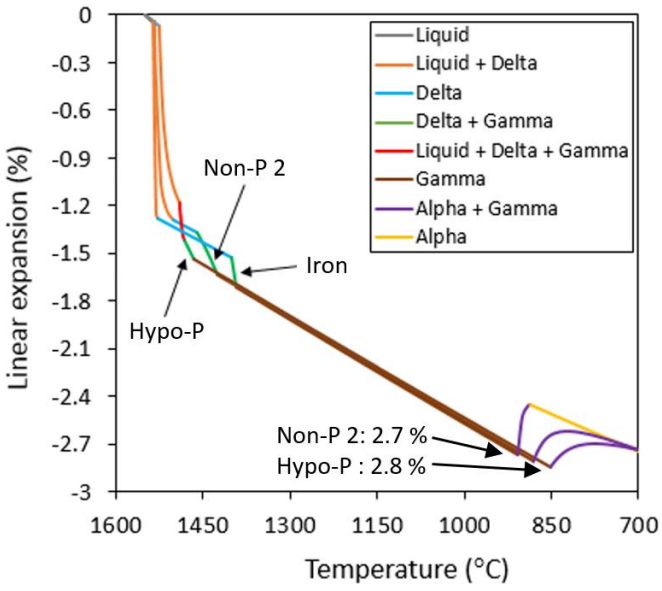

Figure 5.1 Comparisons of the Thermo-Calc calculations of the linear solidification shrinkage for the Hypo-P and Non-P 2 samples. For comparison, the solidification behaviour of pure iron is also included in the plot

An example of the measured solidification shrinkage is shown in Figure 5.2. After the molten steel is poured into the mould, the pre-shrinkage expansion is observed in the sample. This occurs due to the evolution of gases within the sample [92] when carbon dissolved in the steel reacts with oxygen in the atmosphere to form CO and CO_2. The pre-shrinkage expansion is then followed by the solidification shrinkage when liquid phase transforms to solid.

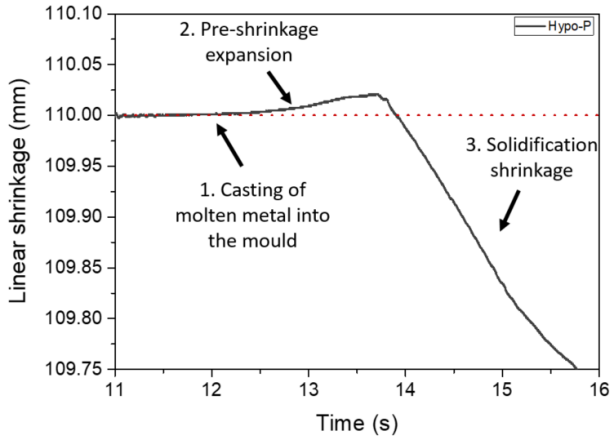

Figure 5.2 An example of the measured solidification shrinkage

During the continuous casting process, the cooling rate varies across the steel slab or bloom, and this also affects the shrinkage. Thus, the effect of the cooling rate on the solidification shrinkage results is also evaluated and discussed in this chapter. The slow cooling rate of about 40 °C/s is achieved using a graphite mould. The fast cooling rate of up to 100°C/s (which is close to the cooling rate at the steel shell during the CC process as mentioned in section 2.2) is reached using a water-cooled copper mould. A more detailed explanation about this technique can be found in section 3.4.

It was reported, that some parameters, like the length of the sample and the friction between the moving wall and the mould wall, do not affect the solidification shrinkage of the steels and alloys [76]. However, in general, the solidification shrinkage experiments are very delicate because there are many parameters, which can directly affect the solidification shrinkage results. Some of these parameters are listed in Mehrara et al. paper [76]:

- Casting mass, which can change the thermal gradient and therefore, the solidification pattern of the sample;
- Casting height, which can also alter the solidification shrinkage pattern. The thicker the sample, the higher the chances of non-uniform volume shrinkage (for example, when the bottom of the sample is solid, but the top is still liquid). So, to achieve a more uniform thermal gradient across the sample, the height of the metal, which solidified in the mould was recommended to be up to 10mm.

Therefore, high attention was given in the attempt to achieve the same sample mass of about 200 g and sample height of about 10 mm for all investigated samples, as well as comparable casting temperature for all samples during every experiment.

Figure 5.3 shows the linear solidification shrinkage results measured in two consecutive tests for non-peritectic (Non-P 2_2 and Non-P 2_3) and peritectic (Hypo-P_2 and Hypo-P_3) samples. As predicted by the Thermo-Calc calculations, the Hypo-P sample exhibits a rapid volume decrease before the radial shrinkage slope changes to the gradual linear slope, which is not the case in the Non-P 2 samples, where a gradual volume decrease is observed (Figure 5.1). However, based on the measured data, it is hard to find the point when the radial shrinkage slope changes to the linear one. It can be assumed that for the non-peritectic steel (Figure 5.3 (a)) it occurs when the linear shrinkage reaches 0.36% (Non-P 2_2) and 0.21% (Non-P 2_3), which is less compared to the calculated 1.4% (Figure 5.1). For the hypo-peritectic steel (Figure 5.3 (b)), the change from radial to linear slope occurs when the shrinkage reaches 0.18% (Hypo-P 2) and 0.31% (Hypo-P 3), which is also less compared to the calculated 1.6% (Figure 5.1).

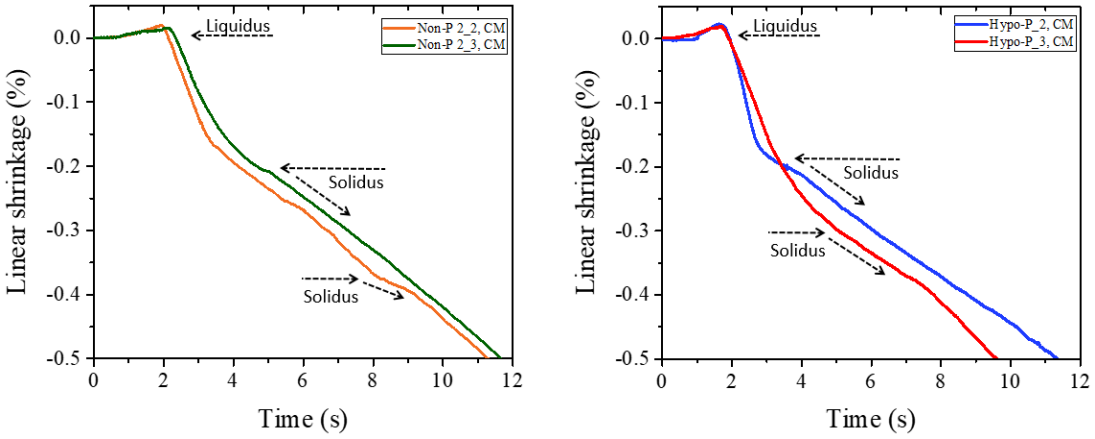

(a) (b)

Figure 5.3 Solidification shrinkage results measured in two consecutive tests for (a) non-peritectic (Non-P 2_2 and Non-P 2_3) and (b) peritectic (Hypo-P_2 and Hypo-P_3) samples

A small measured shrinkage, compared to the calculated one, may be due to the formation of porosity during solidification as a result of the gas formation [92], such as CO and CO_2. The illustration of the porosity found in the cross-section of the Non-P 2 sample which solidified during the shrinkage measurements is shown in Figure 5.4.

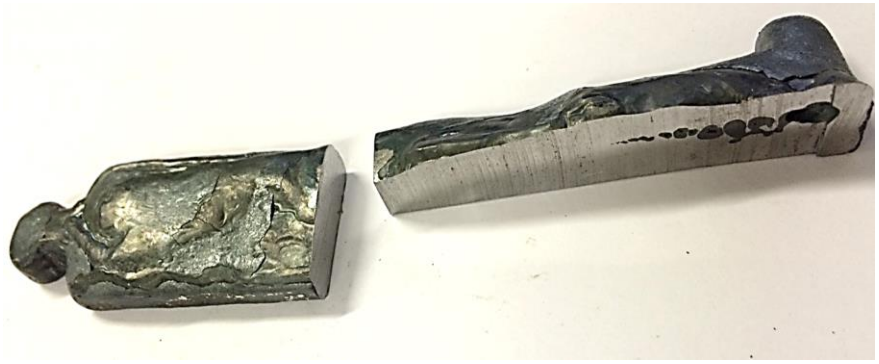

Figure 5.4 Cross-section of the Non-P 2 sample solidified during the shrinkage measurements, which indicates the porosity inside the sample

Therefore, even though all initial conditions for all samples were comparable during all tests, it was found that there is a significant error between the two comparable measurements for the same steel grade as illustrated in Figure 5.3. This makes it difficult to draw any comparison between the shrinkage in different steel grades during slow (graphite mould) or fast (copper mould) cooling as illustrated in Figure 5.5, which includes the additional shrinkage results (Hypo-P_1, Non-P 2_1) to show the variation in the shrinkage results. This error is likely caused by variations in the temperature gradient during cooling, resulting from a different degree of oxidation; contact conditions between the melt and mould during pouring; and gas formation during solidification.

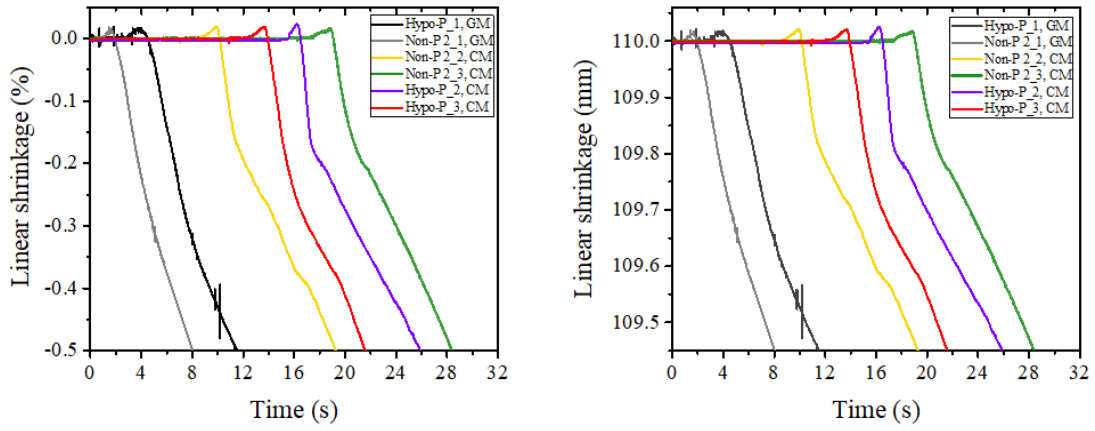

(a) (b)

Figure 5.5 Linear shrinkage measurements of Non-P 2 and Hypo-P samples during solidification (GM – Graphite mould, CM – Copper Mould)

To verify the proposed idea, the IR camera was used during the shrinkage experiments to analyse the solidification behaviour of the samples. More details about the application of the IR camera can be found in section 3.4.3. The IR camera allows of plotting the temperature gradient on the surface of the casting during pouring, solidification and further cooling.

The thermal imaging analysis suggests that, once the sample solidifies, the variation of the temperature gradient between the minimum and maximum values is high. For the Non-P 2 sample, it varies by 280 °C across the sample and 330 °C along the sample, as illustrated in Figure 5.6.

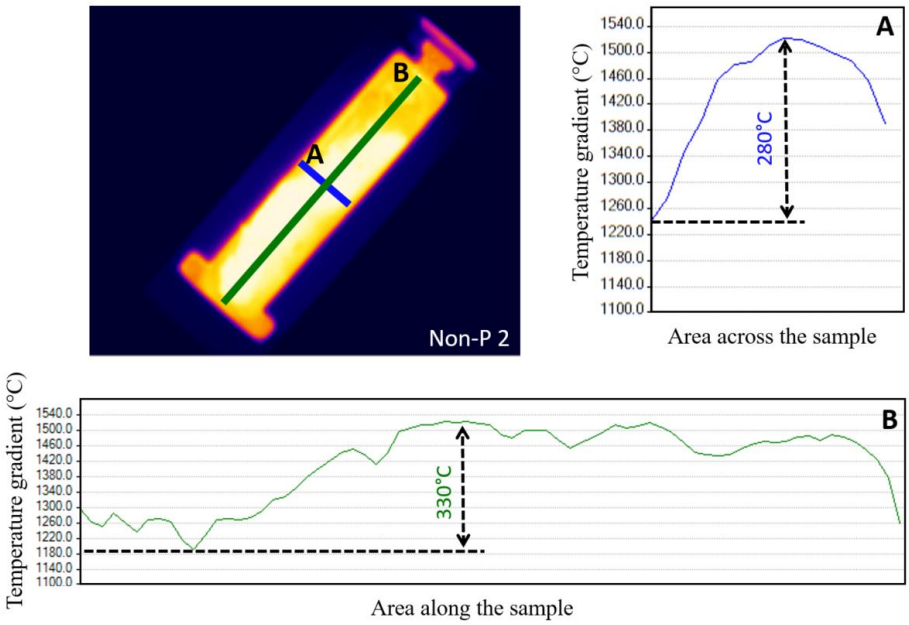

Figure 5.6 Temperature gradient across (A - blue curve) and along (B - green curve) the Non-P 2 sample, once it solidifies

For the Hypo-P sample, the temperature gradient varies by about 300°C across and along the sample, as shown in Figure 5.7. Moreover, the thermal gradient along the Hypo-P sample has more fluctuations between the minimum and maximum temperature than the Non-P 2 sample. This fact suggests that the transformations in the sample also occur un-uniformly, which affects the shrinkage results because it becomes harder to distinguish clear volume changes, associated with the phase transformations. This also correlates well with the information, summarised in Chapter 1, that the surface of the peritectic steels often looks uneven during the CC process, compared to non-peritectic steels.

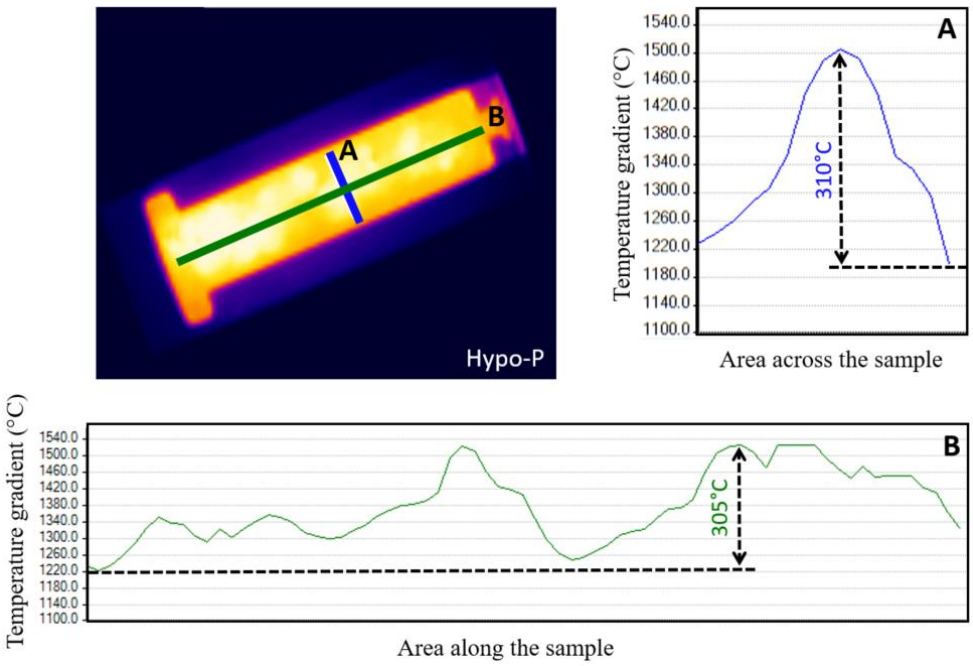

Figure 5.7 Temperature gradient across (A - blue curve) and along (B - green curve) the Hypo-P sample, once it solidifies

Further evidence, which suggests that the transformation of the Hypo-P steel occurs at a different time, is shown in Chapter 4. It was illustrated that when comparing the DSC and CSLM results, the transformation temperature from δ to γ varied by 45.5 °C for peritectic steel. Whereas for non-peritectic steel, the difference between the transformation temperatures was only 4°C. The reason behind this was also described in detail in Chapter 4. It was suggested that the δ to γ transformation temperature in the Hypo-P steel strongly depends on the number of segregated elements around the depleted δ during solidification. The higher amount of the segregated element, the sooner the δ to γ transformation occurs, but it is hard to predict and control the amount of the segregated elements in front of the solidifying δ dendrite. The uneven surface of the peritectic steel during casting leads to a less uniform cooling of the cast, and thus it behaves less predictably. Therefore, the volume shrinkage cannot be quantitatively measured during solidification of steel during the CC process as the thermal gradient across the sample is also affected by the non-uniform shrinkage of the steel surface. As for the Non-P 2 sample, the temperature gradient shows fewer fluctuations compared to the Hypo-P sample. Despite that, the conclusions about the shrinkage of the Non-P 2 samples still cannot be drawn due to the large error in the experimental results. This error is mainly caused by gas formation (CO, CO_2) during solidification and a temperature gradient along the sample affected by the contact conditions between the melt and mould during pouring, which eventually leads to the non-uniform cooling and shrinkage.

Although no defined transformation was observed in the shrinkage data between Hypo-P and Non-P samples under comparable cooling conditions, the differences were seen during different cooling rates. Figure 5.8 (a) shows the initial stages of solidification when an initial rapid shrinkage is followed by a more consistent slope. By plotting a tangent from the initial solidification to the linear portion of the shrinkage, a proportional rate of shrinkage can be seen between the steels. The peak length between the shrinkage curve and tangent can be calculated using ImageJ [95,96] software. Figure 5.8 (b) illustrates that the Non-P 2 sample shrinks at a slightly slower rate than the Hypo-P sample in both graphite and copper moulds. However, due to the large error between the results, it is hard to distinguish it. It can also be seen that, as expected, the higher shrinkage rate is observed during faster cooling (in the water-cooled copper mould).

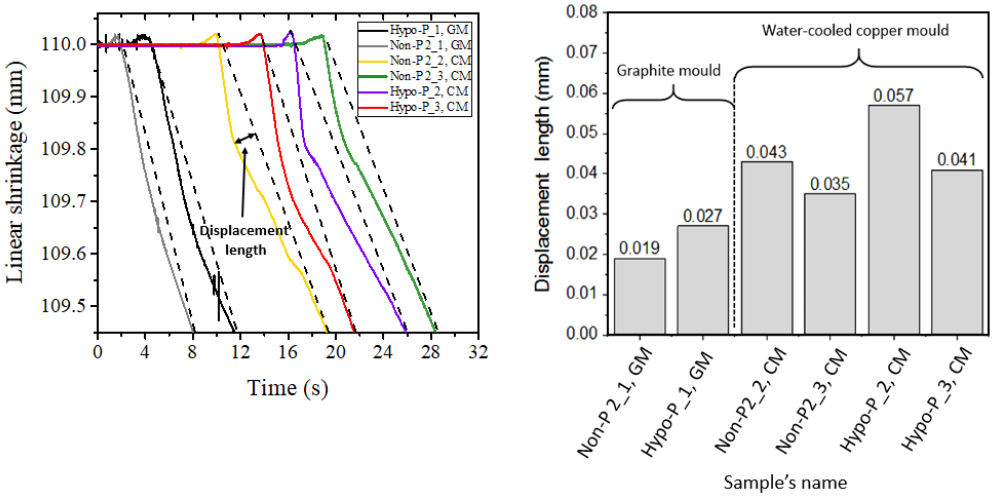

(a) (b)

Figure 5.8 Displacement measurements of the Non-P 2 and Hypo-P samples during solidification (GM – Graphite mould, CM – Copper Mould)

The full range of the linear shrinkage data is shown in Figure 5.9. The experimental shrinkage results for the Non-P 2 and Hypo-P steels (Figure 5.9 (a)) show that the shrinkage reaches about 1.8% when γ transforms to α in both samples in the graphite and copper moulds. However, Thermo-Calc predicts that the shrinkage of both samples must be about 3% before the γ to α transformation. The lower measured shrinkage values are likely to be due to the formation of porosity, as was also suggested by Mehrara et al. [76] and Eskin et al. [92].

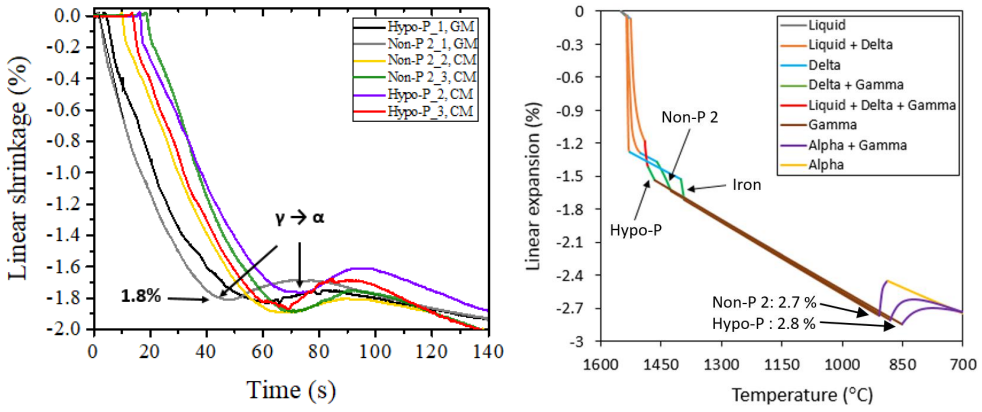

(a) (b)

Figure 5.9 Measured (a) and calculated (b) linear shrinkage measurements of the Hypo-P and Non-P 2 steels

It is interesting to note that the volume expansion due to the γ → α transformation is evident for all samples as illustrated in Figure 5.9, whereas, the volume changes are not so clear at the initial solidification stages. As proposed above, due to the large temperature gradient across and along the sample, when liquid transforms into solid, it is hard to distinguish apparent volume changes, associated with the phase transformations. However, once the sample is fully solid and it approaches the γ to α transformation, the temperature ranges for both steels reduces to about 60-65°C across the sample and about 110-125 °C along the samples (Figure 5.10 - Figure 5.11). Therefore, a more prominent transformation is observed when the thermal gradient is narrower for both steels.

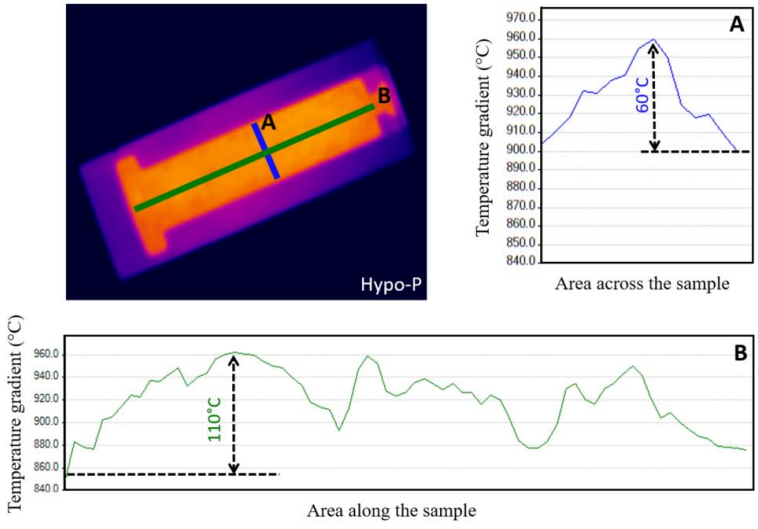

Figure 5.10 Temperature gradient across (A - blue curve) and along (B - green curve) the Hypo-P sample, when γ transforms to α

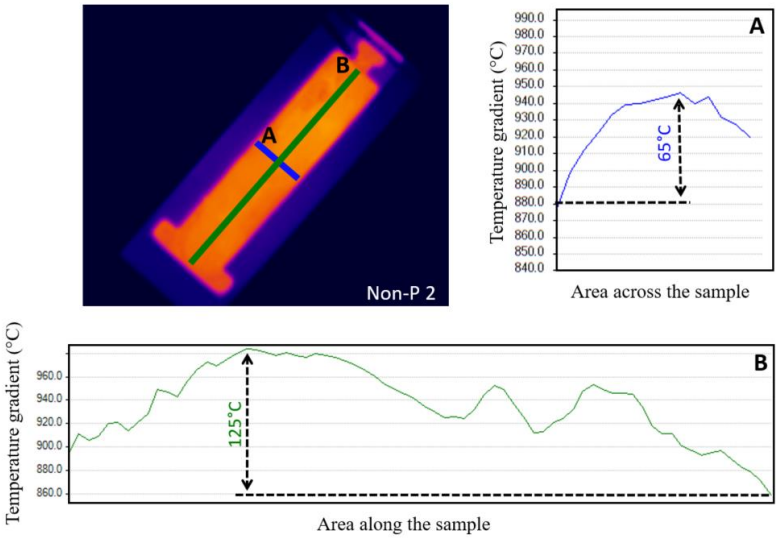

Figure 5.11 Temperature gradient across (A - blue curve) and along (B - green curve) the Non-P 2 sample, when γ transforms to α

5.3 Thermal Imaging Results

Due to the low emissivity value of liquid steel (around 0.3), thermal imaging cameras can pick up aspects of solidification that are otherwise hard to study. By calibrating the thermal imaging camera to the melting point of pure iron, the emissivity of as-cast steel was found to be around 0.85 (within the range of 0.6-0.9 seen in the literature [97,98]).

The casting experiments were conducted by monitoring the sample surface area using a thermal imaging camera. The most effective way to prove the assumed emissivity of the steel surface is the correlation of the slopes of the temperature curves with the corresponding phase transformations. This was carried out with grade 4 iron where both the $\delta \rightarrow \gamma$ and $\gamma \rightarrow \alpha$ transformations were accurately measured to within ±5 °C.

Figure 5.12 (a) shows the apparent temperature of the sample (calculated based on the emissivity value of solid iron), as the sample cools from liquid to solid in pure iron taken from roughly the centre of the sample. As the emissivity is set to the solid iron, then the liquid appears to be cooler, while the steel is liquid. However, as soon as the steel solidifies, there is a rapid change of the thermal profile after 3rd second and the apparent temperature increases, because the emissivity, which is set for the solid iron, can be correlated with the temperature of the sample at that moment. This study has also been reported before by Nagarajan et al. [99]

The temperature fluctuations from 0 s until 3.2 s represent that the metal was liquid (caused by the flow of molten metal), as can be seen in the thermal profile (Figure 5.13.1) captured immediately after casting using TIC. Then, while the sample was solidifying, the temperature began to rise after 3 s to form δ-Fe which can be observed in Figure 5.13.2. Upon further cooling, the δ to γ transformation started after 20 s (Figure 5.13.3 – 5.13.4) at around 1400 °C (Figure 5.12 (b)). The γ to α transformation was observed after 48 s at around 920 °C and is shown in Figure 5.12 (c).

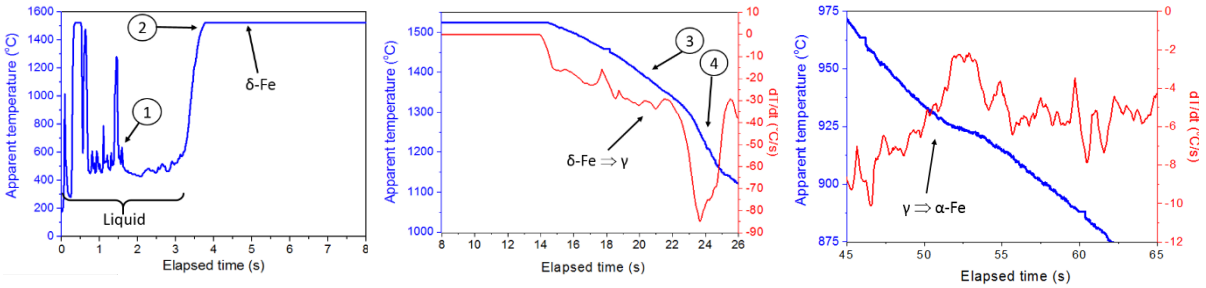

L ⇒ δ – Fe δ – Fe ⇒ γ γ ⇒ α-Fe

Figure 5.12 Apparent temperature measurements of the pure iron during solidification in the graphite mould

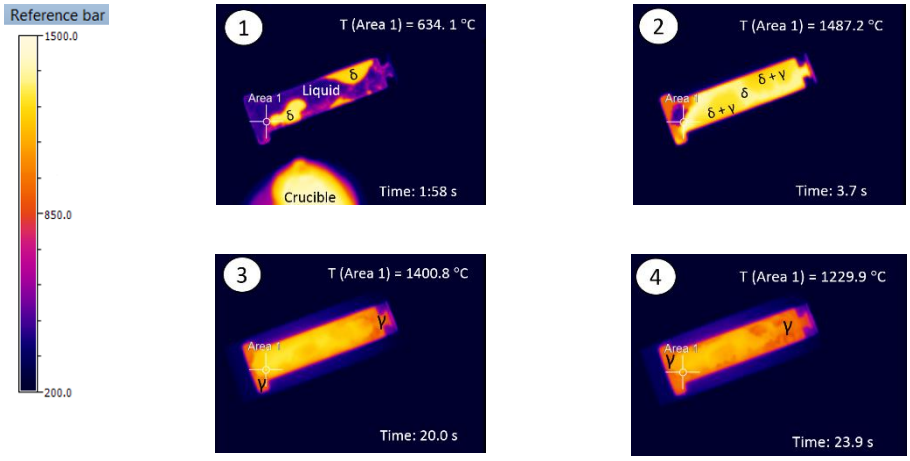

Figure 5.13 Infrared imaging for the solidification of pure iron from liquid to solid state during shrinkage experiments

Figure 5.14 shows a comparison of the solidification of Non-P 2 and Hypo-P samples. In Non-P 2 sample (Figure 5.14 (a)), a liquid phase was observed between 0 –2.5 s, then the temperature increased and stabilised at around 1200 °C, referring to the mushy zone where a combination of emissivity of liquid and solid metal is emitted. When L+δ transforms into the solid δ, the temperature increases after 9 s to 1500 °C. The solidification process observed in Hypo-P

sample is different (Figure 5.14 (b)). After Hypo-P sample starts to solidify and forms the mushy zone of L+δ after 2 s, the cast seems to show a reversion back to liquid before making the final transformation to δ+γ. It was stated earlier that a larger temperature difference was seen in the Hypo-P sample compared with the Non-P 2 due to the different latent heat. This latent heat is the probable cause for the destabilisation of the liquid phase seen here.

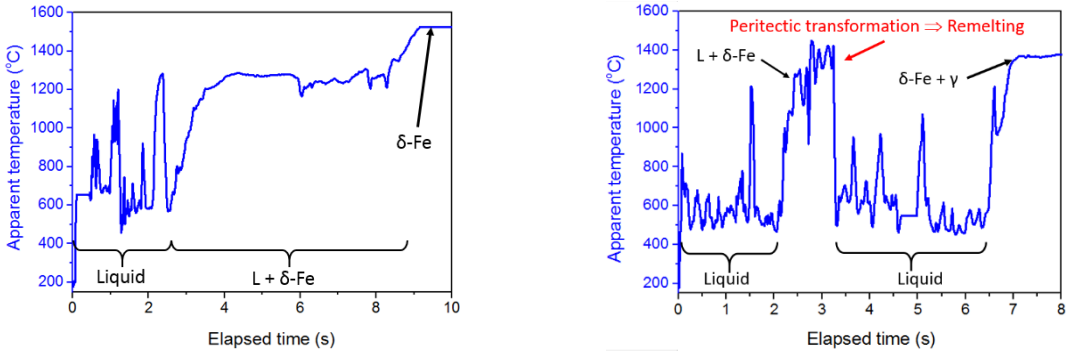

Non-P 2: L ⇒ L + δ – Fe ⇒ δ – Fe

Hypo-P: L ⇒ L + δ ⇒ L + δ + γ ⇒ γ

Figure 5.14 Temperature measurements of the Non-P 2 (a) and Hypo-P (b) samples during primary solidification in the graphite mould

Thus, a big difference during solidification of peritectic and non-peritectic steel can be observed using the IR thermography, which can help better understand the problems appearing during the solidification of the molten metal. This technique may be useful for the assessment of the solidification behaviour of a new product at the laboratory scale before starting to produce material at a larger scale.

During the peritectic transformation, when Liquid + δ transforms to γ, a release of latent heat may increase the temperature of the steel and therefore stabilise the liquid fraction. This event may not happen in the pure iron and Non-P 2 sample because the transformation from δ to γ occurs at a lower temperature (below solidus temperature). Therefore, this will physically occur further away from the L to δ transformation within the cast, influencing it to a lesser degree.

5.4 Summary

Solidification shrinkage experiments were carried out under various fast cooling rates for Hypo-P and Non-P samples. Although some information can be deduced from the shrinkage testing, in-depth understanding of the peritectic transformation and the reasons behind formation of the non-uniform surface of the Hypo-P samples cannot yet be fully characterised by this method. Based on the shrinkage results, the following conclusions can be reached:

- The solidification shrinkage shows a significant error of the measured results for a single condition for a single steel grade. The error is mainly caused by the temperature gradient along the sample affected by the contact conditions between the melt and mould during pouring, which eventually leads to non-uniform cooling (and therefore non-uniform shrinkage). In addition, the error can be caused by gas formation during solidification;
- Due to the large temperature gradient, and variation from sample to sample, it becomes harder to distinguish clear volume changes, associated with the phase transformations;
- The thermal gradient along the Hypo-P sample has more fluctuations between the minimum and maximum temperature than the Non-P 2 sample. The δ to γ transformation temperatures may also vary for the Hypo-P sample during the experiments, which was observed in the previous chapter and reported in the literature review;
- The Non-P 2 sample shrinks at a slightly slower rate than the Hypo-P sample during the initial stages of solidification in the graphite and copper moulds, but due to the significant error, it is hard to distinguish it;
- During fast cooling rates (in the water-cooled copper mould), higher shrinkage is observed in the Non-P 2 and Hypo-P samples compared to the slow cooling (graphite mould) during initial solidification;
- As the temperature gradient across and along the sample before the γ to α transformation is lower compared to the gradient after the sample solidifies, it allows observing of the volume change, associated with the γ to α transformation;
- The measured shrinkage values after the sample solidifies and before the γ to α transformation are lower than the predicted values by Thermo-Calc. This may be due to the formation of porosity during solidification;
- Shrinkage experiments are very delicate because there are many parameters, which can directly affect the solidification shrinkage values.

As for the initially stated hypothesis, the results show that the error between the experimental results is too large to be able to clearly interpret the solidification shrinkage in both non-peritectic and hypo-peritectic samples. However, a difference in the shrinkage results was observed between the slow and fast cooling conditions. Therefore, there might be a future potential to use this technique for solidification shrinkage measurements, but the casting conditions must be improved to avoid the formation of porosity and therefore increase the chances of getting accurate shrinkage results. In addition, the effect of the thermal gradient on the solidification shrinkage can also be further investigated because in the current research some trends were observed in the way the temperature gradients are varying depending on the steel composition.

An important observation of the localised remelting of the Hypo-P steel was made during solidification, which was not seen during solidification of the Non-P 2 sample. This observation will be analysed and discussed in the following Chapter.

Chapter 6 Combined Approach of Using CSLM and TIC to Interpret the Solidification Behaviour of Peritectic Steels

6.1 Introduction

The surface observations, which were made using IR thermography during the shrinkage experiments (section 5.3), show that the solidification of the Hypo-P steel was accompanied by a localised remelting phenomenon. In an attempt to prove that it is the remelting of steel during solidification, a series of experiments were conducted on the microscopic scale on the Non-P 2, Hypo-P and Hyper-P steels using CSLM. High cooling rates (up to 10 °C/s), comparable to that during the shrinkage experiments, were used during CSLM experiments.

As described in Chapter 2, the occurrence of the remelting of peritectic steel during solidification was previously reported and explained by several authors [21,30,73]. One of the explanations was that during solidification δ remelts partially in front of the γ formation due to the segregation of solute. This idea was suggested by Hillert [73] based on the isothermal model, but no experimental data was collected at that time for low carbon peritectic steel to prove it. Another two authors [30,40] have performed concentric solidification experiments in the CSLM to explain the remelting phenomena, but their conclusions were different from each other. Phelan et al. [21] proposed that δ remelts due to the heat release during formation of γ. However, Griesser et al. [30] suggested that the remelting of δ is not related to the heat transfer, but it is caused by the solute diffusion. Griesser et al. [30] concluded that the diffusion of carbon in iron is higher compared to the diffusion of iron atoms, leading to a partitioning process and causing remelting of δ, which occurs at a higher driving force (higher rate) than the solidification of the γ phase.

Despite disagreement on the reason behind the remelting of peritectic steels, all authors reported that peritectic steels always cause defect formation during the CC process. As summarised in Chapter 2, the defects can be associated with a large shrinkage, which occurs during the peritectic reaction, leading to formation of a large air gap between the steel and the copper

mould. It reduces the heat extraction from the molten metal and, as a result, leads to a thin solidified shell, which cracks due to the ferrostatic pressure.

As noted above, Phelan et al. [21] and Griesser et al. [30] were using the concentric solidification technique to describe the remelting phenomenon, but this technique only works if there is a large temperature gradient across the sample. It results in the forced segregation of the elements towards the centre of the sample, leading to formation of γ between liquid and δ. Without a large temperature gradient and excessive segregation, the solidification behaviour may be different from that described by Phelan et al. [21] and Griesser et al. [30]. Therefore, it is important to understand what exactly causes the defect formation during solidification and assess whether remelting indeed occurs in peritectic steels not only during concentric tests but also during bulk solidification of the sample.

In this Chapter, the evaluation of the heat extraction during solidification was carried out, which gives an insight into the solidification behaviour of peritectic steels. Traditionally this can be done using the DSC technique (described in Chapter 4). However, due to the restricted cooling rate of the DSC (which is maximum about 0.8 °C/s), an alternative method must be used to assess the released heat during rapid solidification of steel.

In a recently developed method by Slater et al. [69] it was shown that it is possible to obtain the information about the latent heat of fusion, seen during the solidification and phase transformation, by combining the IR thermography and CSLM techniques. As described in detail in Section 3.5, this combination resembles the DSC technique; however, it has been shown to be less constrained by heating and cooling rates. Therefore, it also gives information about the released heat during fast cooling rates (up to 10°C/s), which enhances the capability of the CSLM. In addition, it is capable of imaging the surface of the sample while doing the experiments in a good inert atmosphere. Thus, some transformations, which cannot be detected by the DSC, can be confirmed using the CSLM.

The cooling rate for the experiments used in the current research varies depending on the experimental setup. It is very slow during the DSC test – 0.5 °C/s due to the limitations of the equipment and other reasons previously described. The cooling rate varies during the CSLM test from 0.5 to 10 °C/s, and it is higher during the shrinkage test – between 50 to 100 °C/s. All these results can be correlated with the behaviour of the steel during continuous casting process at the different location inside the slab, because the cooling rate of the slab also varies from

1000 °C/s (at the steel shell closer to the copper mould) to 0.1 °C/s (close to the middle of the slab) as described in section 2.2.

The objectives and hypothesis to be investigated were explained in Chapter 1, but the parts relevant to this part of the study are:

1) To develop a new experimental technique based on the heat extraction idea during solidification of steels, which gives an understanding of the defect formation of peritectic steels during solidification

- It is hypothesised that due to the larger shrinkage during the early stages of solidification of peritectic steels, the heat extraction from the Hypo-P steels is lower compared to the Non-P steels.

2) To assess the difference in the solidification behaviour of the Non-P 2, Hypo-P and Hyper-P steels under rapid cooling rates using CSLM and explore on the microscopic scale if remelting of peritectic steel indeed occurs during solidification. Section 2.7.4 summarises the literature survey when remelting of peritectic steel was observed during concentric solidification, but it is also important to understand if the remelting occurs during bulk solidification. The localised remelting was observed in Chapter 5 during the shrinkage experiments, but it is important to understand if this phenomenon is also observed on the microscopic level.

- It is hypothesised that the Hypo-P steels are more prone to remelting during solidification, compared to the Non-P 2 and Hyper-P samples

6.2 The use of CSLM and IR thermography to evaluate the solidification of the Non-P 2 samples

A series of experiments were conducted for the Non-P 2 sample, which qualitatively indicates the heat conducted from the sample to the crucible during solidification. The data is taken from 8 pixels located on the crucible (C1-8), which are about 0.5mm away from the sample, as illustrated in Figure 3.17. (Section 3.5.2).

The radiated heat was measured from the crucible and not from the sample because the emissivity of the solidifying sample changes when liquid phase transforms to solid. In addition, it changes if there are any inclusions or oxides on the sample surface, which are also affected by the atmosphere [69]. However, the crucible always remains solid during the CSLM test, so

it does not undergo the emissivity change due to phase transformations, but it shows the difference in emitted heat as the temperature changes. Therefore in order to obtain much more reliable and consistent thermal readings, only the heat conducted from the sample to the crucible (much like a DSC) is considered, and not the heat, emitted by the sample. As mentioned in Section 3.5.2, to be able to measure the emitted heat from the crucible, the thermal imaging source must operate at frequencies higher than the frequency of the halogen bulb at the bottom of the CSLM furnace (higher than 2 μm).

The radiated heat of the Non-P 2 sample, measured by the IR camera during solidification at 1°C/s is illustrated in Figure 6.1 (a). The average values of 8 pixels and the measured temperature are shown in Figure 6.1 (b). A gradual reduction of the emitted heat is observed during cooling between 0 and 52 s. Then, at 53 s, the radiated heat starts to rise, which is consistent with the beginning of solidification. Based on the temperature measurements shown in Figure 6.1 (b), the solidification process starts at 1508°C at 1 °C/s cooling. For comparison, during the DSC test, at 0.5°C/s cooling (Chapter 4), the beginning of solidification was observed at 1506°C.

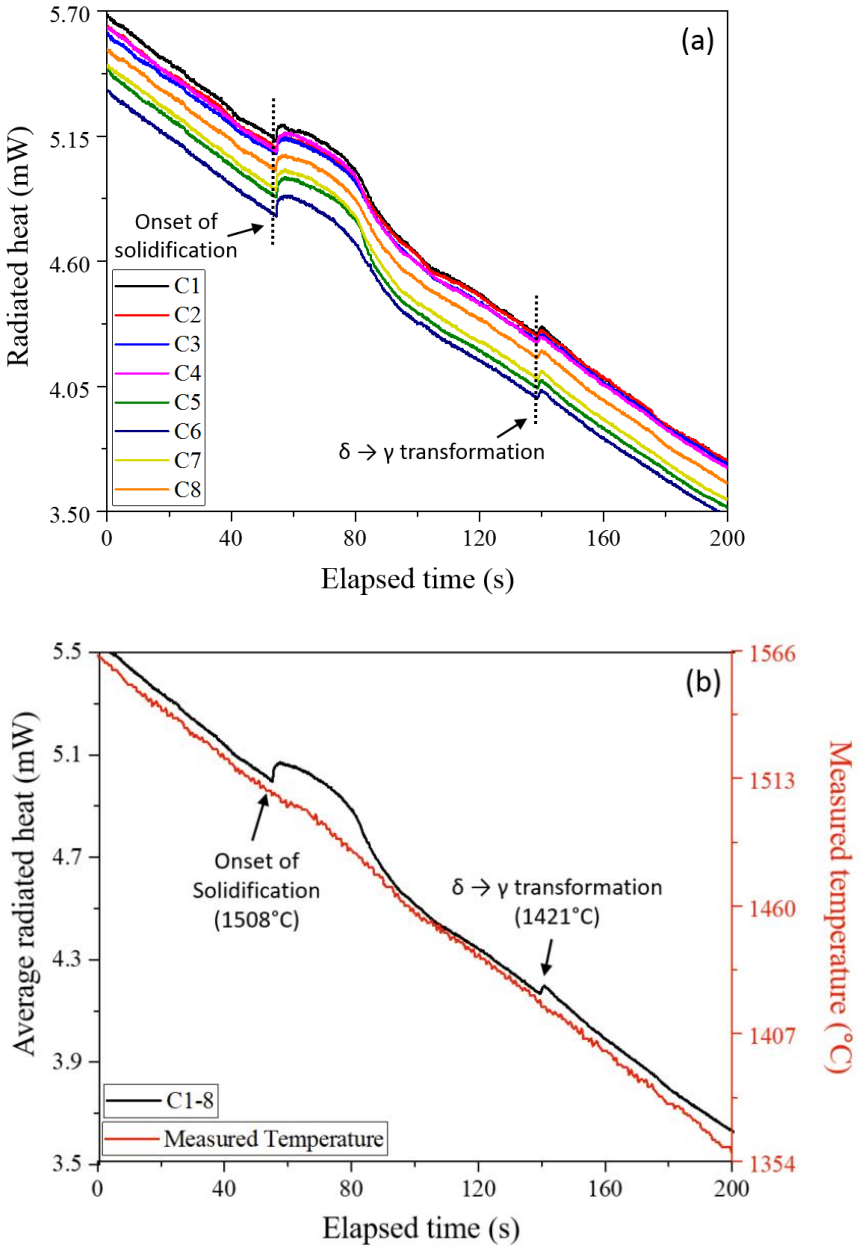

Figure 6.1 Radiated heat, measured by the IR camera during 1°C/s cooling of the Non-P 2 sample, taken from 8 pixels from the crucible around the sample (a), and temperature data, measured by the thermocouple, combined with the average values of the radiated heat, taken from 8 pixels (b)

It is difficult to accurately determine the end of solidification based on the radiated heat results because it requires the calibration procedures comparable to that used for the DSC (described in section 2.6.1), which is not available at this moment. When the sample approaches the end of solidification, the heat extraction decreases gradually. In addition to that, while the sample solidifies, it shrinks, so a gap is created between the sample and the crucible, which reduces the heat extraction even more. The higher the shrinkage of the sample during solidification, the less thermal information is collected during the test. Therefore, the solidus temperature is not

included in these analyses. At 139 s, another exothermic change in the emitted heat can be seen on the curve at around 1421°C. This peak is consistent with the δ to γ transformation, which was shown in Figure 4.5 (c-d) as surface relief in the CSLM imaging at 1405°C. The δ to γ transformation is accompanied by only 42 J/g of released energy, compared to the 258 J/g during solidification. This is a reason why the second peak shown in Figure 6.1 is much smaller, compared to the first peak [69].

Comparable solidification behaviour of low carbon steel between the DSC, CSLM and IR thermography has been previously confirmed by Slater et al. [69]. Therefore, the IR thermography and CSLM technique can be used to obtain a clear indication of the solidification process. However, unlike the DSC, currently it cannot be used to calculate the enthalpy of fusion, because the measurements need to include unknown data, like the balance of the heat lost from the sample surface and the heat conducted through the crucible [69].

It is also important to know the temperature range between the solidification onset and the δ → γ transformation because the higher undercooling for the δ → γ transformation, the larger the thermodynamic driving force for the phase transition and therefore the higher reaction and transformation kinetics [1]. This is subsequently accompanied by a negative effect on the steel quality during the CC process because of the rapid phase transformation, leading to a rapid volume decrease of the steel, creating an air gap between the steel shell and the copper mould, decreasing the heat extraction and causing stress formation in the region where rapid shrinkage occurred.

For the Non-P 2 sample, the temperature difference between the solidification onset and the δ → γ transformation is 87°C, which is 12°C more than the equilibrium value calculated by Thermo-Calc, as shown in Figure 6.2. The comparison of the temperature range between the steel samples will be described later in this Chapter.

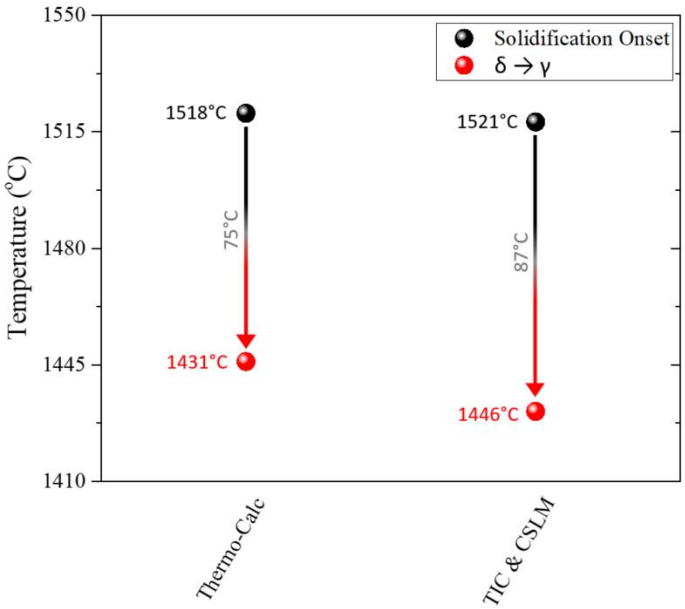

Figure 6.2 Temperature difference between solidification onset and δ to γ transformation in the Non-P 2, calculated by Thermo-Calc and measured during TIC and CSLM experiments at cooling rate of 1°C/s

The solidification behaviour of the Non-P 2 sample was also observed at a faster cooling rate of 10°C/s (which is currently not available in commercial calorimetry equipment, as mentioned above). The radiated heat from the Non-P 2 steel is illustrated in Figure 6.3. By comparing slow (1°C/s) and fast (10°C/s) coolings (Figure 6.1 and Figure 6.3, respectively), it can be seen that at 10°C/s the solidification starts at around 1518°C, which is 10°C higher compared to the solidification onset at 1°C/s. However, the undercooling temperature is expected to be higher at higher cooling rates, but this can be explained by two phenomena, which must take place in the liquid phase for the solidification to occur: undercooling and nucleation. When both conditions are met, the nuclei start to grow into a solid grain until the sample fully solidifies [100]. The microstructural analysis of the samples, which solidified during the CSLM or DSC tests shows that the whole sample (about 130 mg) has only about 5-10 grains. The small amount of grains formed during solidification means that there were fewer chances of the nucleation of γ for the δ → γ phase transformation to occur. Therefore, nucleation has a strong influence on the solidification process. As it is a statistical parameter, which cannot be controlled during these experiments, then this is a reason why the measured solidification temperature is not the same as predicted.

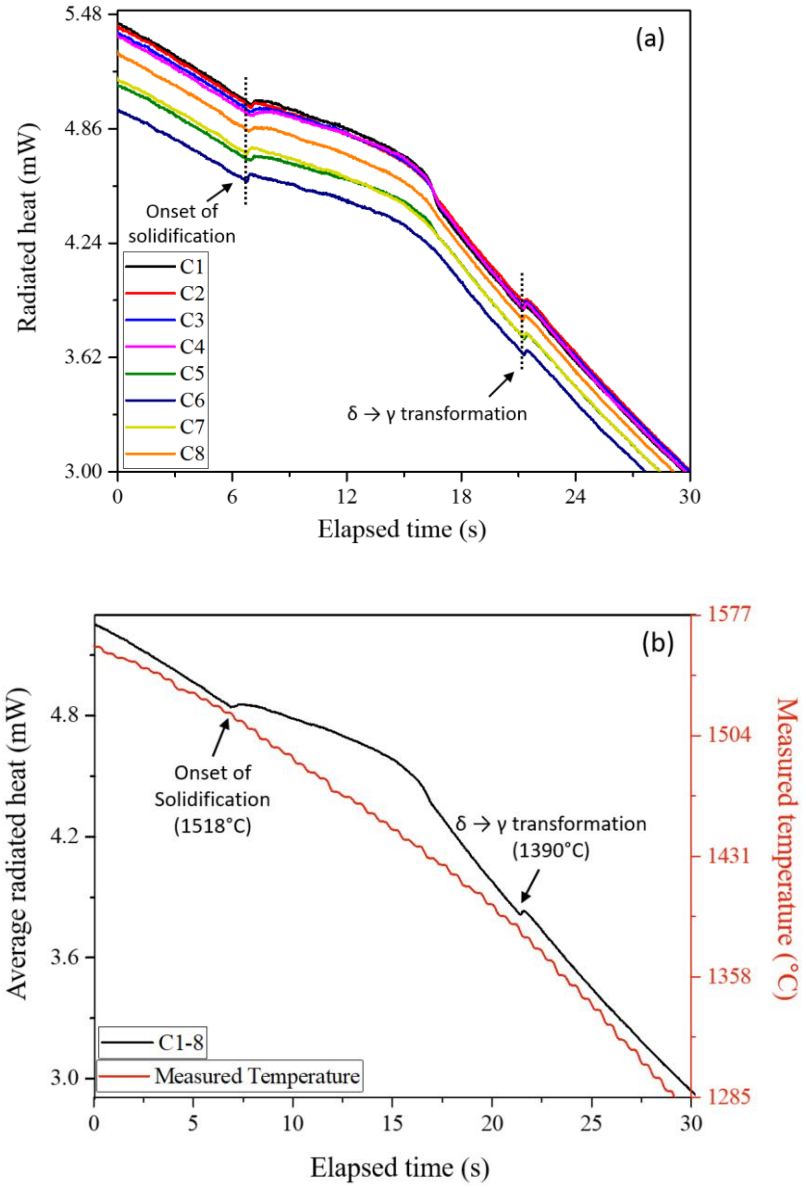

Figure 6.3 Radiated heat, measured by the IR camera at 10°C/s cooling of the Non-P 2 sample, taken from 8 pixels from the crucible around the sample (a), and temperature data, measured by the thermocouple, combined with the average values of the radiated heat, taken from 8 pixels (b)

At higher cooling rates it is even more difficult to understand when the solidification process finishes based on the radiated heat curve, although the δ to γ transformation is clearly observed at 1390°C as a small heat increase. The temperature difference between the beginning of the solidification and the δ to γ transformation is 128°C, which is 53°C more than the equilibrium value. As predicted, by increasing the cooling rate, the undercooling temperature for the δ to γ transformation increases, as illustrated in Figure 6.4. Therefore, this technique can be used to study the effect of the cooling rate on the undercooling temperature for the δ → γ phase transformation, because the earlier this transformation occurs during CC process, the higher the shrinkage of steel will be, which may eventually influence the quality of steel.

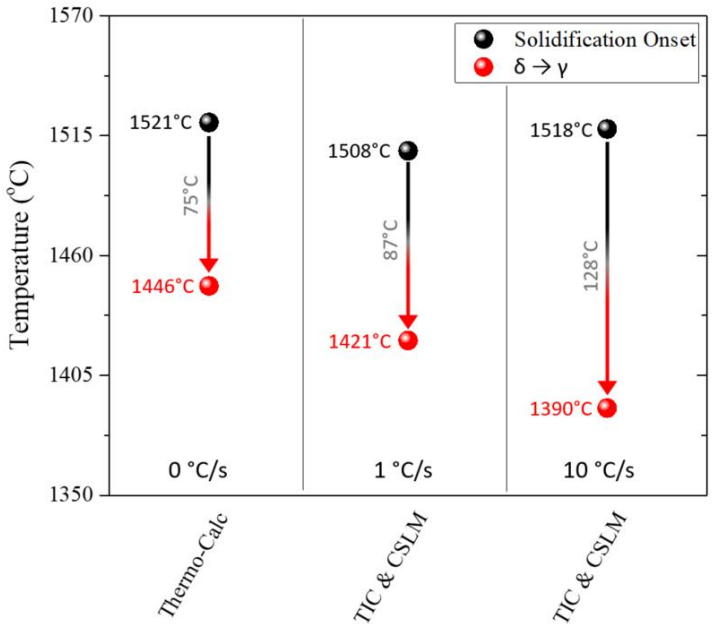

Figure 6.4 The effect of cooling rate on the temperature difference between solidification onset and δ to γ transformation in the Non-P 2 sample, calculated by Thermo-Calc (0°C/s) and measured during TIC and CSLM experiments at 1°C/s and 10°C/s

The microscopy observations of the Non-P 2 sample are also conducted at 10°C/s cooling. The CSLM images, depicted in Figure 6.5 (a), illustrate the first solid phase (δ) that appears on the top surface of the molten droplet at 1432°C. The emitted IR heat shows the temperature increase as soon as the sample starts to solidify subsurface (Figure 6.3), which cannot be observed on the top surface of the CSLM image until the dendrites reach that area. However, when the sample starts to solidify subsurface in the CSLM, the noticeable convection change can be seen on the surface, which is also confirmed by Slater et al. [69]. Nevertheless, the emitted IR heat during solidification of the sample can indicate earlier the onset temperature of the sample solidification, then it is seen on the surface of the CSLM image. This explains why the onset of solidification during the CSLM imaging test is 86°C lower compared to that indicated in the radiated heat.

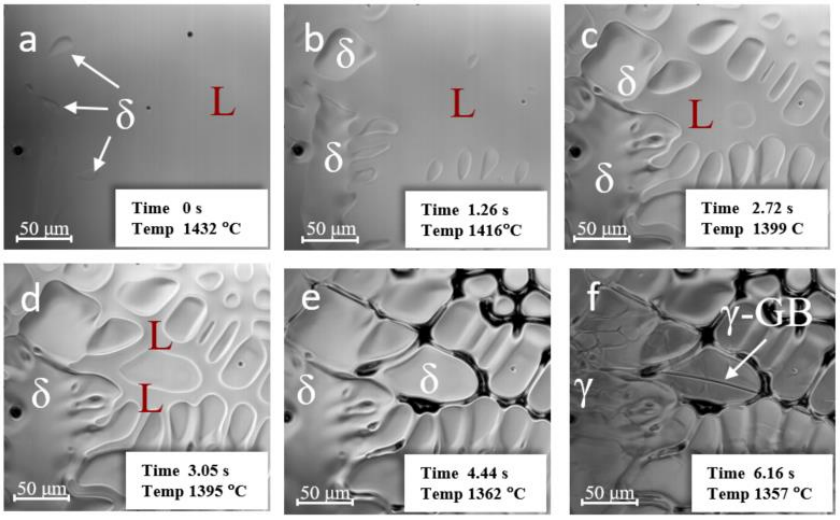

Figure 6.5 Solidification of the Non-P 2 sample using CSLM at a cooling rate of 10°C/s

Upon further cooling, the dendrite arms, illustrated in Figure 6.5 (b to d) grow and coarsen, until the sample fully solidifies at 1362°C (Figure 6.5 e). The δ to γ transformation is then observed on the sample surface at 1357°C (Figure 6.5 f).

6.3 The use of CSLM and IR thermography to evaluate the solidification of the Hypo-P samples

The IR thermography curves for the Hypo-P sample (Figure 6.6 a, b) illustrate that at 1°C/s cooling the solidification starts at 1524°C. Unlike in the Non-P 2 sample, the Hypo-P sample shows non-uniform heat extraction, which can be seen as heat fluctuations while the sample solidifies, as illustrated in the C1, C2, C3 and C8 curves in Figure 6.6 (a). These results are explained in more detail at the end of this Chapter.

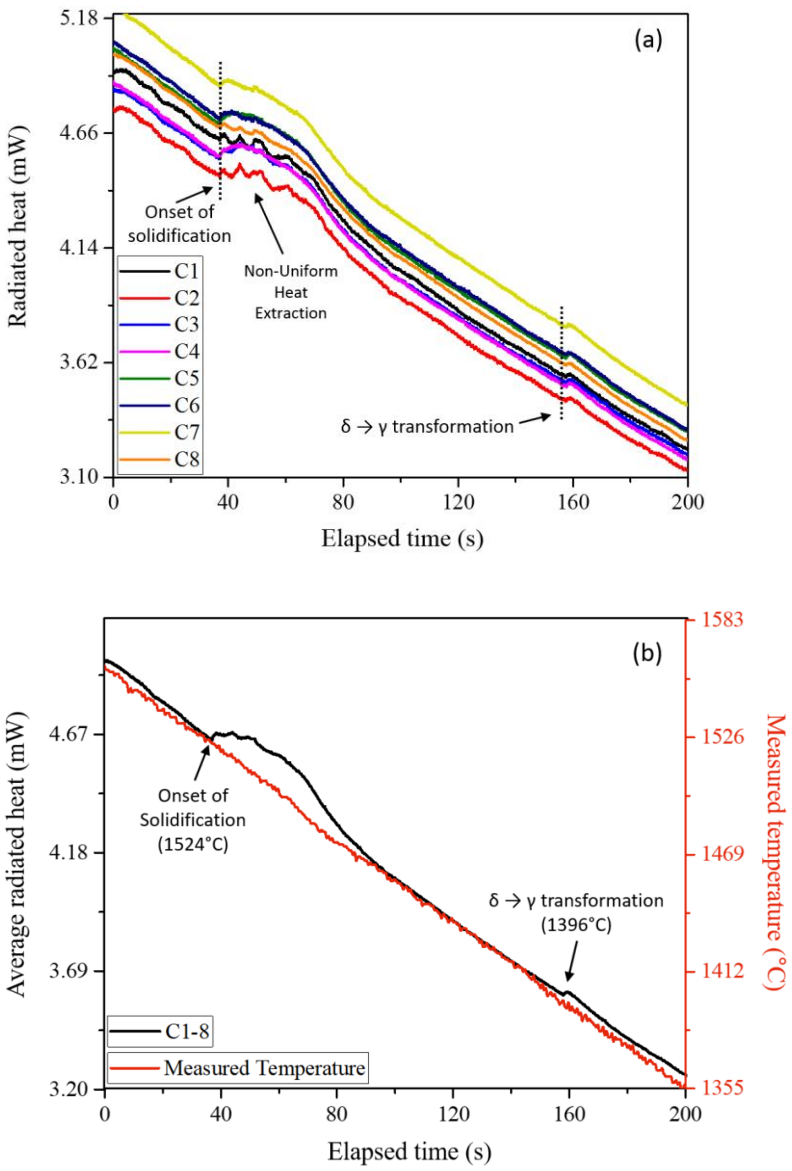

Figure 6.6 Radiated heat, measured by the IR camera during 1°C/s cooling of the Hypo-P sample, taken from 8 pixels from the crucible around the sample (a), and temperature data, measured by the thermocouple, combined with the average values of the radiated heat, taken from 8 pixels (b)

Upon further cooling of the Hypo-P sample, the δ to γ phase transformation is measured at 1396°C (Figure 6.7). So in the Hypo-P sample, the measured temperature range between solidification onset until the δ → γ transformation is 66°C larger, compared to the equilibrium value, whereas in the Non-P 2 sample the difference was only 12°C (Figure 6.4) for the same cooling rate. This is an important observation because knowing the effect of the cooling rate on the undercooling temperature of the phase transformation can help adjust the cooling conditions during the CC process and improve the steel quality. Therefore, this technique can be used to understand better the phase transformation behaviour of the steels, especially those, which are sensitive to defect formation during solidification.

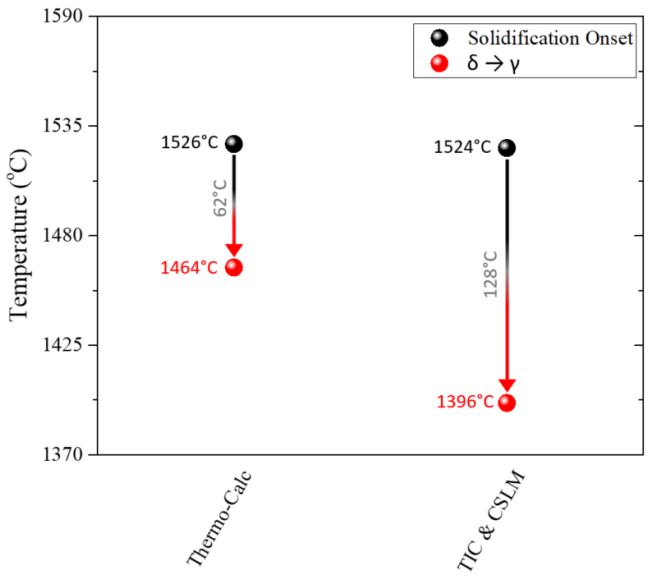

Figure 6.7 Temperature difference between solidification onset and δ to γ transformation in the Hypo-P sample, calculated by Thermo-Calc and measured during TIC and CSLM experiment at 1°C/s

At a higher cooling rate of 10°C/s, uneven heat extraction was also observed during solidification of the Hypo-P sample. As shown in Figure 6.8 (a), after the solidification onset at 1512°C, the C1 and C8 curves have lower heat extraction, compared to the C3, C4, C5 curves, and the curve called C2 shows small fluctuations during the sample solidification. Another important observation is that the peak for the δ to γ transformation was not observed after the sample solidified. The radiated heat data was checked until about 1000°C, and there were no peaks observed for the δ to γ transformation. The uneven heat extraction and the absence of the peak for the δ to γ transformation will be discussed in detail at the end of this Chapter.

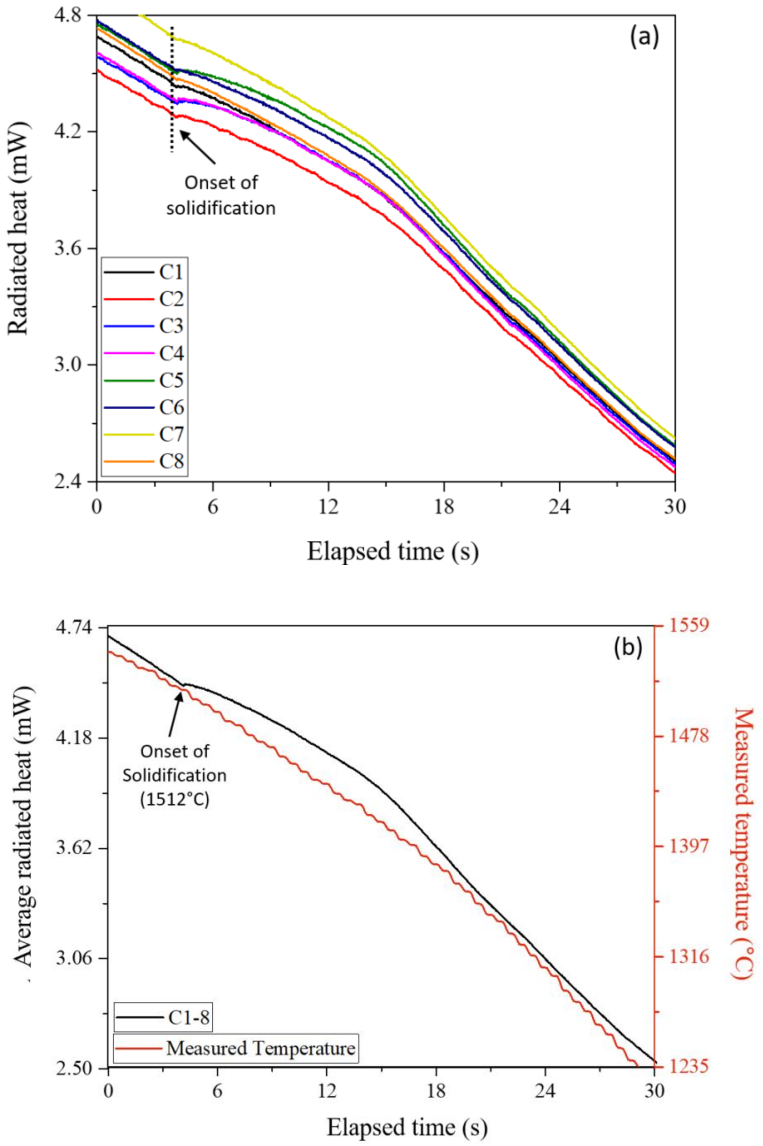

Figure 6.8 Radiated heat, measured by the IR camera at 10°C/s cooling of the Hypo-P sample, taken from 8 pixels from the crucible around the sample (a), and temperature data, measured by the thermocouple, combined with the average values of the radiated heat, taken from 8 pixels (b)

To understand the reason for the fluctuations in the radiated heat, the CSLM images were recorded during the test at 10°C/s cooling, as illustrated in Figure 6.9. The CSLM results show that the dendrites appear on the surface at around 1486°C, followed by dendrite growth (Figure 6.9 a, b). However, a moment after that, some of the dendrites start to decrease in size or re-melt (completely disappear from the top surface of the sample) after they partially solidified. Seven areas, where these events occur, are highlighted in Figure 6.9 (b-i) in the dashed circles. The white circles illustrate the area where the remelting starts, the yellow – is where the size of the solidified dendrite decreases, and the red – is where the dendrite completely disappears from the surface of the sample. It should be noted that not only small dendrites re-melt but also large

dendrites re-melt after they partially solidified, as shown as dendrite number 2 in Figure 6.9 (c – f). Even though it is larger, compared to the one above it, nevertheless, it re-melts and completely disappears from the surface, as shown in Figure 6.9 (f).

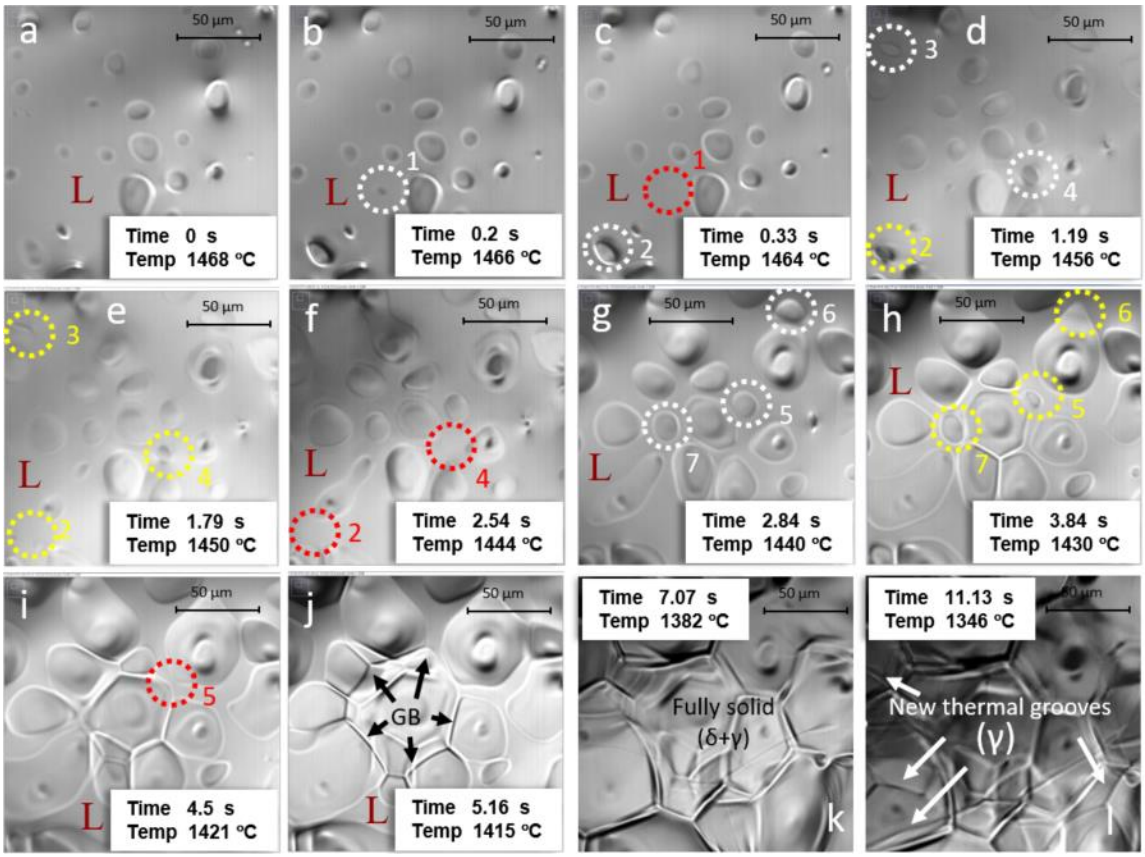

Figure 6.9 Remelting of the Hypo-P sample during solidification using CSLM at 10 °C/s cooling

Upon further cooling, the Hypo-P sample fully solidifies at 1382°C to form a combination of two phases – δ and γ. At 1346°C, a rapid transformation on the sample surface is observed, and new thermal grooves appeared on the sample. Based on the previous observations, described in Chapter 4, this indicates the δ → γ transformation, which is associated with sample shrinkage as γ is denser than δ.

The remelting of the Hypo-P sample was also observed at 0.5°C/s, which is illustrated in Figure 6.10. The solidification starts at 1501°C, following by dendrites remelting until the sample fully solidifies at 1490°C.

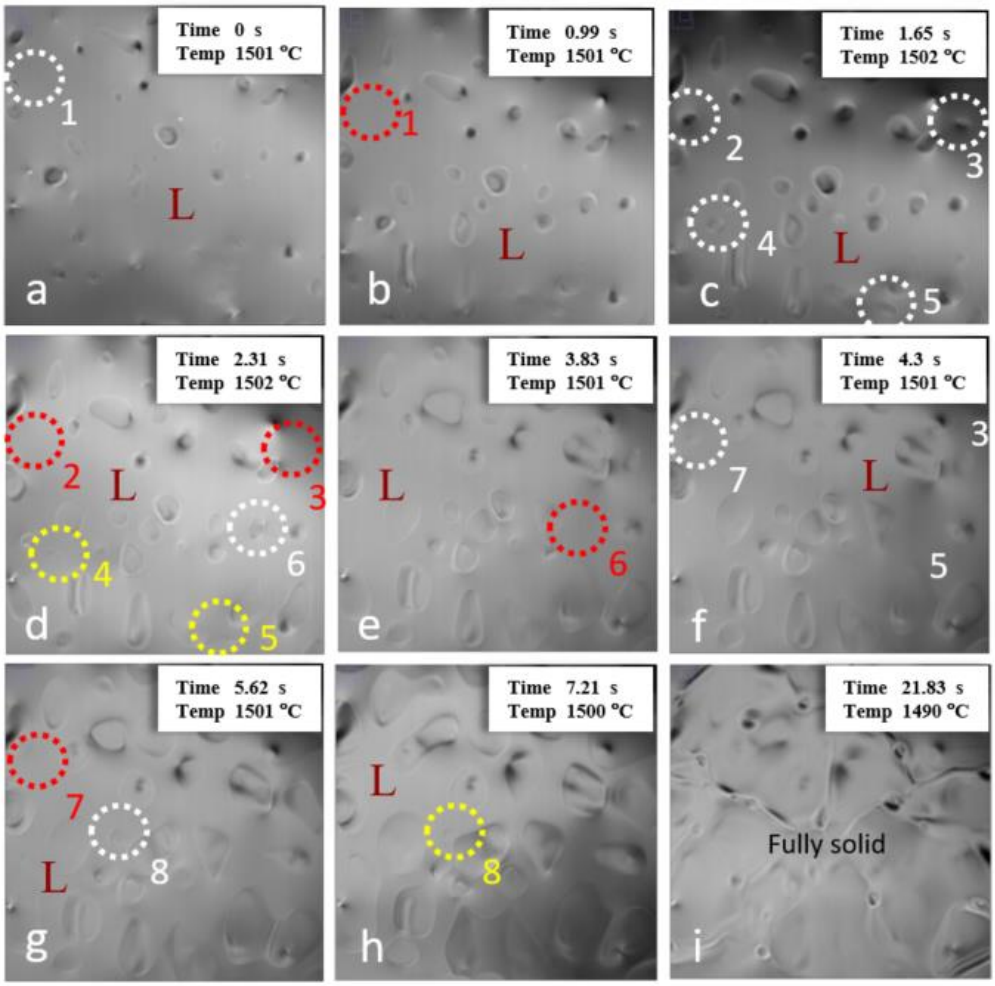

Figure 6.10 Remelting of the Hypo-P sample during solidification using CSLM at 0.5 °C/s cooling rate.

This section revealed interesting observations of the solidification phenomena of the Hypo-P samples, which were conducted using a combination of IR thermography and CSLM. It also proved the idea, proposed in Chapter 5, that the Hypo-P steels undergo localised remelting during constant cooling.

6.4 The use of CSLM and IR thermography to evaluate the solidification of the Hyper-P samples

After the remelting phenomena were observed in the Hypo-P samples, it was interesting to check, if the Hyper-P sample has a comparable behaviour during solidification. Figure 6.11 illustrates the radiated heat, released from the sample to the crucible during 1°C/s cooling of the Hyper-P sample. It can be seen, that after the sample starts to solidify at 1499°C, all 8 cooling curves behave similarly without any heat fluctuations (Figure 6.11).

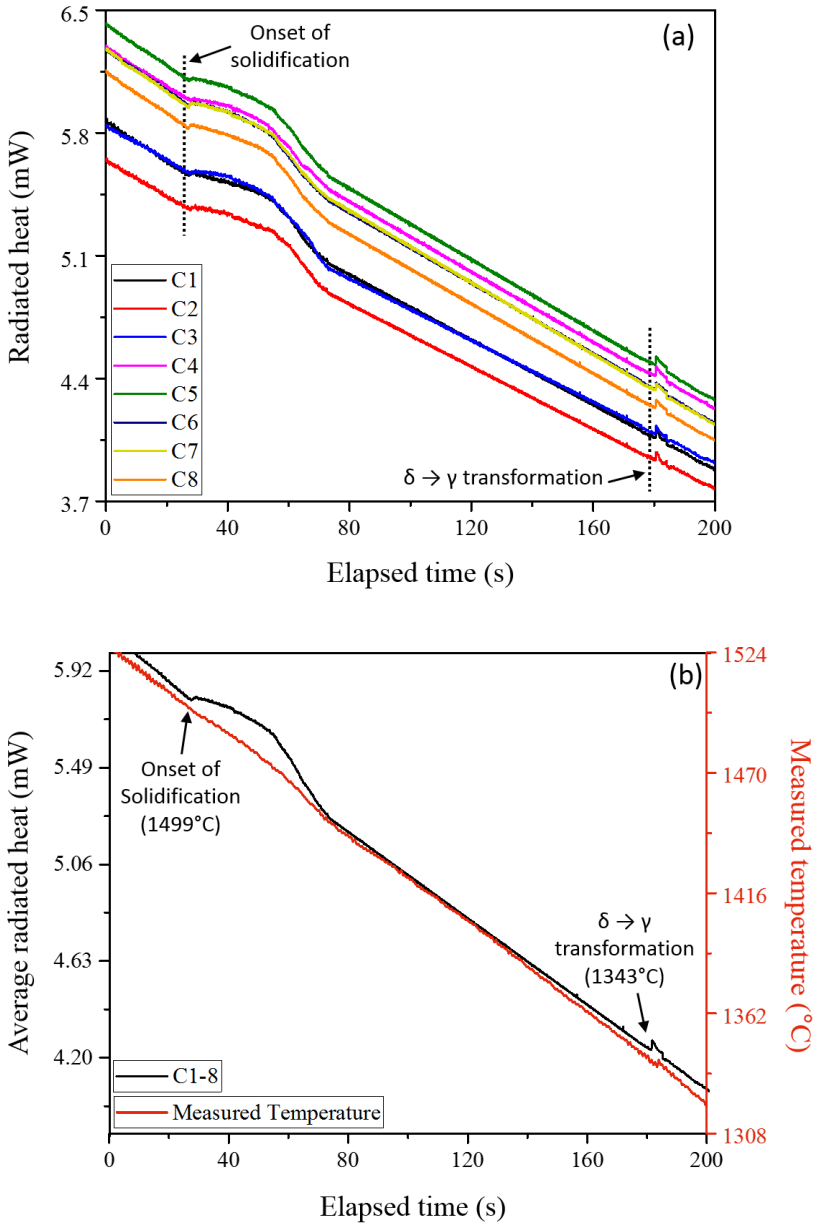

Figure 6.11 Radiated heat, measured by the IR camera during 1°C/s cooling of the Hyper-P sample, taken from 8 pixels from the crucible around the sample (a), and temperature data, measured by the thermocouple, combined with the average values of the radiated heat, taken from 8 pixels (b)

Upon further cooling, the peak for the δ → γ transformation is indicated on the curves at 1343°C. As illustrated in Figure 6.12, the measured temperature difference between the solidification onset and the δ → γ transformation is 113°C, compared to the calculated one.

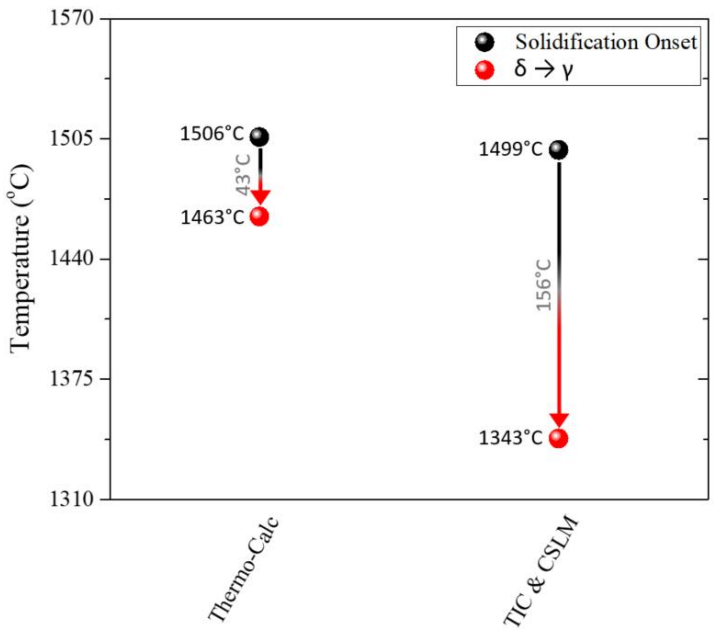

Figure 6.12 Temperature difference between solidification onset and δ to γ transformation in the Hyper-P sample, calculated by Thermo-Calc and measured during TIC and CSLM experiments at 1°C/s cooling rate.

The undercooling temperature difference is much larger in the Hyper-P sample (113°C) than in the Hypo-P (66°C) and Non-P 2 (12°C) samples (Figure 6.13). The explanation for the large undercooling temperatures for the δ → γ transformation is suggested in section 4.5, where comparable behaviour was observed in the Hypo-P sample at a slow cooling rate of 0.5°C/s. It was proposed that during solidification, gamma is formed around the solute depleted δ dendrite core. As diffusion through γ is slower than diffusion through δ, then the δ dendrite core transforms to γ only when δ is undercooled below the temperature of its existence. The fact that the Hyper-P shows a very large undercooling temperature supports the idea suggested in section 4.5, because the layer of γ around depleted δ is about 40% larger in the Hyper-P sample, compared to the Hypo-P one, which makes it more difficult for the carbon to diffuse through it.

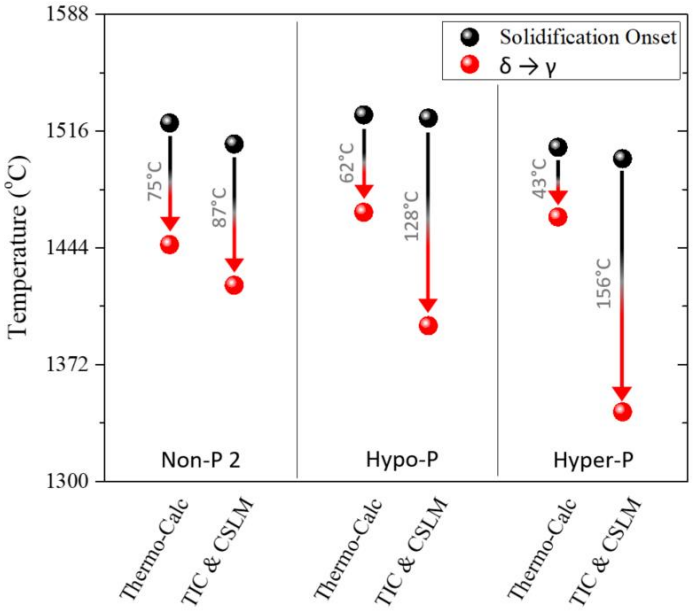

Figure 6.13 Temperature difference between solidification onset and the δ to γ transformation in the Non-P 2, Hypo-P and Hyper-P samples, calculated by Thermo-Calc and measured during TIC and CSLM experiments at 1°C/s cooling rate.

As described before, large undercooling for the δ → γ transformation has a negative effect on the steel quality during solidification. Very large undercooling can lead to the massive δ → γ transformation and rapid volume decrease of the steel shell, which creates stresses at the steel shell during the CC process and can lead to the defect formation. As summarised in Figure 6.13, the steels, which are more sensitive to defect formation during the CC process, have the largest temperature difference between equilibrium and measured data. Therefore, combining the IR thermography and CSLM techniques helps to understand the solidification and phase transformation behaviour of steels better, which can subsequently help to improve the steel quality during the CC process.

At the faster cooling rate of 10°C/s (Figure 6.14), the beginning of solidification of the Hyper-P sample is observed at 1478°C, but the peak for the δ → γ transformation is also not detected, similarly to the Hypo-P sample at 10°C/s cooling rate (Figure 6.14).

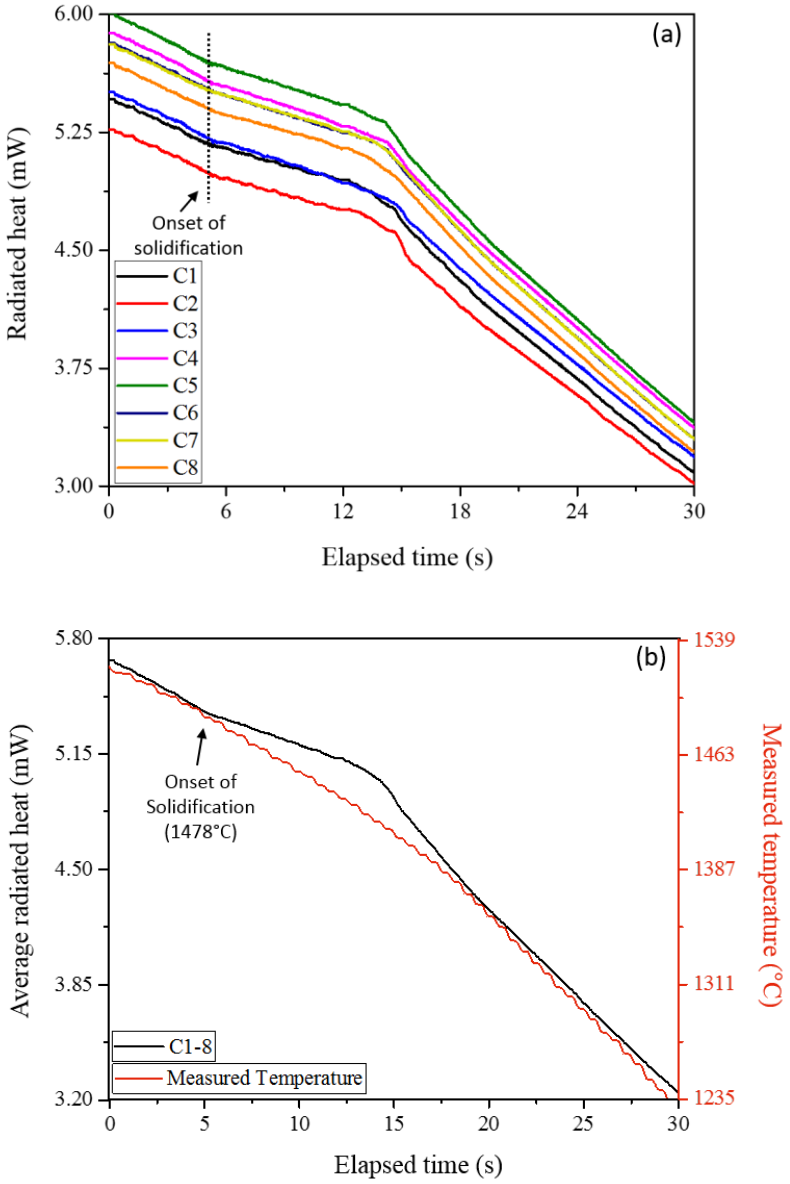

Figure 6.14 Radiated heat, measured by the IR camera during 10°C/s cooling of the Hyper-P sample, taken from 8 pixels from the crucible around the sample (a), and temperature data, measured by the thermocouple, combined with the average values of the radiated heat, taken from 8 pixels (b)

CSLM images of the Hyper-P sample (Figure 6.15) show that solidification starts at 1473°C and finishes at 1433°C. During this period, none of the dendrites was re-melted, and even the smallest dendrites solidified and remained on the sample surface. The δ → γ transformation was then observed at 1376°C. The black background in Figure 6.15e-f is the area where the last liquid solidified, This area is segregated with the elements which have low solubility in δ, and this area between the dendrites can lead to the γ formation, which has lower density than δ,

which can be the reason why the black background appears to have higher shrinkage compared to the grey region of δ dendrites.

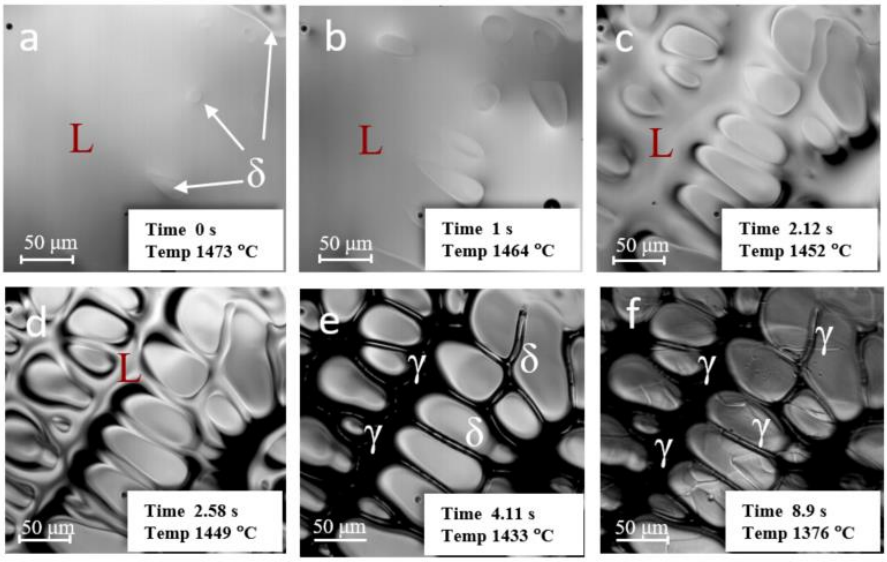

Figure 6.15 Solidification of the Hyper-P sample using CSLM at a cooling rate of 10°C/s

To draw a visual comparison of the heat extraction during solidification of all the steel samples described in this chapter, the radiated heat results for all 8 pixels (C1-C8) were normalised and colour-coded according to the scale on the right edge of each image as illustrated in Figure 6.16 and Figure 6.18. The radiated heat data was only magnified in the region, where solidification occurs. The blue colour means that there is no exo- or endothermic reaction while the steel is liquid (or solid). When the blue colour changes to the white, yellow or red (as depicted in the upper part of the colour bar) it means that the heat extraction increases as a result of an exothermic reaction during solidification (or phase transformation). When the colour map changes back to the blue colour, it means that the solidification process has finished.

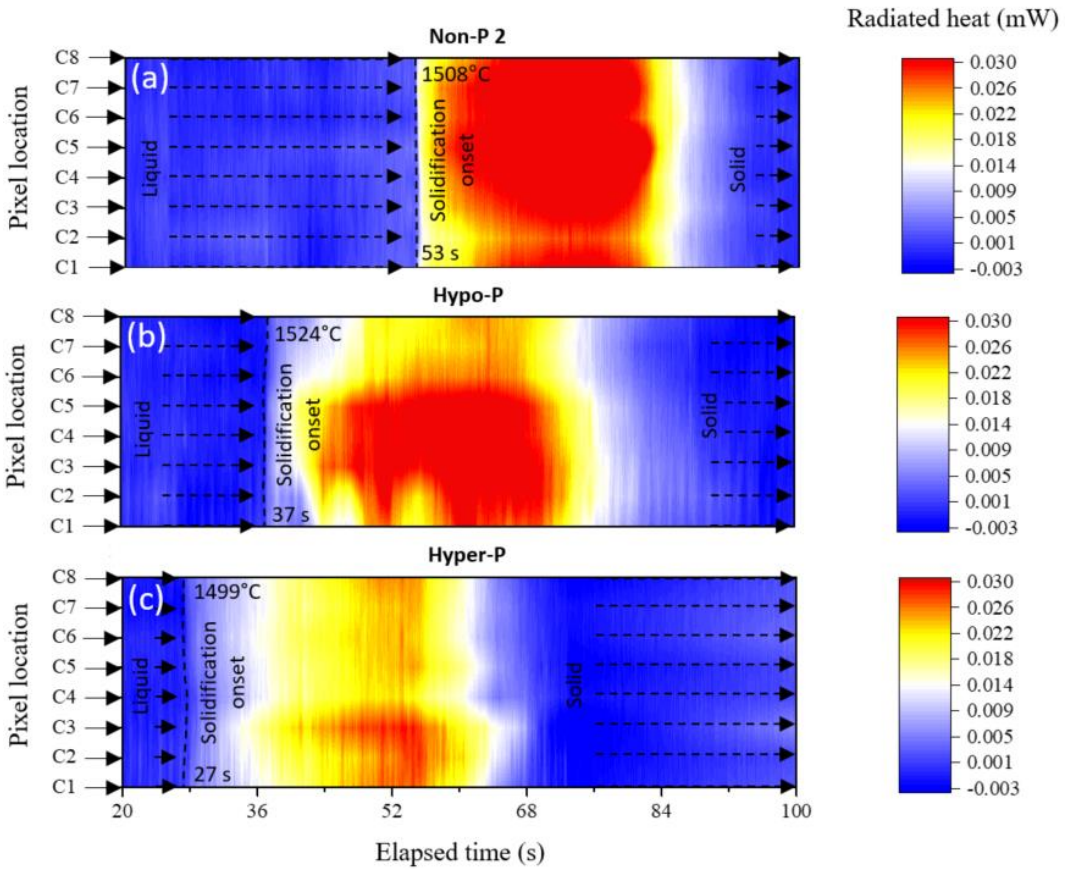

Figure 6.16 Normalised and colour-coded radiated heat results for the Non-P 2, Hypo-P and Hyper-P samples measured at a cooling rate of 1°C/s

Figure 6.16 illustrates that in the Non-P 2 sample the radiated heat starts to rise at 53s (1508°C) in all locations around the sample (from C1 to C8). The solidification also finishes at the same time in all 8-pixel locations, which indicates uniform heat extraction during the solidification process.

This is not the case for the Hypo-P sample, where non-uniform heat extraction and heat fluctuations are observed. After the solidification begins at 37 s (1524°C), the highest heat extraction is observed in the pixel locations C4 – C5; the lowest extraction is in C6 – C7 and the fluctuations of heat are observed in C1 – C3 and C8. This was also illustrated before in Figure 6.6 (a). One of the explanations for this solidification behaviour is suggested below and illustrated in Figure 6.17.

As explained above in this section and section Figure 4.5, when a δ dendrite solidifies, γ forms around the δ due to the segregation, which is illustrated as a dark grey δ dendrite core and a white γ layer around it in Figure 6.17 (b). It is proposed that the dendrites, which started to grow close to the C3 – C5 location have higher preferential growth compared to other areas, that is

why they are larger, whereas those, which grow closer to C6 – C7, are smaller as the heat extraction is less in that region. While δ dendrites are growing, C and Mn segregate not only around the dendrites to form γ but also in front of the solidifying δ, leading to the formation of a segregated area of C and Mn on the opposite side of the sample (closer to the C1 – C2 areas). This leads to the formation of the peritectic reaction, which occurs when 90% of δ solidifies. This reaction causes rapid release of heat and shrinkage because γ is denser compared to δ. This shrinkage creates a gap between the sample and the crucible and decreases the heat extraction. In addition, the heat caused by a peritectic reaction and reduced heat extraction causes the remelting of δ because the temperature of δ at that moment of the peritectic reaction is close to the solidus temperature and the heat, absorbed by δ after the peritectic reaction transforms it back to liquid. The occurrence of the remelting of the Hypo-P sample is also illustrated in Figure 6.9 and Figure 6.10. This is accompanied with heat fluctuations, which are clearly shown in C1 – C3 and C8 in Figure 6.16 (b) and Figure 6.6 (a).

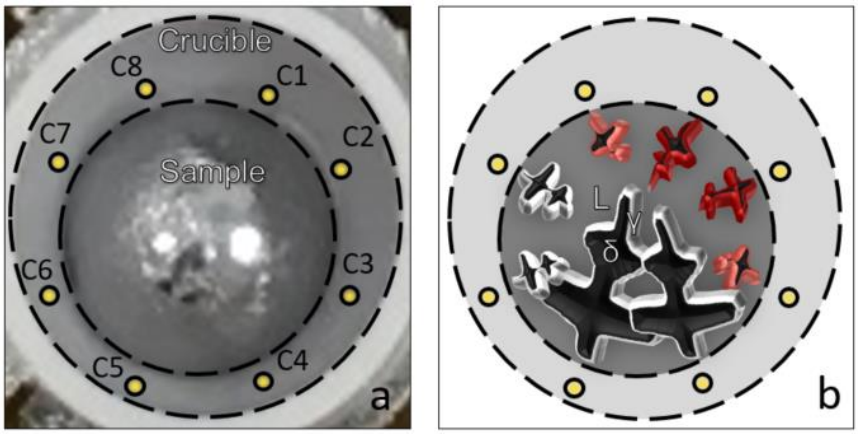

Figure 6.17 Simplified graphical illustration of the solidification process of the Hypo-P sample during TIC and CSLM techniques. Dark grey regions illustrate δ dendrite core, white regions – γ and red – areas of remelting of δ dendrites caused by a peritectic reaction

The solidification of the Hyper-P sample starts at 27s (1499°C) and shows the lowest heat extraction compared to other grades (Figure 6.16). Based on the Thermo-Calc calculations (Section 3.5.1), γ phase starts to form when 50% of the δ solidifies, whereas in the Hyper-P sample γ forms when about 90% of the δ solidifies. Therefore, the shrinkage caused by the γ formation in the Hyper-P sample occurs in the earlier stages of solidification, compared to the Hypo-P sample, leading to a low heat extraction, as depicted in Figure 6.16 (c).

Figure 6.18 illustrates the colour-map of the solidification of the Non-P 2, Hypo-P and Hyper-P samples at 10°C/s. The solidification of the Non-P 2 sample (Figure 6.18 (a)) starts at 7s

(1518°C), followed by a δ → γ transformation at 21s (1390°C) just after the sample solidifies. The solidification pattern of the Non-P 2 sample is uniform around the sample in all 8 locations.

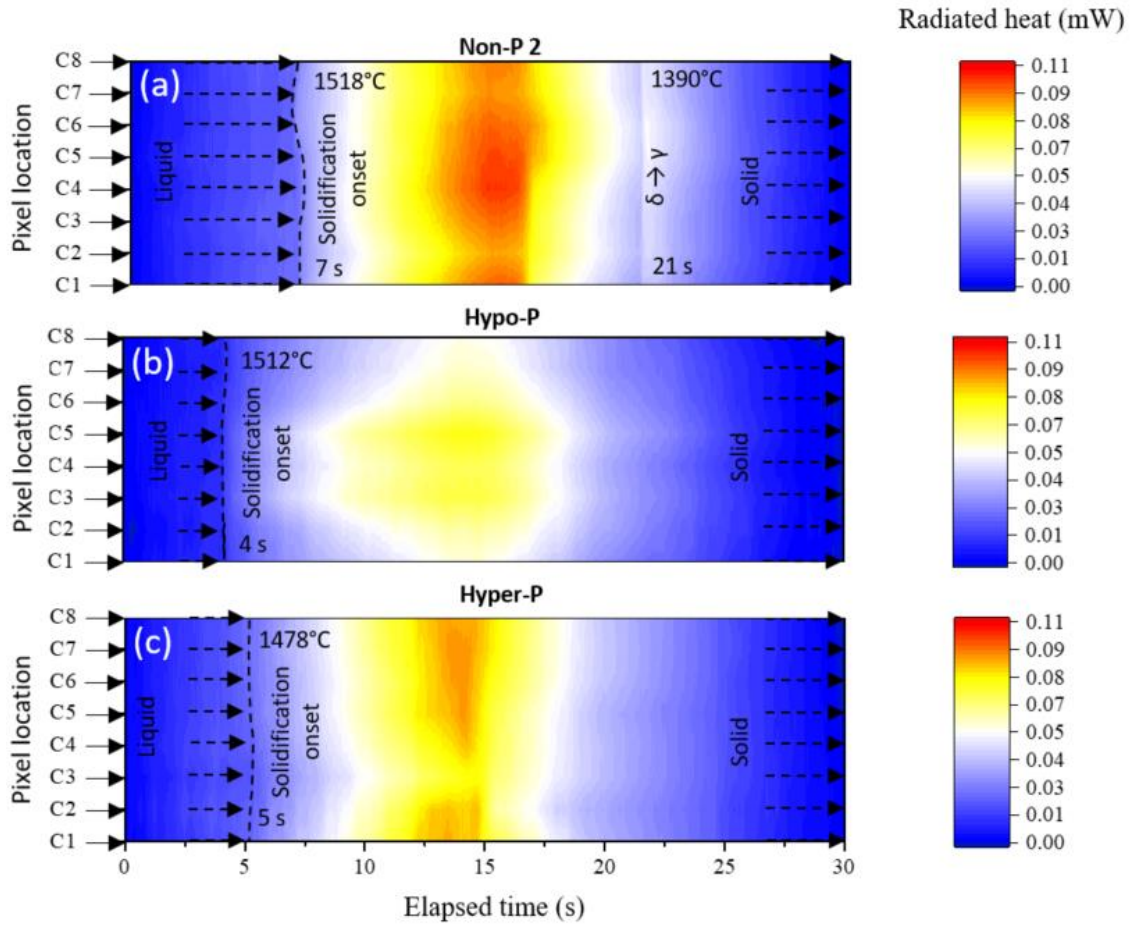

Figure 6.18 Normalised and colour-coded radiated heat results for the Non-P 2, Hypo-P and Hyper-P samples measured at a cooling rate of 10°C/s

The solidification of the Hypo-P sample starts at 4s (1512°C), and it shows non-uniform heat extraction, which is lowest in the C1, C7 and C8 locations, and higher on the opposite side of the sample at the C3 – C5 locations (Figure 6.18 (b)). The idea, proposed above is also applicable to this solidification pattern. It is suggested that the preferential growth of the dendrites occurs on one side of the sample, leading to the segregation, peritectic reaction and subsequent remelting at the opposite side of the sample, this is why heat extraction varies across the sample.

The solidification of the Hyper-P sample starts at 5s (1478°C) as shown in Figure 6.18 (c). The heat extraction is also higher on one side of the sample (C6 – C8) and lowest on the opposite side (C3). This solidification behaviour is relevant to all samples described in this Chapter, but

it is more vivid in those samples which undergo a peritectic reaction during solidification because of the shrinkage formation in that region.

As shown previously in this Chapter, the peak for the $\delta \rightarrow \gamma$ transformation was not observed in the Hypo-P and Hyper-P samples at a cooling rate of 10°C/s. One of the explanations is that the radiated heat during the $\delta \rightarrow \gamma$ transformation was much less than the radiated heat caused by the solidification, so the $\delta \rightarrow \gamma$ peak does not stand out in the results. Another explanation is that the shrinkage of the Hypo-P and Hyper-P samples is high during solidification and the conduction of the heat caused by a $\delta \rightarrow \gamma$ transformation is therefore low towards the crucible, so the Thermal Imaging Camera is not sensitive enough to pick up this difference in the radiated heat.

6.5 Summary and Conclusions

A combined IR thermography and CSLM technique was implemented for the current study to evaluate the solidification behaviour of the Non-P 2, Hypo-P and Hyper-P samples. The following conclusions can be drawn based on the experimental results:

- A combination of the IR thermography and CSLM technique can be used to obtain a clear indication of the solidification process.

- For the Non-P 2 samples, at a cooling rate of 1°C/s the measured temperature values between the solidification onset and the $\delta \rightarrow \gamma$ transformation is 12°C, but for the Hypo-P and Hyper-P samples the values are 66°C and 113°C respectively. The formation of a γ layer around a solute poor dendrite core during solidification explains the reason for a high undercooling temperature for the $\delta \rightarrow \gamma$ transformation because it does not allow for the segregated elements to diffuse back to the δ.

- High undercooling temperatures between the solidification onset and $\delta \rightarrow \gamma$ transformation for the Hypo-P and Hyper-P samples can lead to high reaction and transformation kinetics and can be a reason for the defect formation during the CC process of these grades. Combining IR thermography and CSLM techniques help to understand the effect of the cooling rate on the undercooling temperature of the phase transformation and subsequently improve the steel quality

- Non-uniform heat extraction was observed during solidification of the Hypo-P samples, which correlates well with the remelting of the solidified dendrites of the Hypo-P sample observed during CSLM tests.
- The reason for remelting of the δ dendrites is explained as a combination of several events, which occur one after another. It starts from the peritectic reaction, which leads to exothermic heat and shrinkage of the steel, causing the reduction of the heat extraction and leading to the remelting of the solidified δ dendrites.
- The remelting phenomena were only observed in the Hypo-P steels, both during high (10°C/s) and slow (1°C/s) cooling rates, but not in the Non-P 2 or Hyper-P samples.

Chapter 7 Conclusions and Further Work

7.1 Conclusions

The demands for the production of steels, close to the peritectic region in composition, has been increasing, especially for the automotive industry, mainly to reduce the mass of the vehicles and achieve excellent mechanical properties as well as cost reduction. However, the solidification of peritectic steels during continuous casting often leads to defect formation, such as deeper oscillation marks, longitudinal cracks and even breakouts. The fundamental reason for the defect formation remains incompletely understood, even though based on the literature review it has been extensively studied. To decrease the defect generation, casting of peritectic steels is usually performed at reduced casting speeds, leading to a negative influence on plant productivity.

An attempt was made in the current research to find a detailed explanation of the reason for the defect formation during solidification of peritectic steels. The assessment of the solidification behaviour of steels was made on commercial steel grades, one of which is a peritectic grade (Fe-0.11wt.%C) and another a non-peritectic grade (Fe-0.042wt.%C). By combining different experimental techniques, it was found that the solidification behaviour in industrial peritectic steels is different from that in non-peritectic steels. The main experimental results are summarised in the statements below.

1) Based on the theoretical values, which have been produced using thermodynamic software such as Thermo-Calc, it was found that the solidification behaviour of industrial peritectic and non-peritectic steels used in the current research is different. Peritectic steels show a thirteen degrees broader mushy zone, 0.2% larger shrinkage formation and 6% more heat release compared to non-peritectic steels.

2) During heating, the peritectic behaviour in steels is clearly determined based on the DSC curves by correlating the DSC results with the thermodynamic calculations. However, the literature review has shown that this is not the case in cooling, making it difficult to define the point of peritectic transformation. By combining the DSC with high-temperature Confocal Scanning Laser Microscopy results under comparable experimental conditions, it was possible to interpret the solidification behaviour of peritectic steels based on the DSC cooling curves. It was found that what was previously

reported in the literature to be a peritectic reaction on the DSC cooling curve, is, in fact, a solid-state transformation of undercooled solute poor δ dendrite core to γ. It was also established that 38% more heat is released during solidification of peritectic steels, compared to non-peritectic steels. Another important finding is that the undercooling of the δ to γ transformation in peritectic steels is measured to be greater (75°C) compared to non-peritectic steels (32-35°C).

3) Based on the literature survey on this topic, the solidification shrinkage values have not been thoroughly studied in past research studies. In the present study, the evaluation of the shrinkage formation during the peritectic transformation was made based on cooling conditions, comparable with the CC process. Little difference in shrinkage was found between peritectic and non-peritectic steels. However, cooling rate was shown to be a dominant factor, showing an increase in contraction during initial solidification stages at higher cooling rates.

4) The application of IR thermography is growing in Material Science because it provides contactless measurements of the surface temperature at high frame rates. However, the literature review did not show information where IR thermography is used to assess the solidification kinetics of steels. Therefore, in the current research, the thermal profile of the solidifying sample surface was carried out using a thermal imaging camera, which allowed observation of the localised remelting of the peritectic steel while it was solidifying in the mould. However, the remelting was not seen during solidification of non-peritectic steels.

5) High-temperature Confocal Scanning Laser Microscopy results showed that the peritectic solidification is accompanied by the localised remelting of primary solid δ phase during solidification. However, the exact reason for the remelting of peritectic steels was unclear. Therefore, applying the IR thermography during the CSLM tests highlights the reason for the defect formation during the initial solidification stages of peritectic steels because it showed the fluctuation of the temperature during solidification of Hypo-P steel and supported the proposed sequences of events described in at the end of section 6.5.

The overall aim of this thesis is to understand the formation of defects in peritectic steels and explain why the solidification behaviour of peritectic steels is different from non-peritectic. Therefore, the impact of the findings described above can be summarised in the following statements:

- The equilibrium solidification behaviour of steels can be predicted relatively quickly with thermodynamic calculations, such as Thermo-Calc. This is an important step before steel production because the casting parameters, like cooling rate and casing speed, for peritectic steels are different compared to non-peritectic. Therefore, adjusting the casting parameters before production of peritectic steels can help to minimise the defect formation in these steels.
- The excessive exothermic heat and delayed δ to γ transformation found during solidification of peritectic steels can have a negative impact on steel production because it increases the metallurgical length. The casting speed must be subsequently reduced to ensure that sufficient thickness of the solidified shell is formed upon cooling for it to be able to withstand a ferrostatic pressure. This agrees well with what is currently used in steel production, where slower casting speeds of peritectic steel grades lead to better performance and quality of the final product, however, the production time increases in this case.
- Thermo-Calc predicts that the solidification shrinkage of peritectic steels is larger compared to non-peritectic steels. The shrinkage measurements in this research have shown that by increasing the cooling rate, the amount of shrinkage increases during the initial solidification stages. However, the predicted equilibrium values cannot explain the reason for the defect formation during solidification, therefore it is important to conduct experiments to identify the root of the defect formation during solidification of peritectic steels.
- The observation of localised remelting of δ ferrite during solidification of peritectic steels that is accompanied with non-uniform shrinkage, temperature fluctuation and poor heat extraction also increases the metallurgical length during the casting of peritectic steels. This is additional important evidence, which explains why casting of peritectic steels must be done at slower casting speeds compared to the casting of non-peritectic steels. Otherwise, insufficient cooling of the peritectic steel would lead to the formation of a thin steel shell with localised hot spots in the areas where remelting

occurs. This would lead to stress formation at the solidifying shell and may result in cracking if the shell is unable to withstand the ferrostatic pressure. In the worst scenario, if the crack size increases, it may lead to hot tearing and even a breakout. Therefore, it is extremely important to ensure efficient heat extraction during the production of peritectic steels.

7.2 Further work

The following further investigations can be made, which will benefit the current research:

- Based on the observations made during the current research, we can improve the models of the solidification behaviour of peritectic steels. Currently, available models on the solidification behaviour of peritectic steels are mainly based on thermodynamic data and do not include localised remelting phenomena. Thus, it is important to take this research further and implement findings of remelting of peritectic steels during solidification into the models.

- Using a combination of CSLM and infrared thermography, assess the effect of superheat of the steel samples on the solidification behaviour of peritectic steels. Non-uniform shrinkage, temperature fluctuation and poor heat extraction during solidification of peritectic steels was shown to be one of the reasons for the defect formation. Therefore, it is important to understand how the solidification behaviour of peritectic steels may change by decreasing the overheating temperature of the peritectic steels before casting.

- Assess the variation of the chemical composition of the peritectic steels on the solidification behaviour. By adding austenite or ferrite stabilisers (the elements which can shift the solidification and phase transformation paths of the steels and alloys), the solidification path of the peritectic steels will change. It can either become narrower or completely disappear. So it is important to explore which element can be a dominant contributor to reduce or eliminate the defect formation of peritectic steels during solidification.

References

[1] S. Griesser, C. Bernhard, R. Dippenaar, Effect of nucleation undercooling on the kinetics and mechanism of the peritectic phase transition in steel, Acta Mater. 81 (2014) 111–120. doi:10.1016/j.actamat.2014.08.020.

[2] World Steel Association AISBL, World Steel in Figures 2017 now available, Brussels, Belgium. (n.d.).

[3] A. Badri, T.T. Natarajan, C.C. Snyder, K.D. Powers, F.J. Mannion, a. W. Cramb, A mold simulator for the continuous casting of steel: Part I. The development of a simulator, Metall. Mater. Trans. B. 36 (2005) 355–371. doi:10.1007/s11663-005-0065-5.

[4] P.E. Ramirez-lopez, K.C. Mills, P.D. Lee, B. Santillana, A Unified Mechanism for Oscillation Mark Formation, (2011).

[5] E.T. Turkdogan, Fundametals of steelmaking, The institute of materials, 1996.

[6] G.J. Davies, Solidification and casting, Applied science publisher LTD, London, 1973.

[7] D.M. Stefanescu, Science and engineering of casting solidification, second edition, 2009. doi:10.1007/978-0-387-74612-8.

[8] B. Terence, Steel Grades and Properties, (2017).

[9] K.E. Blazek, O. Lanzi lll, P.L. Gano, D.L. Kellogg, Calculation of the peritectic range for steel alloys, Iron Steel Technol. (2008).

[10] S. Moon, The peritectic phase transition and continuous casting practice, 2015.

[11] K. Hechu, C. Slater, B. Santillana, P. Srirangam, S. Sridhar, Real-time measurement of contraction behaviour of peritectic steels during solidification, in: AISTech - Iron Steel Technol. Conf. Proc., 2016: p. 11.

[12] M. Suzuki, Y. Yamaoka, Influence of carbon content on solidifying shell growth of carbon steels at the initial stage of solidification, Mater. Trans. 44 (2003) 836–844.

[13] T. Emi, H. Fredriksson, High-speed continuous casting of peritectic carbon steels, Mater. Sci. Eng. A. 413–414 (2005) 2–9. doi:10.1016/j.msea.2005.08.169.

[14] L.C. Hibbeler, B.G. Thomas, B. Santillana, a. Hamoen, a. Kamperman, Longitudinal

face crack prediction with thermo-mechanical models of thin slabs in funnel moulds, Metall. Ital. 101 (2009) 1–10.

[15] B.G. Thomas, H. Zhu, Thermal distortion of solidifying shell near meniscus in continuous casting of steel, in: JIM / TMS Solidif. Sci. Process. Conf., Honolulu, HI, 1995: pp. 197–208.

[16] S. Carless, A. Westendorp, A. Kamperman, J. Brockhoff, Optimization of surface quality through mold thermal monitoring, in: AISTech 2010 Proc., 2010: pp. 105–113.

[17] H. Yasuda, T. Nagira, M. Yoshiya, A. Sugiyama, N. Nakatsuka, M. Kiire, M. Uesugi, K. Uesugi, K. Umetani, K. Kajiwara, Massive transformation from delta phase to gamma phase in Fe–C alloys and strain induced in solidifying shell, IOP Conf. Ser. Mater. Sci. Eng. 33 (2012) 12036. doi:10.1088/1757-899X/33/1/012036.

[18] K.E. Blazek, O. Lanzi, H. Yin, Reason for the beneficial effect of sulfur additions on the hypoperitectic reaction in a 0.1 Pct carbon and the sulfur content needed to establish the effect, Metall. Mater. Trans. B Process Metall. Mater. Process. Sci. 43 (2012) 686–693. doi:10.1007/s11663-011-9620-4.

[19] P. Presoly, R. Pierer, C. Bernhard, Identification of defect prone peritectic steel grades by analyzing high-temperature phase transformations, Metall. Mater. Trans. A. 44A (2013) 5377–5388. doi:10.1007/s11661-013-1671-5.

[20] M.B. Santillana, Thermo-mechanical properties and cracking during solidification of thin slab cast steel, Delft University of Technology, 2013.

[21] D. Phelan, M. Reid, R. Dippenaar, Kinetics of the peritectic reaction in an Fe-C alloy, Mater. Sci. Eng. A. 477 (2008) 226–232. doi:10.1016/j.msea.2007.05.090.

[22] H. Shibata, Y. Arai, M. Suzuki, T. Emi, Kinetics of peritectic reaction and transformation in Fe-C alloys, Metall. Mater. Trans. B. 31B (2000) 981–991.

[23] M. Hillert, Phase equilibria, phase diagrams and phase transformations : their thermodynamic basis, Cambridge University Press, Cambridge, 1998.

[24] H. Stone, Materials science. Metals and Alloys, 2014.

[25] B.G. Thomas, Modeling of continuous casting defects related to mold fluid flow, Iron Steel Technol. 3 (2006) 128–143.

[26] H. Fredriksson, U. Akerlind, Materials Processing during Casting, John Wiley & Sons,

Ltd, 2012.

[27] M. Cohen, M.C. Flemings, Rapidly solidified crystalline alloys, Adam eds., Warrendale, PA, 1985.

[28] Stefanescu D.M., Science and engineering of casting solidification, Second Edi, 2009.

[29] H.W. Kerr, W. Kurz, Solidification of peritectic alloys, Int. Mater. Rev. 41 (1996) 129–164.

[30] S. Griesser, C. Bernhard, R. Dippenaar, Mechanism of the peritectic phase transition in Fe – C and Fe – Ni alloys under conditions close to chemical and thermal equilibrium, ISIJ Int. 54 (2014) 466–473.

[31] D.G. Eskin, Suyitno, L. Katgerman, Mechanical properties in the semi-solid state and hot tearing of aluminium alloys, Prog. Mater. Sci. 49 (2004) 629–711. doi:10.1016/S0079-6425(03)00037-9.

[32] D.M. Stefanescu, G. Upadhya, D. Bandyopadhyay, Heat transfer-solidification kinetics modeling of solidification of castings, Metall. Mater. Trans. A. 21A (2014) 997–1005. doi:10.1007/BF02656584.

[33] M.F. Basdogan, V. Kondic, G.H.J. Bennett, Graphite morphologies in cast irons, Trans. Am. Foundrymen's Soc. (1982) 263–273.

[34] H. Tian, D.M. Stefanescu, Experimental evaluation of some solidification kinetics-related material parameters required in modeling of solidification of Fe-C-Si alloys, Model. Cast. Weld. Adv. Solidif. Process. 6 (1993) 639–646.

[35] A.A. Howe, Segregation and phase distribution during solidification of carbon, alloy and stainless steels, 1991.

[36] M.E. Glicksman, Principles of solidification: an introduction to modern casting and crystal growth concepts, 2011. doi:10.1007/978-1-4419-7344-3.

[37] D. Phelan, In-situ studies of phase transformations in iron alloys, University of Wollongong, 2002.

[38] H. Fredriksson, The mechanism of the peritectic reaction in iron-base alloys, Met. Sci. 10 (1976) 77–86.

[39] H.W. Kerr, J. Cisse, G.F. Bolling, On equilibrium and non-equilibrium peritectic

transformations, 22 (1974).

[40] D. Phelan, M. Reid, R. Dippenaar, Kinetics of the peritectic phase transformation: In-situ measurements and phase field modeling, Metall. Mater. Trans. A. 37 (2006) 985–994. doi:10.1007/s11661-006-0071-5.

[41] Stefanescu D.M., Microstructure evolution during the solidification of steel, ISIJ Int. 46 (2006) 786–794.

[42] P. Presoly, G. Xia, P. Reisinger, C. Bernhard, Continuous casting of hypo-peritectic steels: mould thermal monitoring and DSC-analysis, BHM Berg- Und Hüttenmännische Monatshefte. 159 (2014) 430–437. doi:10.1007/s00501-014-0306-5.

[43] J. Agren, Calculation of phase diagrams: Calphad, Curr. Opin. Solid State Mater. Sci. 1 (1996) 355–360.

[44] D. Zhang, Characterisation and modeling of segregation in continuously cast steel slab, University of Birmingham, 2015.

[45] H.L. Lukas, J. Weiss, E.-T. Henig, Strategies for the calculation of phase diagrams, Calphad. 6 (1982) 229–251.

[46] B. Sundman, B. Jansson, J.-O. Andersson, The Thermo-Calc databank system, Calphad. 9 (1985) 153–190.

[47] M. Park, Fundametals of modeling for metal processing, ASM International, 2009.

[48] G. Eriksson, K. Hack, ChemSage, A computer program for the calculation of complex chemical equilibria, Metall. Mater. Trans. B. 21 (1990) 1013–1023.

[49] J.O. Andersson, T. Helander, L. Hoglund, P.F. Shi, B. Sundman, Thermo-Calc and DICTRA, Computational tools for materials science., Calphad. 26 (2002) 273–312.

[50] W.J. Boettinger, U.R. Kattner, K.-W. Moon, J.H. Perepezko, DTA and heat-flux DSC measurements of alloy melting and freezing, U.S. Government printing office, Washington, 2006. doi:10.1007/s13398-014-0173-7.2.

[51] K. Chattopadhyay, R. Goswami, Melting and superheating of metals and alloys, Prog. Mater. Sci. 42 (1997) 287–300. doi:10.1016/S0079-6425(97)00030-3.

[52] W. Kurz, D.J. Fisher, Fundamentals of solidification, Third Edit, Trans Tech Publications, 1992.

[53] Netzsch, Simultaneous Thermal Analyzer – STA 449 F3 Jupiter®, (2018) 20. https://www.netzsch-thermal-analysis.com/en/products-solutions/simultaneous-thermogravimetry-differential-scanning-calorimetry/sta-449-f3-jupiter/ (accessed 5 June 2018).

[54] Netzsch, The simultaneous thermal analyzer NETZSCH STA 449 F3 Jupiter, (2018). https://www.netzsch-thermal-analysis.com/media/thermal-analysis/brochures/STA_449_F3_Jupiter_en_web.pdf (accessed 10 July 2018).

[55] Netzsch, Accessories for differential scanning calorimeters and thermobalances, (2018) 80. https://www.netzsch-thermal-analysis.com/media/thermal-analysis/Accessories_Catalogue/Accessories_DSC_TGA_STA_0518w.pdf (accessed 5 June 2018).

[56] Netzsch, Functional principle of a heat-flux DSC, (2018). https://www.netzsch-thermal-analysis.com/en/landing-pages/principle-of-a-heat-flux-dsc/ (accessed 5 June 2018).

[57] E. Wielgosz, T. Kargul, Differential scanning calorimetry study of peritectic steel grades, J. Therm. Anal. Calorim. 119 (2014) 1547–1553. doi:10.1007/s10973-014-4302-5.

[58] H. Chikama, H. Shibata, T. Emi, M. Suzuki, 'In-situ' real time observation of planar to cellular and cellular to dendritic transition of crystals growing in Fe-C alloy melts, Mater. Trans. JIM. 37 (1996) 620–626. doi:10.2320/matertrans1989.37.620.

[59] I. Sohn, R. Dippenaar, In-situ observation of crystallization and growth in high-temperature melts using the confocal laser microscope, Metall. Mater. Trans. B Process Metall. Mater. Process. Sci. (2016) 1–12. doi:10.1007/s11663-016-0675-0.

[60] S. Griesser, R. Dippenaar, Enhanced concentric solidification technique for high-temperature Laser-Scanning Confocal Microscopy, ISIJ Int. 54 (2014) 533–535.

[61] M. Reid, D. Phelan, R. Dippenaar, Concentric solidification for high temperature laser Scanning Confocal Microscopy, ISIJ Int. 44 (2004) 565–572.

[62] T. Takahashi, K. Ohsasa, J. Tanaka, Peritectic reaction and delta-gamma transformation mechanism in carbon steels, Tetsu-to-Hagane. 73 (1987) 99–106.

[63] S. Griesser, M. Reid, C. Bernhard, R. Dippenaar, Diffusional constrained crystal nucleation during peritectic phase transitions, Acta Mater. 67 (2014) 335–341. doi:10.1016/j.actamat.2013.12.018.

[64] S. Aminorroaya, R. Dippenaar, A novel approach to simulate segregation at the centreline of continuously cast steel using Laser-Scanning Confocal Microscopy., J. Microsc. 227 (2007) 87–91. doi:10.1111/j.1365-2818.2007.01792.x.

[65] W.P. Bosze, R. Trivedi, On the kinetic expression for the growth of precipitate plates, 5 (1974) 1973–1974.

[66] N.J. McDonald, S. Sridhar, Peritectic reaction and solidification in iron-nickel alloys, Metall. Mater. Trans. A. 34 (2003) 1931–1940. doi:10.1007/s11661-003-0158-1.

[67] F. Huang, X. Wang, J. Zhang, C. Ji, Y. Fang, Y. Yu, In-situ observation of solidification process of AISI 304 austenitic stainless steel, J. Iron Steel Res. Int. 15 (2008) 78–82. doi:10.1016/S1006-706X(08)60271-X.

[68] C. Orrling, Y. Fang, N. Phinichka, S. Sridhar, A.W. Cramb, Observing and measuring solidification phenomena at high temperatures, Jom. 51 (1999). http://www.tms.org/pubs/journals/jom/9907/orrling/orrling-9907.html.

[69] C. Slater, K. Hechu, S. Sridhar, Characterisation of solidification using combined confocal scanning laser microscopy with infrared thermography, Mater. Charact. 126 (2017) 144–148. doi:10.1016/j.matchar.2017.02.025.

[70] C. Slater, S. Spooner, C. Davis, S. Sridhar, Chemically induced solidification: A new way to produce thin solid-near-net shapes, Metall. Mater. Trans. B. 47B (2016) 3221–3224. doi:10.1007/s11663-016-0785-8.

[71] K. Hechu, C. Slater, B. Santillana, S. Clark, S. Sridhar, A novel approach for interpreting the solidification behaviour of peritectic steels by combining CSLM and DSC, Mater. Charact. 133 (2017) 25–32. doi:10.1016/j.matchar.2017.09.013.

[72] M. Hillert, Communications: Mature of massive transformation, Metall. Mater. Trans. A. 35 (2004) 351–352.

[73] M. Hillert, Solidification and Casting of Metals, in: Eutectic Peritectic Solidif., The Metals Society, London, 1979: pp. 81–93.

[74] M. El-Bealy, H. Fredriksson, Modeling of the peritectic reaction and macro-segregation in casting of low carbon steel, Metall. Mater. Trans. B. 27 (1996) 999–1014.

[75] B. Korojy, Volume change effects during solidification of alloys, Royal Institute of Technology, 2009.

[76] H. Mehrara, D.G. Eskin, R.H. Petrov, M. Lalpoor, L. Katgerman, Linear contraction behavior of low-carbon, low-alloy steels during and after solidification using real-time measurements, Metall. Mater. Trans. A Phys. Metall. Mater. Sci. 45 (2014) 1445–1456. doi:10.1007/s11661-013-2089-9.

[77] J. Xu, S. He, X. Jiang, T. Wu, Q. Wang, Analysis of crack susceptibility of regular carbon steel slabs using volume-based shrinkage index, ISIJ Int. 53 (2013) 1812–1817. doi:10.2355/isijinternational.53.1812.

[78] J. Sengupta, C. Ojeda, B.G. Thomas, Thermal-mechanical behaviour during initial solidification in continuous casting: steel grade effects, Int. J. Cast Met. Res. 22 (2009) 8–14. doi:10.1179/136404609X368037.

[79] M. Suzuki, C. Yu, H. Sato, Y. Tsui, H. Shibata, T. Emi, Origins of heat transfer anomaly and solidifying shell deformation of peritectic steels in continous casting, ISIJ Int. 36 (1996) 171–174.

[80] A. Chrysochoos, Infrared thermography applied to the analysis of material behavior : a brief overview, 2013.

[81] R. Władysiak, A. Kozuń, An application for infrared camera in analyzing of the solidification process of Al-Si alloy, Arch. Foundry Eng. 15 (2015) 81–84. doi:10.1515/afe-2015-0065.

[82] J. Słoma, I. Szczygieł, A. Sachajdak, Verification of heat phenomena during surfacing using a thermal imaging camera, Weld. Int. 28 (2014) 610–616. doi:10.1080/09507116.2012.753220.

[83] S. Karnati, N. Matta, T. Sparks, F. Liou, Vision-based process monitoring for laser metal deposition processes, in: 24th Int. Solid Free. Fabr. Symp. - An Addit. Manuf. Conf., 2013: pp. 88–94.

[84] Z.J. Miao, A.D. Shan, W. Wang, J. Lu, W.L. Xu, H.W. Song, Solidification process of conventional superalloy by confocal scanning laser microscope, Trans. Nonferrous Met. Soc. China (English Ed. 21 (2011) 236–242. doi:10.1016/S1003-6326(11)60704-8.

[85] H. Yin, T. Emi, H. Shibata, Morphological instability of δ-ferrite/ γ-austenite interphase boundary in low carbon steels, Acta Mater. 47 (1999) 1523–1535. http://www.sciencedirect.com/science/article/pii/S1359645499000221.

[86] Y. Komizo, H. Terasaki, In-situ Studies of Phase Transformation in Steel During Welding, In-Situ Stud. with Photons, Neutrons Electrons Scatt. (2010) 209. doi:10.1007/978-3-642-14794-4_1.

[87] P. Presoly, R. Pierer, C. Bernhard, Linking up of HT-LSCM and DSC measurements to characterize phase diagrams of steels, IOP Conf. Ser. Mater. Sci. Eng. 33 (2012) 12064. doi:10.1088/1757-899X/33/1/012064.

[88] H. Yin, T. Emi, H. Shibata, Determination of free energy of δ-ferrite/γ-austenite interphase boundary of low carbon steels by in-situ observation, ISIJ Int. 38 (1998) 794–801. doi:10.2355/isijinternational.38.794.

[89] R. Dippenaar, C. Bernhard, S. Schider, G. Wieser, Austenite grain growth and the surface quality of continuously cast steel, Metall. Mater. Trans. B. 45 (2014) 409–418. doi:10.1007/s11663-013-9844-6.

[90] T. Wang, S. Cai, J. Li, J. Xu, Z. Chen, J. Zhu, Z. Cao, T. Li, Mould taper optimization for continuous casting steels by numerical simulation, China Foundry. 7 (2010) 61–67.

[91] TopCast SRL, Topcast TMF - Manual Extraction Furnaces, (2018). https://www.topcast.it/en/products/induction-melting-furnaces/tmf-manual-extraction-furnaces/tmf-manual-extraction-furnaces_24.html (accessed 5 June 2018).

[92] D.G. Eskin, L. Katgerman, Suyitno, J.F. Mooney, Contraction of aluminum alloys during and after solidification, Metall. Mater. Trans. A. 35 (2004) 1325–1335. doi:10.1007/s11661-004-0307-1.

[93] A.H.W. Lee, D.E. Klein, J.P. Lamb, Constant flux, turbulent convection data using infrared imaging, Int. J. Heat Mass Transf. 37 (1994) 535–539.

[94] Micro-Epsilon UK Ltd., Thermo-Imager TIM - Compact thermal imaging cameras, (2018). https://www.micro-epsilon.com/temperature-sensors/thermoIMAGER/?sLang=en (accessed 5 June 2018).

[95] M.D. Abramoff, P.J. Magalhaes, S.J. Ram, Image processing with ImageJ, Biophotonics Int. 11 (2004) 36–42.

[96] W. Rasband, The ImageJ user guide, (2010). https://imagej.nih.gov/ij/docs/guide/user-guide.pdf.

[97] Fluke Corporation, Emissivity values of common materials, (n.d.).

https://www.emlab.com/m/store/Fluke Thermal Camera Emissivity Values.pdf (accessed 10 February 2016).

[98] Micron Instrument Company, Table of emissivity of various surfaces, (n.d.). http://www-eng.lbl.gov/~dw/projects/DW4229_LHC_detector_analysis/calculations/emissivity2.pdf (accessed 10 February 2016).

[99] S. Nagarajan, S. Nagarajan, P. Banerjee, P. Banerjee, W. Chen, W. Chen, B. a Chin, B. a Chin, Control of the welding process using infrared sensors, Society. 8 (1992) 86–93. doi:10.1109/70.127242.

[100] W. Baldwin, Metallography and microstructures handbook, ASM Int. 9 (2004) 2733. doi:10.1361/asmhba0003771.